NORTHWESTERN UNIVERSITY

Initial Stages of Thin Film Deposition: Metal-Induced Surface Reconstructions on Semiconductors and the Nucleation of Cubic Boron Nitride

A DISSERTATION

SUBMITTED TO THE GRADUATE SCHOOL
IN PARTIAL FULFILLMENT OF THE REQUIREMENTS

for the degree

DOCTOR OF PHILOSOPHY

Field of Materials Science and Engineering

By
Christopher Collazo-Davila

EVANSTON, ILLINOIS

June 1998

ABSTRACT

Initial Stages of Thin Film Deposition: Metal-Induced Surface Reconstructions on Semiconductors and the Nucleation of Cubic Boron Nitride

Christopher Collazo-Davila

The deposition of thin films is becoming an increasingly more important part of many new technologies. The degree of control made available through modern thin-film deposition techniques allows an engineer to conceive of and create structures on an atomic scale. This has given rise to new challenges in atomic scale characterization. In this thesis, new and powerful approaches to atomic scale characterization are employed to solve several current thin-film deposition problems. Experimental measurements are obtained on an integrated, in-situ surface analysis system with an adjoining ultra-high vacuum transmission electron microscope.

Transmission electron diffraction data is used to refine the atomic positions of the Ge(001)-(2x1) native surface reconstruction. It is then shown that direct methods techniques can be applied to both transmission electron diffraction and X-ray diffraction data to solve completely unknown surface structures. Direct methods are

applied to X-ray diffraction data from the Ge(111)-(4x4)/Ag surface to determine its structure. Also, two related linear surface structures on Si, the Si(111)-(3x1)/Ag and the Si(111)-(4x1)/In structures, are both solved by applying direct methods to transmission electron diffraction data. A general trend for linear reconstructions on the Si (111) surface is noted by comparing the newly solved Si(111)-(3x1)/Ag and Si(111)-(4x1)/In structures to the previously solved Si(111)-(5x2)/Au structure.

Finally, in-situ high energy electron bombardment and high-resolution electron microscopy are used to reveal the formation of nanoarches in hexagonal boron nitride. The nanoarch structures are shown to be possible nucleation sites for the cubic phase of boron nitride, and the growth of cubic boron nitride thin films is explained based on this new nucleation mechanism.

Approved by

Professor Laurence D. Marks (Thesis advisor)

Department of Materials Science and Engineering

Robert R. McCormick School of Engineering and Applied Science

Northwestern University, Evanston, IL 60208

To my wife, my parents, my two sisters, and Grandma Urweider. I owe all of my accomplishments to the unwavering support of my family.

ACKNOWLEDGEMENTS

First I'd like to thank my classmates, Eric Landree and Daniel Grozea, for helping me to survive. They were always there with their support and friendship. I don't know how any of us would have fared if we didn't have each other.

Thank you Erman Bengu for your friendship, thoughtful discussions, and entertaining debates with Dan. I also owe thanks to Ganesh Jayram for "taking me under his wing" and for always being willing to take time to explain things to me, and to Hong Zhang for her support, guidance, and encouragement.

Thanks are due to Bob Passeri for of his help during the early years, and to Jim Poulos for going beyond the call of duty as a service representative for Hitachi. I'd like to thank Mark Kirk for his guidance and participation in the ion-irradiation studies of hexagonal boron nitride, Robert Feidenhans'l and coworkers for supplying the X-ray diffraction data used in the study of the Ge(111)-(4x4)/Ag surface, and K. Nishii and Y. Tanishiro for supplying the transmission electron diffraction data for the study of the Si(111)-(4x1)/In surface. I'd also like to thank Dr. Robert P. Flemming for many fruitful discussions.

This work was funded by the National Science Foundation under grant #DMR-9214505.

TABLE OF CONTENTS

TABLES

FIGURES

CHAPTER 1: INTRODUCTION

1.1 Atomic Scale Engineering and Characterization

The rise of the semiconductor industry has pushed man's ability to engineer materials on an atomic scale. The current minimum lateral feature size found on a semiconductor chip is around 250 nm, and the familiar semiconductor industry's "roadmap" calls for a steady reduction in that size to 50 nm within the next fifteen years. At that point, the dimensions of the electronic devices on a chip will be on the order of several hundred atoms across. However, the thrust towards the atomic scale is not limited to the world of semiconductors alone. Other major industries are pushing the scale of engineering to ever decreasing sizes as well. Some hard coatings research is exploring multilayer films where the thickness of a single layer is only a few nm (Shinn and Barnett 1994; Madan, Chu, and Barnett 1996). Also, as chapter 5 of this thesis shows, it appears that a detailed atomic-scale understanding of the growth process of cubic boron nitride (a potential hard coating material) is necessary in order to develop new processes capable of making high quality films. Moreover, many researchers predict that the field of microelectromechanical devices (MEMS) is on the brink of a rapid expansion into industry (Marshal 1997).

In these growing high-technology nanoscale environments, the materials scientist's job remains the same -- to relate the structure of a material to its properties. While the properties may still manifest themselves on a macroscopic scale (e.g. surface hardness or I-V response curves) and may therefore still be measurable through conventional means, microscopic structures have become increasingly more difficult to determine. New characterization techniques have emerged, and old ones have become more sophisticated, but the technology of microstructural characterization seems to be falling behind envisioned designs. A recent article in *Research and Development Magazine* (Comello 1998) identifies metrology as one of the biggest barriers standing between the semiconductor industry and 100 nm feature sizes. In order to overcome this barrier the latest edition of the semiconductor industry's roadmap suggests a move towards in-situ, integrated analysis by placing a variety of characterization equipment directly on the chip fabrication line. This move towards in-situ analysis and the integration of different analysis techniques can be seen in many areas of research, and it is proving to be a powerful approach that is necessary to overcome the most difficult characterization challenges.

This thesis underscores the capabilities of the integrated, in-situ analysis approach to microstructural characterization. Through the use of an integrated analysis system described in section 1.2.1, the surfaces of germanium and silicon and the structure of several thin metal films on these two semiconductors have been characterized on an atomic scale (Chapters 2 - 4). Also, the atomic scale dynamics

taking place during the nucleation of cubic boron nitride thin films have been determined as described in Chapter 5.

1.2 Experimental Approach

Much of the research described within this dissertation involved the use of the SPEAR system described in section 1.2.1. The system was designed by Prof. L.D. Marks and Prof. P.C. Stair with the help of Superior Vacuum Technology (SVT), which is now part of EPI. SVT built the system and delivered it to Northwestern University. Through the efforts of Ganesh Jayaram, Richard Plass, Eric Landree, Daniel Grozea, and myself the SPEAR system was made operational (Collazo-Davila et al. 1995). Eric Landree, Daniel Grozea, Erman Bengu, and I have been responsible for the system's maintenance. Erman Bengu was responsible for designing the boron nitride growth chamber attached to the SPEAR system.

1.2.1 The SPEAR System

SPEAR stands for Sample Preparation Evaluation Analysis and Reaction. The fundamental reason for the creation of the system was to have the capabilities of a high-resolution transmission electron microscope (TEM) paired with standard film growth and surface characterization techniques all within the same ultra high vacuum (UHV) environment. A schematic diagram of the system is shown in figure 1.1a, and a photograph appears in figure 1.1b. A central sample transfer chamber serves as the link

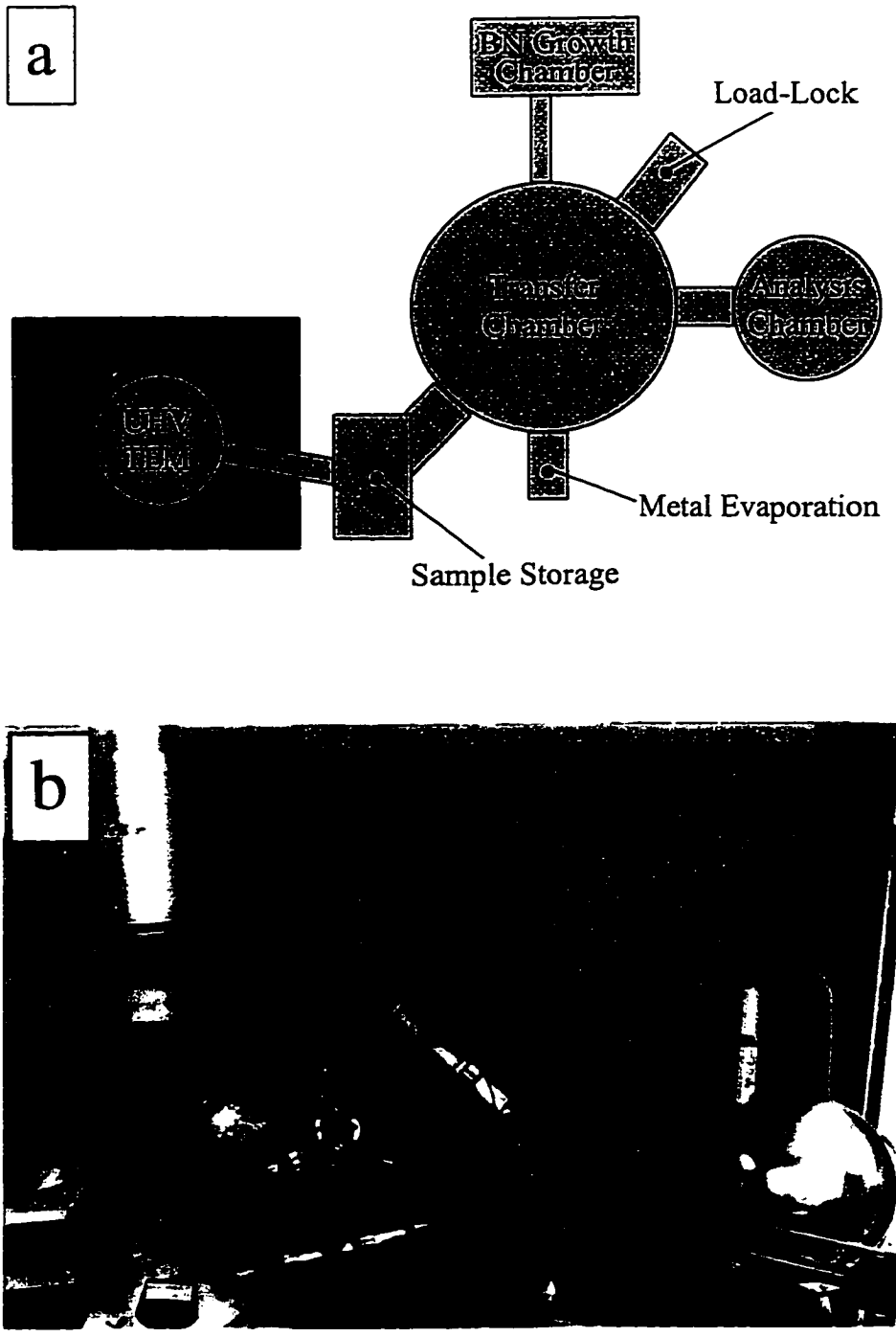

Figure 1.1. a) Schematic diagram of the SPEAR surface analysis system viewed from the top. b) Photograph of the SPEAR system.

between a UHV H-9000 Hitachi TEM, a surface preparation/analysis chamber, a load-lock, and a boron nitride film growth chamber. The surface analysis chamber has a Perkin Elmer 04-548 dual anode x-ray tube and a Phi 10-360 spherical capacitance electron energy analyzer (SCA) allowing the collection of x-ray photoelectron spectroscopy (XPS) data. An FEI single lens field-emission scanning electron gun can produce Auger electron spectroscopy (AES) data as well as scanning electron microscopy (SEM) images. The surfaces of samples can be sputtered and imaged at the same time with a 6050 Phi duoplasmatron variable gas source ion gun package, and samples can be annealed either by direct current heating or by electron bombardment using a high-current electron gun.

Samples placed into the load lock (up to 5 at a time) can be brought into the main transfer chamber after an eight hour bake-out step which lowers the pressure in the load lock to about $5x10^{-10}$ torr. The base pressure in the transfer, growth, and analysis chambers is in the low 10^{-11} torr range, and the pressure in the objective region of the H-9000 TEM where the sample sits is less than $1x10^{-10}$ torr with the electron beam on. The growth chamber has a Thermionics 100-0010 3 kW electron beam evaporation source for the evaporation of pure boron, and an Astex compact electron cyclotron resonance (ECR) nitrogen source. A Perkin Elmer 04-300 ion gun can independently provide 500 eV - 4 keV Ar^+ ion bombardment of the growing film. A small 4 inch port on the side of the transfer chamber has been modified by Dr. Richard Plass to provide

metal evaporation from resistively heated tungsten boats. The metal evaporation capability was used to deposit silver in the study of the Si(111)-(3x1)/Ag structure discussed in section 4.2.

1.2.2 Substrate Preparation

The substrates used for deposition or native surface studies were either silicon or germanium, and the basic sample preparation procedure that was common to both materials is outlined here. The sample geometry is dictated by the TEM sample cartridge. All specimens have to be in the form of a 3 mm diameter disc and must have regions that are only a few hundred angstroms thick in order to be suitable for TEM study. Starting from a commercial Si or Ge wafer (400 μm to 600 μm thick), 3 mm discs were cut using the ultrasonic disc cutter in Prof. V.P. Dravid's lab. The discs were then thinned to 200 μm using 600 grit alumina sandpaper. Next, the samples were dimpled to a thickness of 20 μm to 30 μm in the center with a VG1000 dimpler using a force of 10 g. and a grinding wheel speed of 20 rpm to 40 rpm. At a central thickness of 30 μm, the thickness at the edge of the 3 mm disc is about 180 μm. As a final step in the dimpling process, the samples were polished using first 1 μm diamond paste, and then a 0.1 μm syton colloidal suspension. The thinning of the sample was completed by a chemical etch consisting of a nitric and hydrofluoric acid solution in a 9 to 1 ratio for Si and Ge(001). The etch was stopped as soon as a hole was seen to form at the center of the 3 mm disc.

Before being placed in the SPEAR system, the samples were mounted in a molybdenum ring (fig. 1.2). The molybdenum ring has a lip on which the sample disc rests, and either a tantalum or a tungsten spring clip above the sample keeps it firmly in place. The molybdenum ring allows fragile TEM samples to be transferred safely and also provides a route for heating by directly passing current through the molybdenum. Once inside the UHV system, chemical impurities were removed from both the top and the bottom surfaces of a sample by cycles of ion milling and annealing. Monitoring of the surface impurity level was accomplished through XPS. Figure 1.3 shows a sequence of XPS spectra collected during the cleaning of a Si(001) sample. When the surface impurity levels were below the XPS detection limit, the sample was moved into the microscope to check for the native surface reconstruction of the substrate using TED (see for example fig. 2.3).

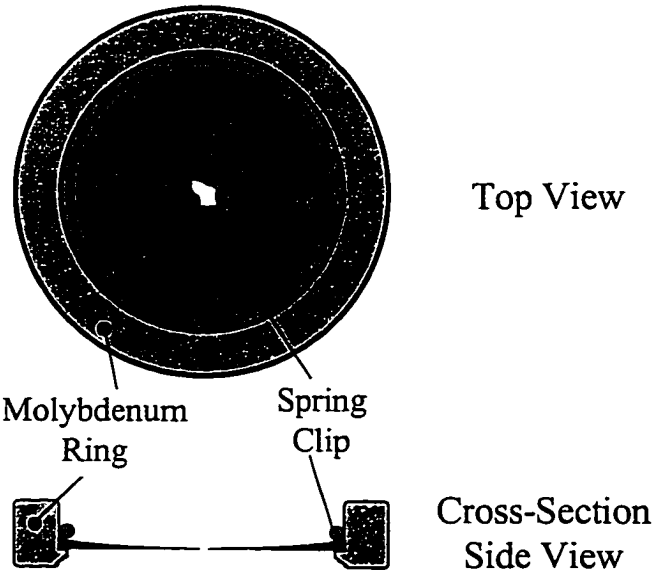

Figure 1.2. Drawing of the molybdenum ring for holding samples in the SPEAR system. The spring clip can be either tungsten or tantalum.

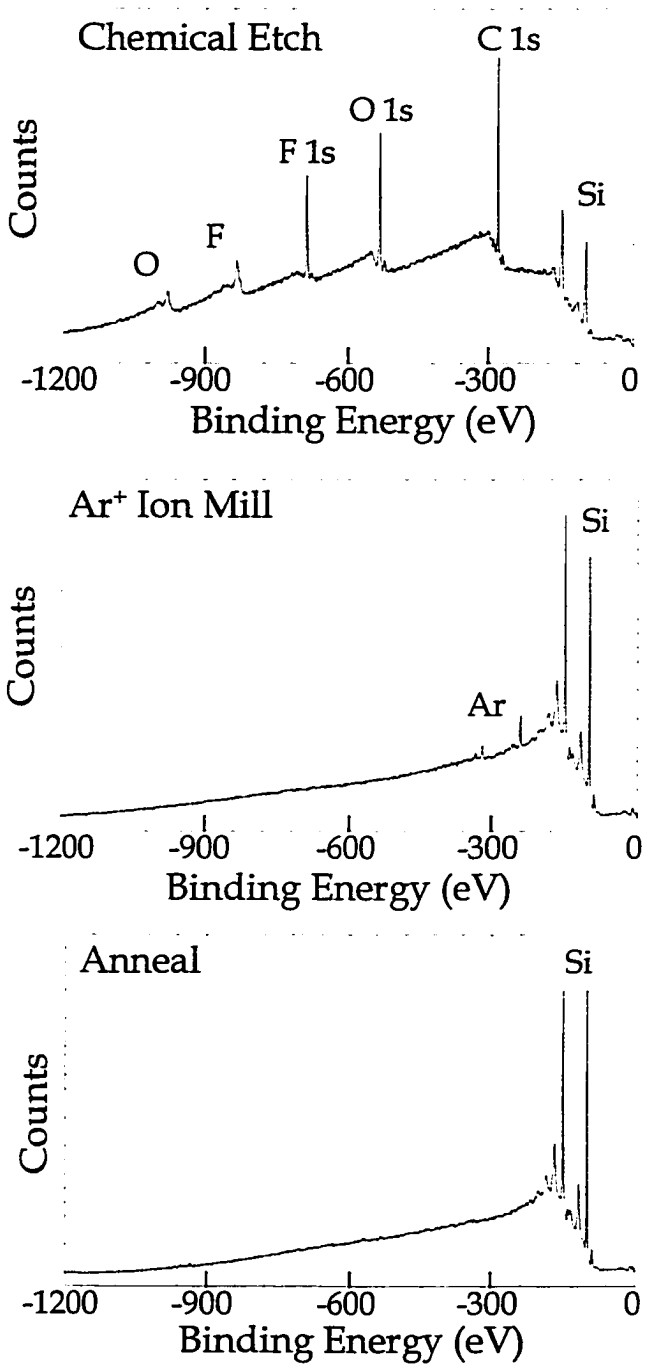

Figure 1.3. Sequence of XPS spectra collected during a milling/anealing cycle while removing impurities from a Si(001) substrate.

1.2.3 Surface Reconstructions

The atoms at the surface of a crystal reside in a different environment than the atoms inside the bulk of the material. Consequently it often happens that the lowest energy arrangement for the surface atoms differs from the arrangement of atoms inside the bulk. This new arrangement of surface atoms is called a surface reconstruction. Figure 1.4a shows the (001) surface for a diamond-cubic crystal with all of the atoms left in their normal bulk positions. In this arrangement there are two dangling bonds on each

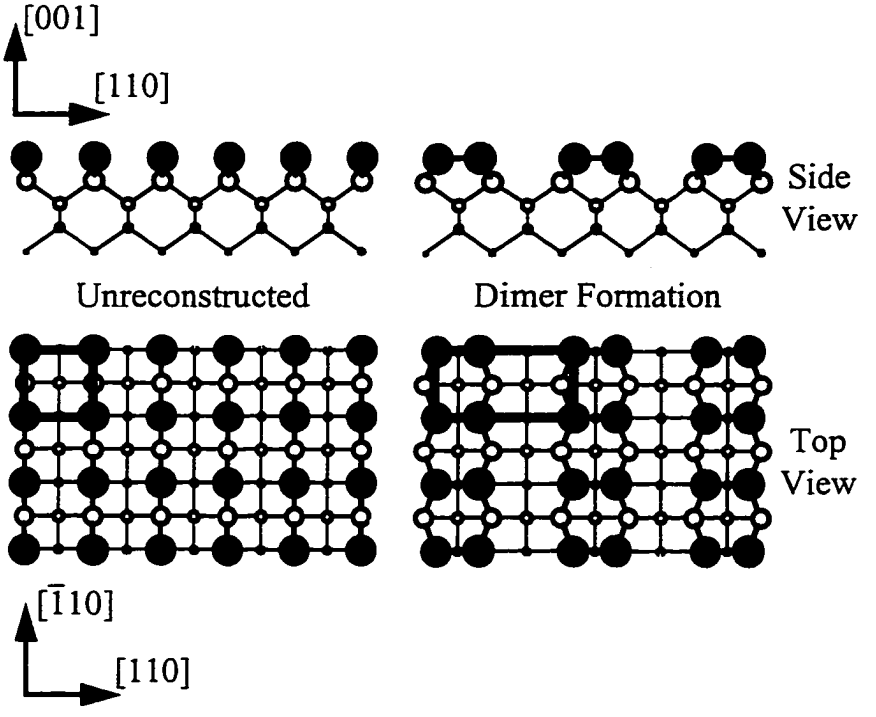

Figure 1.4. a) The (001) surface of a diamond cubic crystal with all atoms remaining in their bulk positions. The square 1x1 2D unit cell for the atoms on the surface is outlined in black. b) The same surface after reconstruction and the formation of dimers. The new 2x1 2D unit cell for the surface atoms is outlined in black and is twice the size of the 1x1 unit cell aong the [110] direction.

surface atom, and the system can lower its potential energy by forming new bonds between atoms on the surface. As shown in Figure 1.4b, each surface atom bonds to a neighboring atom along a <110> direction. The new pairs of atoms bonded to each other at the surface are referred to as dimers, and the surface reconstruction is called a (2x1) reconstruction in reference to the size and orientation of the 2D unit cell for the new surface structure.

Surface reconstruction nomenclature is based on the 2D unit cell for the atoms on the surface while in their bulk positions before reconstruction takes place (Wood 1963). In the case of the (001) surface of a diamond-cubic crystal, the surface atoms in their bulk positions form a 2D lattice with a square unit cell which is outlined in figure 1.4a. This base unit cell of the bulk-terminated surface is always referred to as a 1x1 unit cell. After rearrangement of the surface atoms, a new 2D unit cell is drawn for the surface structure (fig. 1.4b), and the surface reconstruction is called a 2x1 reconstruction because the a-axis of the reconstructed unit cell is "2" times as long as the a-axis of the original 1x1 unit cell, and the b-axis is "1" times as long as the b-axis of the 1x1 unit cell. In general, a reconstruction will be labeled as (nxm)Rϕ°, where the reconstructed unit cell has an a-axis length "n" times the a-axis length of the 1x1 cell and a b-axis length "m" times the b-axis length of the 1x1 cell, and the reconstructed unit cell is rotated by an angle of "ϕ"° relative to the 1x1 unit cell. If there is no rotation of the surface unit cell then the Rϕ° is left off instead of explicitly writing R0°.

Reconstructions were monitored as part of the work presented in this thesis both for their intrinsic interest (specific reconstructions are the subjects of study in the research described in Chapters 2 - 4) and also for their ability to provide information about impurities not detectable by XPS (native substrate reconstructions were always verified to be present before the deposition of any thin films). In terms of atomic scale engineering, the smaller engineered structures become, the more important are their surfaces and interfaces in terms of determining their behavior. Unfortunately, our understanding of surface and interface physics is far from complete, and it currently does not provide accurate predictive abilities. Being able to characterize and understand atomic structures at a surface or an interface is an important step in the process of building a working knowledge of surface and interface physics which will one day allow accurate predictions to be made. In terms of impurity monitoring, most native surface reconstructions are highly sensitive to small amounts of adsorbed atoms including hydrogen which is not detectable by XPS. If a native surface reconstruction is detected by TED, then one can be sure that the surface is almost completely free of any foreign adsorbate atoms. The presence of a strong surface structure diffraction pattern also indicates long range order which shows that the surface is relatively flat on an atomic scale with surface steps spaced by at least several tens of nanometers apart.

CHAPTER 2: TRANSMISSION ELECTRON DIFFRACTION FOR STUDYING SURFACES

2.1 Surface-Sensitive Experimental Techniques

Despite the development of many experimental techniques for studying surfaces of crystalline materials, determination of the atomic geometry of a surface reconstruction remains a difficult experimental task. No single method exists which can independently and routinely solve surface structures. The ideal technique would a priori produce an image which would be directly interpretable in terms of surface atomic positions. Unfortunately the only two imaging techniques which have the lateral resolution required to discern individual atoms, scanning tunneling microscopy (STM) and high resolution transmission electron microscopy (HRTEM), each have their own limitations. STM can produce low-noise images of the density of states at a surface with a resolution near 0.2 nm. However, peaks in the density of states do not always correspond to surface atom positions, and even if they do, the atomic position information is limited to a single layer of atoms. HRTEM is able to image all layers of atoms in a reconstruction, but HRTEM images are difficult to obtain and suffer from relatively large amounts of noise and high background signals.

As an alternative approach to directly imaging surface atoms, one can perform any measurement which is sensitive to the surface atomic positions. Providing that the theory describing the measurement process is well enough understood to be accurately simulated, quantitative comparisons can be made between the measurements and values simulated from a tentative model for the surface structure. The success of this approach relies on the accuracy of the simulations and in any case can only confirm or refute an hypothetical model. The most common type of surface measurements which are compared to simulations are diffraction techniques. Low energy electron diffraction (LEED) has been applied to almost every known surface reconstruction. While giving valuable information about the dimensions of the unit cell and the nature of any disorder in the surface structure, the scattering of the low energy electrons is highly dynamical and is difficult to accurately model. Reflection high energy electron diffraction (RHEED) is another technique which, due to strong dynamical diffraction, is difficult to simulate. Grazing incidence x-ray diffraction (GIXRD), on the other hand, can be well described by the relatively simple kinematical theory of diffraction, and has been employed in many cases to refine surface reconstructions. Its only limitation is the experimental difficulties associated with obtaining GIXRD data.

Perhaps one of the most powerful techniques for determining surface structures is transmission electron diffraction (TED). If the TEM sample is tilted away from a major bulk zone axis, the surface diffraction intensities can be approximated using kinematical diffraction theory. Precise refinements are also possible since the required dynamical

diffraction calculations can be accurately performed using the established multislice simulation method. Although TED comes with its own experimental difficulties (mostly due to sample preparation), the technique has a major advantage over GIXRD with respect to data collection times. A complete GIXRD data set requires several hours to a few days to acquire -- even using modern sources of synchrotron radiation. A complete TED data set can be recorded on film in under 5 minutes. The main reason surface TED has not found more widespread use is that it requires highly specialized equipment which is expensive and not readily available. Most surface reconstructions must be formed under UHV conditions in order to survive long enough to be studied, and there are only a handful of UHV transmission electron microscopes in the world. Despite the rarity of capable laboratories, TED has made significant contributions to the field of surface science. Solution of the celebrated Si(111)-(7x7) structure was based on TED data (Takayanagi et al. 1985), and more recently our group has used TED data to solve and refine a number of structures.

2.2 TED Data Collection and Reduction

Before collecting surface diffraction data in a TEM, the sample is tilted a couple of degrees off the zone-axis in order to attenuate the bulk reflection intensities relative to the surface reflection intensities (Jayaram, Plass, and Marks 1995). A series of negatives is then exposed with increasing exposure times. Typical exposure times will range from 0.5 s to 120 s. Such an exposure series will cover the wide dynamic range found in a

typical diffraction pattern. Parallel Electron Energy Loss Spectroscopy (PEELS) data may be collected from the transmitted beam and the most intense bulk diffracted beams as well. By measuring the bulk spot intensities relative to the transmitted beam with PEELS, absolute comparisons can be made between simulated and measured diffraction intensities during the fitting process. PEELS measurements also provide an estimate of the sample thickness based on the ratio of the number of electrons in the entire spectrum to the number of zero-loss electrons (Malis, Cheng, and Egerton 1988).

After developing, the diffraction pattern negatives are digitized to 8 bits with a 25 μm pixel size using an Optronics P-1000 microdensitometer. Relative beam intensities are then measured using a cross-correlation technique developed in our group (Xu, Jayaram, and Marks 1994). For each digitized negative, around 10 strong but non-saturated spots are chosen, independently scaled to unit integrated intensity, and then averaged together to form a motif representing the general shape of a diffraction spot. Separate motifs can be formed for bulk and surface reflections since their shapes may differ due to domain size effects. After the formation of the motifs, a software routine scans through the negative comparing each non-saturated spot with the appropriate motif. At each point of comparison, the background of diffuse scattering surrounding a sharp diffraction spot is removed. For the comparison, the center of the spot to be measured is found by cross-correlation with the motif. With the centers of the spot and the motif precisely aligned, a least squares fit between the two is calculated pixel by pixel assuming that the measured spot is simply a scaled up version of the motif. In this

manner, the intensities of all the surface spots on a given negative are determined relative to each other. For PEELS data, a one dimensional analog of the cross-correlation method can be used to obtain the relative intensities of the transmitted beam and strong bulk spots, and in subsequent analysis the PEELS intensity data can be treated the same as if coming from another negative with its own exposure time.

Next, to compare intensities from different negatives in the exposure series, scaling factors between the pictures are defined. Denoting the scaling factor between pictures 1 and 2 as s_1, the scaling between 2 and 3 as s_2, and so on, there are a total of (P-1) factors if the total number of pictures is given by P. These factors are calculated by minimizing the quantity,

$$\sum_{i=1}^{P-1} \sum_{j=(i+1)}^{P} \sum_{n} \left(I_{i,n} - S_{i,j} I_{j,n} \right)^2 \qquad (2.1)$$

where $S_{i,j}=(s_i)(s_{i+1}) \ldots (s_{j-1})$ represents the scaling between pictures i and j, and $I_{i,n}$ is the intensity of beam number n in picture i. The sum over n is taken over all beams which were measured in both pictures i and j. Many beams are often measured on as many as six negatives in the middle of an exposure time series. Using the multiple measurements and the calculated scaling factors, average intensities scaled to the shortest exposure time are found. Due to the digitization process, there is a fixed window of optical density which can be measured on a negative regardless of exposure time. However, as the exposure time increases, the background noise on the film increases relative to the fixed measurement window. To account for this changing uncertainty in intensity

measurements, a separate variance is calculated for the data from each negative. The variances are used for error estimates of individual measurements when calculating a final average value and associated error (For details see appendix A).

2.3 TED Data Simulation and Surface Structure Refinement

2.3.1 Quantitative Measures of Agreement

There are many standard methods used to quantify the agreement between two sets of numbers. This discussion will be limited to the three numerical measures of agreement appearing in this thesis, and it will be presented in the context of comparing a set of measured diffraction intensities to a corresponding set of simulated values.

First, an R-factor defined as,

$$R \equiv \frac{\sum_{j=1}^{N} I_j^{meas} - I_j^{calc}}{\sum_{j=1}^{N} I_j^{meas}} \qquad (2.2)$$

can be calculated without the need for any estimates of the measurement errors. I^{meas} is a measured intensity, I^{calc} is the simulated diffraction intensity, and N is the total number of measured intensities. Refinements using this R-factor are insensitive to the weaker reflections in a data set since the weak reflections contribute relatively little to the sum in equation 2.2. Therefore, in an R-factor fit the largest measured intensities will match the simulated intensities within unrealistically small percentage errors at the expense of a reasonable match for the weakest reflections.

Alternatively, a reduced χ^2 value defined as,

$$\chi^2 \equiv \frac{1}{N-M}\sum_{j=1}^{N}\left(\frac{I_j^{meas} - I_j^{calc}}{\sigma_j}\right)^2 \qquad (2.3)$$

takes into account estimates of the measurement errors, the σ_j's, for each beam. M is the number of parameters being varied during the fitting process. The χ^2 value leads to a more reasonable distribution of the fitting errors, and it can be interpreted as a statistical measure of the probability of making a given set of observations (Bevington and Robinson 1992, 68). For a good fit, the numerator in the sum should be on average about equal to the denominator, and the value of χ^2 will tend towards 1. If it is much less than 1, then the estimates of the measurement errors are too large. If it is much greater than 1, then the estimates of the measurement errors may be too small, the postulated model may not be completely correct, or the simulation calculations may not accurately represent the experimental measurement process. In any case, the statistical interpretation of χ^2 rests on the assumption that the measurement errors follow a gaussian distribution. In practice this is not always the case, and there are often "outlier" measurements which are grossly inaccurate for one reason or another.

In a situation where the measurement errors do not follow gaussian distributions, a χ measure of agreement can be employed. The χ value is defined as,

$$\chi \equiv \frac{1}{N-M}\sum_{j=1}^{N}\frac{\left|I_j^{meas}-I_j^{calc}\right|}{\sigma_j} \qquad (2.4)$$

The χ factor is similar to χ^2 and for a reasonable fit will tend toward a value of 1, but it is less sensitive to points with large errors. While in the calculation of χ^2 a large value of (I^{meas} - I^{calc}) for a poorly fit beam will be squared and will contribute significantly to the sum, the same (I^{meas} - I^{calc}) in the calculation of χ will only be a few times larger than most of the other terms in the sum and will not be treated with undue importance.

2.3.2 TED Data Fitting Procedure

While kinematical diffraction theory provides a good description of weakly scattered x-rays, a dynamical approach is needed for more strongly scattered electrons. For this thesis, dynamical diffraction calculations were performed with the Northwestern University Multislice and Imaging System (NUMIS) package. In the standard multislice approach used by NUMIS, the crystal is cut into slices perpendicular to the direction of the incident electron plane wave. The scattering calculations are performed slice by slice as the wave propagates through the crystal.

Both the total sample thickness and the angle of tilt between the crystal zone axis and the incident beam direction must be known for an accurate TED simulation. An initial estimate of the crystal tilt can be found by looking at one of the longer exposure negatives of the diffraction pattern and using either the intersection of Kikuchi lines or the curvature of the zeroth order Laue zone to find the distance between the transmitted

beam and the center of the zone axis. Next, an R-factor is used to compare the measured bulk reflection intensities with simulated intensities in a three dimensional grid search with two search axes corresponding to the two possible tilt directions and the third axis corresponding to the sample thickness. While the crystal tilt can be found to within a few hundredths of a degree during this step, the thickness cannot always be uniquely determined. For a fixed crystal tilt near the correct value, the calculated R-factor for simulated bulk intensities will oscillate with thickness. Typically, in the range of 0 nm to 70 nm, two or three values of the thickness will be found to give reasonable measures of agreement. The ambiguity can be eliminated by analyzing the PEELS data taken from the sample. PEELS is accurate to around 10% when used to estimate thickness (Malis, Cheng, and Egerton 1988), and this is accurate enough to clearly agree with only one of the possible choices found during the grid search.

Once the crystal tilt and thickness have been determined, the surface structure can be refined. A multislice calculation yields simulated intensities for the surface diffraction spots and either a χ or a χ^2 value is used to quantify the agreement with the measured intensities. A standard minimization algorithm varies the atomic positions in the surface slices to search for a better fit. The procedure is iterated until a minimum χ or χ^2 value is found.

2.4 Refinement of the Ge(001)-(2x1) Native Surface Reconstruction

The data for this study (Collazo-Davila, Grozea et al. 1997) were collected using the SPEAR system described in section 1.2.1. The Ge(001) sample preparation and the diffraction data collection were accomplished through the combined efforts of myself, Mr. Daniel Grozea, and Mr. Eric Landree.

2.4.1 Background Information

The (2x1) reconstruction on Si(001) and Ge(001) has been the focus of many investigations since it was first observed (Schlier and Farnsworth 1959) using LEED. Today many details about the structure and dynamics of the two surfaces are known. It is generally accepted that the basic building block of the Si(001) and Ge(001) reconstructions is an asymmetric dimer (see figure 2.1). Atoms on the (001) surface

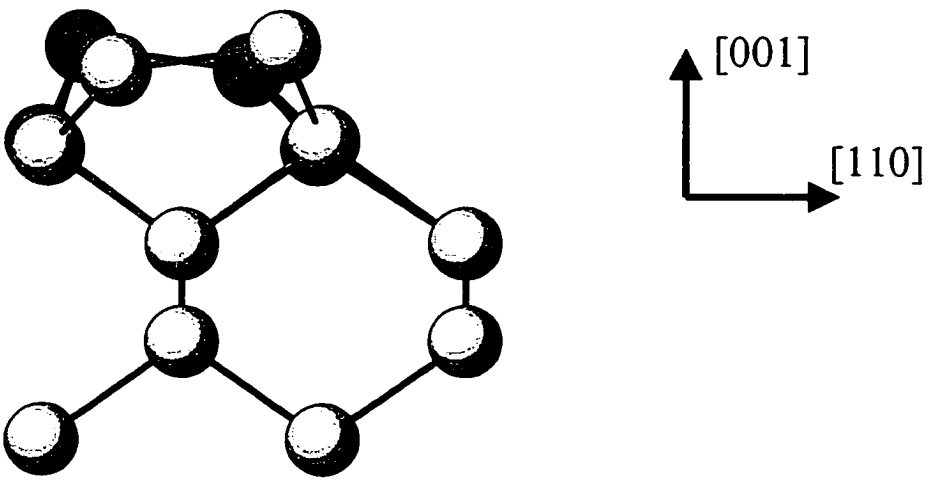

Figure 2.1. Buckled dimer which forms the basic building block for native Si(001) and Ge(001) reconstructions. Two possible tilt directions are indicated as two shades of gray in top two layers of atoms.

satisfy dangling bonds by bonding with neighbors along a (110) direction. The two atoms in a dimer, however, do not move toward each other equal amounts. One atom is pulled slightly into the surface while the other is pushed out forming a tilted dimer with two possible orientations. The dimers line up in parallel rows and by an ordering of their tilt directions can form higher order reconstructions as shown in figure 2.2. Several

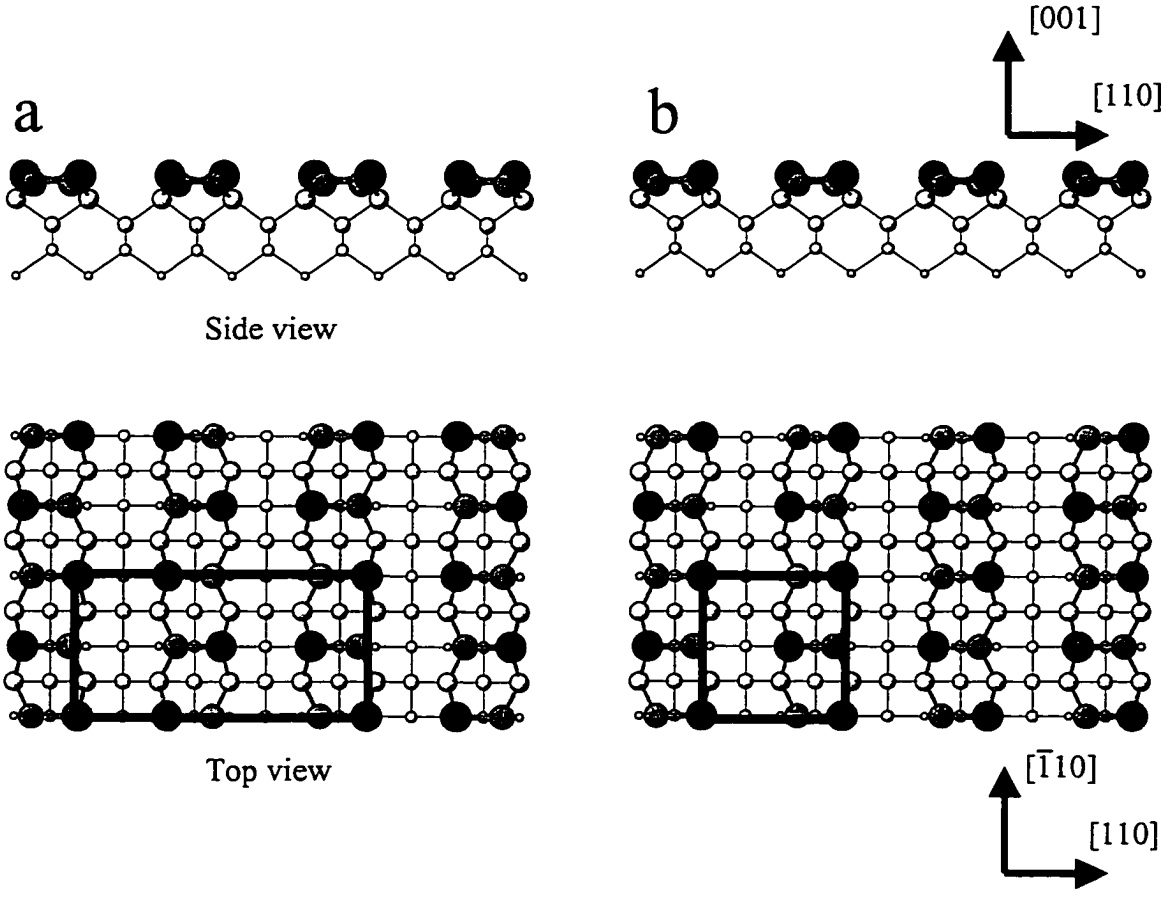

Figure 2.2. Higher order native reconstructions of the Ge(001) and Si(001) surfaces formed by an ordering of the dimer tilt directions. Unit cells are shown in black.
a) c(4x2) b) p(2x2)

room temperature diffraction experiments (Lander and Morrison 1962; Cardillo and Becker 1978; Kevan and Stoffel 1984; Kevan 1985; Culberson, Kuk, and Feldman 1986; Lambert et al. 1987; Lucas et al. 1993) have reported diffuse streaks at p(2x2) and c(4x2) locations indicating that some ordering of the dimer tilts is present along dimer rows. Sharp superstructure spots have only been seen upon cooling down to ~ 200K for Ge(001) (Kevan and Stoffel 1984; Kevan 1985; Lambert et al. 1987; Lucas et al. 1993). Theoretical total energy minimization calculations (Chadi 1979; Ihm et al. 1983; Needels, Payne, and Joannopoulos 1987; Needels, Payne, and Joannopoulos 1988; Spiess, Freeman, and Soukiassian 1994) show either the p(2x2) or c(4x2) structure, figure 2.2, to have the lowest energy, but the experimental investigations indicate that the c(4x2) structure is favored on both Si and Ge.

While early total energy minimization calculations and experimental studies supported the tilted dimer model, the first STM study on Si(001) (Hammers, Tromp, and Demuth 1986) sparked some debate by showing mostly symmetric dimers on the surface. The few dimers that appeared tilted were localized near surface defects. The authors of the STM paper suggested that at room temperature the dimers were flipping orientation rapidly in comparison to the scanning rate, so that the STM images provided a time-averaged representation of an asymmetric dimer. Using the calculated energy difference between a symmetric dimer and a tilted dimer as the energy barrier to be surmounted in a flip, Dabrowski and Scheffler (1992) estimated the flipping rate would

be 10^9 s^{-1} for Si , and Krüger and Pollmann (1995) estimated that for Ge it would be 10^3 times smaller than for Si.

The first detailed experimental structural study on the Ge(001)-(2x1) surface was attempted by Rossmann et al. (1992). This grazing incidence x-ray diffraction experiment reported atomic positions up to 10 layers down from the surface. Since then two more x-ray studies have been reported -- one on Ge(001)-(2x1) (Torrelles et al. 1996) and one on Ge(001)-c(4x2) at 150K (Ferrer et al. 1995). In the following sections a TED study of the room temperature Ge(001)-(2x1) structure is described. The in-plane atomic positions found agree with all three x-ray studies to within a few hundredths of an angstrom. Such a precise experimental consensus allows the Ge(001) surface to serve as a valuable model system for theoretical studies of native surface reconstructions.

2.4.2 Experimental Details

Sample preparation followed the basic procedure outlined in section 1.2.2. The chemical etch consisted of a solution of HNO_3 and HF in a 9 to 1 volume ratio. For the in-situ surface cleaning, an oxygen ion mill (4 kV, 60° from surface normal) followed by an argon ion mill (3 kV, 60° from surface normal) and an anneal at 400 °C for 4 minutes removed most of the surface contamination from the sample. Further cycles of argon ion milling and annealing at 500 °C were used to strengthen the 2x1 surface diffraction spots, and then the diffracted beam intensities were recorded using both film and PEELS

as described in section 2.2. PEELS was used to measure the transmitted beam and the eight strongest bulk diffracted beams.

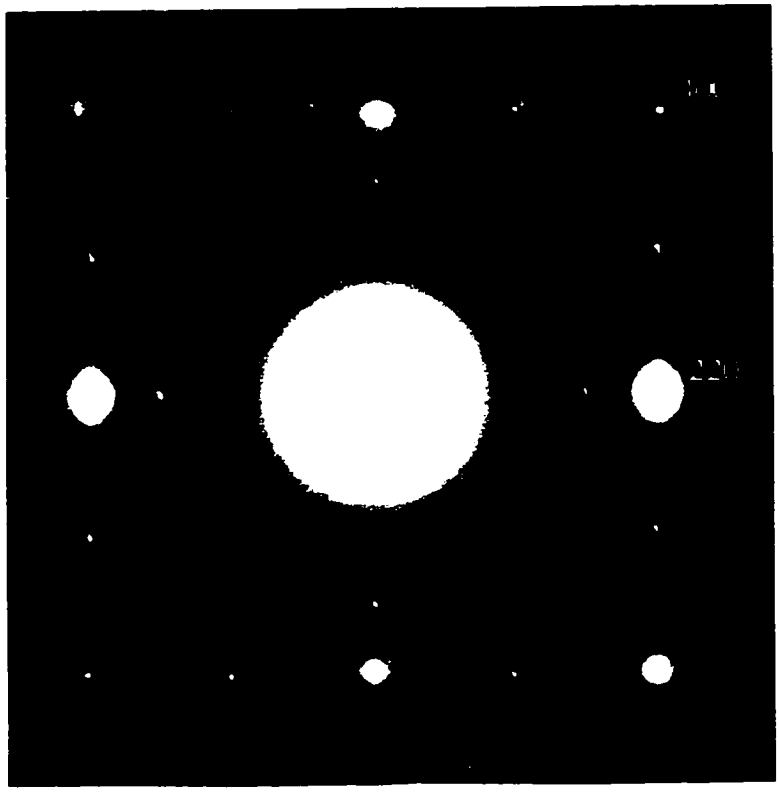

Figure 2.3. Composite of two different exposure time Ge(001)-(2x1) diffraction patterns. The arrowed suface spot is shown in the inset at the top left magnified eight times to show the anisotropic shape due to domain size. Periodic steps on the surface cause the splitting seen in the 1x1 spots.

Figure 2.3 shows the central region of a composite of two digitized diffraction patterns. Reflections from both 2x1 and 1x2 domains are present. The diffraction spots can be separated into three categories: bulk reflections which arise from the bulk diamond cubic germanium lattice, 1x1 reflections having the periodicity of the unreconstructed (001) surface, and pure surface reconstruction reflections which arise

from the 2x1 or 1x2 surface unit cells. The 1x1 spots have intensity contributions from both the surface step structure as well as the surface reconstruction and so were not considered in the analysis. The splitting of the 1x1 spots seen in figure 2.3 indicates a periodic array of steps on the surface spaced about 7 nm apart. While the bulk spots appear round, the surface reconstruction spots are elongated indicating anisotropic surface domain sizes. Since both 2x1 and 1x2 domains must terminate at surface steps and both the 2x1 and 1x2 spots are elongated along the same direction, the anisotropy is most likely due to surface steps running along the direction perpendicular to the elongation of the spots. Because dynamical diffraction calculations were used to refine the model structure, kinematically symmetry equivalent spots were not averaged, and a total of 372 surface intensities appeared in the final data set.

2.4.3 Diffraction Simulation Details

For the multislice calculations each bulk germanium unit cell was cut 4 times along the [001] direction so that a single slice was 0.14 nm thick. TED data is insensitive to displacements parallel to the incident electron beam, and the incident electron beam was nearly perpendicular to the Ge(001) surface, so only displacements parallel to the surface were considered. All of the models tested consisted of either one or two reconstructed unit cells (4 or 8 slices) on both the top and bottom surfaces separated by bulk material.

The initial grid search of the crystal tilt and thickness narrowed the possible thickness down to three ranges near 10 nm, 30 nm, and 60 nm. As mentioned in section 2.2 an independent thickness estimate can be made by analyzing the PEELS spectrum of the transmitted beam with the relation, $t/\lambda=\ln(I_t/I_o)$, where t is the thickness, λ is the inelastic mean free path, I_t is the total number of electrons in the spectrum, and I_o is the number of electrons in the zero loss peak (Malis, Cheng, and Egerton 1988). An effective inelastic mean free path for the Ge sample (dependent on the detector collection angle) was measured by gathering convergent beam electron diffraction patterns (CBED) and PEELS data from relatively thick regions to define the relationship between t and $\ln(I_t/I_o)$. By analyzing the structure in CBED patterns one can measure crystal thickness very precisely (Allen and Hall 1982), but for thin samples (a few tens of nanometers) there is less structure in the CBED images and the technique becomes less precise. Nevertheless, by concentrating on thicker regions of the sample, the CBED technique provided accurate thickness measurements which could be correlated with PEELS measurements to find λ. A linear relationship between t and $\ln(I_t/I_o)$ was verified (figure 2.4), and a value of 224 nm was found for λ. Using this value for λ, the PEELS spectra indicated a thickness near 10 nm for the region from which the surface diffraction data was taken. Finally, a numerical R-factor minimization refined the values for the thickness and tilt to 7.6 nm and 100 mrad respectively. An overall scaling term included in the R-factor fit was 2.5, indicating a reasonable agreement between the absolute magnitudes of the measured and simulated intensities.

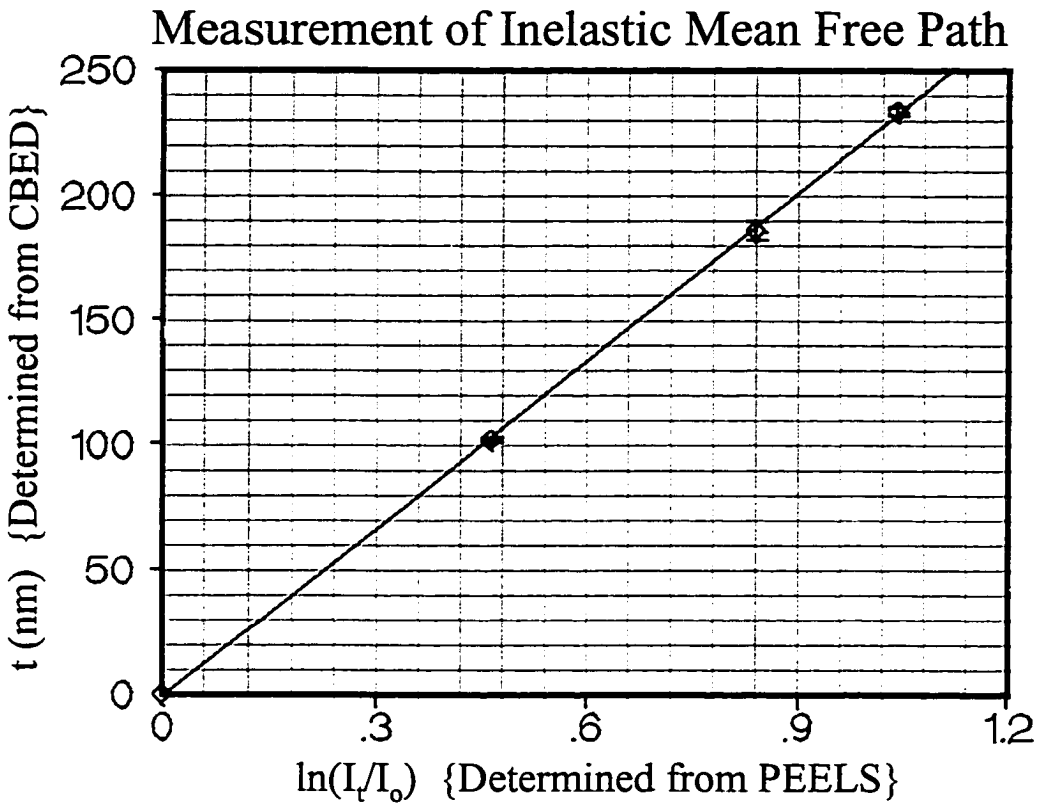

Figure 2.4. Plot of $\ln(I_t/I_o)$ vs. thickness measured with CBED. The straight line is y=224x, indicating an effective inelastic mean free path of 224 nm.

In all the models considered, both 2x1 domains and 1x2 domains were assumed to exist on the top and bottom surfaces, requiring four separate multislice calculations for each iteration of the minimization program. The four calculations were averaged together to form the final simulated diffraction intensities. The relative weightings of the four calculations in the final average were included as four additional fitting parameters. In agreement with Rossmann et al. (1992) and Torrelles et al. (1996) the best fit model for our data was a disordered array of buckled dimers shown in figure 2.1. The random disorder in buckling direction was simulated by including both possible

dimer orientations in a unit cell with a 1/2 fractional occupancy. The fractional occupancy was simulated in only the first two layers of atoms. Isotropic Debye-Waller factors for the first two layers were also included in the fit, and the factors for all other layers were fixed at the bulk value.

A reduced χ^2 was initially used as a measure of the goodness of fit. For the best fit model a χ^2 value of 2.36 was found. With 372 data points in the fit, the probability is infinitesimally small that the model is completely correct, all of the error estimates are accurate, and the value of χ^2 would be 2.36. As mentioned in section 2.3.1, a key assumption in a χ^2 analysis is that the errors between the measurements and the simulation have gaussian distributions. Figure 2.5 is a plot of the distribution of errors

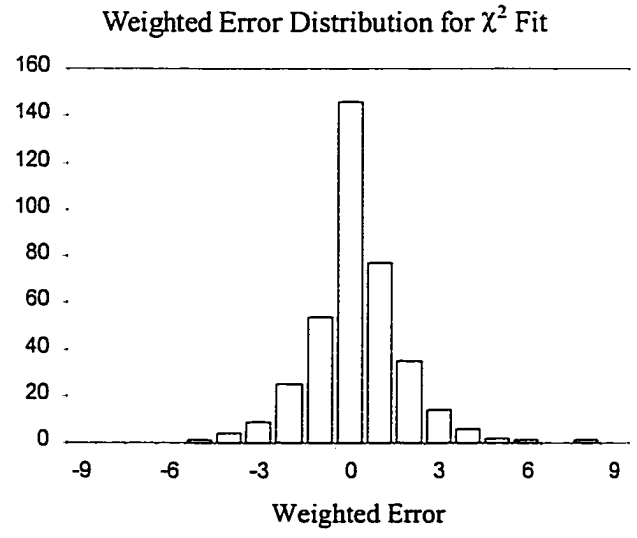

Figure 2.5. Distribution of weighted errors for the 372 simulated reflections in the χ^2 fit.

for the χ^2 fit. Instead of being gaussian, the distribution is much closer to an exponential distribution of the form exp(-|x|), so the use of a χ^2 analysis cannot be justified in this case. Instead, a χ value was employed to decrease the sensitivity to the outlier points during the structure refinement.

2.4.4 Discussion of Refinement Results

The atom positions for the best-fit model are shown in table 2.1 along with the results of three x-ray studies. The Debye-Waller factors for layers one and two were 3.9 times and 2.5 times the bulk Ge value respectively. While both χ^2 and χ factors were calculated, only the results for the χ minimization are shown as explained above. In any case, the atom positions only differed by at most a couple hundredths of an angstrom between the two treatments. The χ value for the fit shown is 1.10. Although the magnitudes of the atom displacements in the 5th and 6th layers are only 0.005 nm and 0.004 nm respectively, they had a significant effect on the goodness of fit. For a model with only the first two layers allowed to move, the lowest χ value obtained was 1.63. Including the 5th and 6th layer displacements in the model dropped the χ value down to 1.10. For comparison, the χ^2 value in the same case fell from 5.64 to 2.36. Other models for the reconstruction were tested including a symmetric dimer and an ordered array of tilted dimers, but none provided an adequate fit.

Table 2.1 Comparison of Experimental Results for Ge(001)-(2x1) Structure

TED study	**Rossmann et al. (1992)**	**Torrelles et al. (1996)**		**Ferrar et al. c(4x2) (1995)**	
372 in-plane.	42 in-plane averaged to 13. 71 out-of plane.	126 in-plane averaged to 48. 428 out-of-plane averaged to 242.		46 in-plane 165 out-of-plane. (no 2x1 beams included).	
X	**X**	**X**	**Y**	**X**	**Y**
0.123	0.129	0.120	0.0*	0.1210	0.0*
0.421	0.422	0.427	0.0*	0.4216	0.0*
0.017	-0.007	0.001	0.5*	0.0164[a]	0.529[b]
0.490	0.458	0.476	0.5*	0.4836[a]	0.471[b]
0.25*	0.25*	0.25*	0.5*	0.25*	0.5*
0.75*	0.75*	0.75*	0.5*	0.75*	0.5036
0.25*	0.25*	0.25*	0.0*	0.2526	0.0*
0.75*	0.75*	0.75*	0.0*	0.75*	0.0*
-0.0061[a]	-0.009[a]	-0.0047[a]	0.0*		
0.5061[a]	0.509[a]	0.5047[a]	0.0*		
-0.0052[b]	-0.004[b]	-0.0021[b]	0.5*		
0.5052[b]	0.504[b]	0.5021[b]	0.5*		

Notes: The size of the data set in each study is indicated at the top of each column, with averaging over kinematically symmetry-equivalent reflections. As explained in the text no symmetry averaging was done in the current study, and all of the reflections measured in the study by Ferrar et al. were non-symmetry related. Numbers are in terms of the (2x1) unit cell with X_o=8 angstroms and Y_o=4 angstroms. The atom positions from the c(4x2) study of Ferrar et al. have been reduced relative to this same (2x1) notation so direct comparisons can be made.

* a parameter that is fixed.

[a,b] two parameters that are symmetry related.

Overall the agreement between the experimental studies is excellent. If one averages the values found in the four studies for each atom position, one finds that for almost every position the largest deviation from the average occurs in the study by

Rossmann et al. (1992). This can be attributed to the relatively smaller data set size measured in that study. The positions for the first dimerized layer are all within 0.007 nm of each other, and even though the individual second layer positions show some more scatter (0.024 nm) the distances between the two second layer atoms all agree to within 0.008 nm. It is not surprising that the relative separation of atoms in a given layer are determined more accurately than the individual atom positions, since the thermal vibrations of neighboring atoms are likely to be correlated. While the vibration amplitude for a given atom could be relatively large near the surface, its vibrational amplitude relative to its neighbor would be significantly less.

It is interesting to note the close agreement for the dimer structure between the room temperature (2x1) studies and the 150K c(4x2) study. Northrup (1993) reported a similar agreement between room temperature photoemission measurements and the surface band structure calculated for the Si(001)-c(4x2) reconstruction. He pointed out that the agreement suggests a strong correlation of dimer tilt directions along a dimer row. In fact, many studies have provided evidence for correlated buckling of dimers at room temperature. Several studies have shown that in the formation of higher order reconstructions, the dimer interaction along a dimer row is much stronger than the interaction between rows (Kevan 1985; Lucas et al. 1993; Ferrer et al. 1995). In STM studies (Hammers, Tromp, and Demuth 1986; Kubby et al. 1987; Wang, Arias, and Joannopoulos 1993; Yang et al. 1994) some rows of alternating tilted dimers can be seen. Other diffraction studies have shown diffuse streaks through c(4x2) positions

indicating that some short range ordering is taking place (Lander and Morrison 1962; Cardillo and Becker 1978; Kevan and Stoffel 1984; Kevan 1985; Culberson, Kuk, and Feldman 1986; Lambert et al. 1987; Lucas et al. 1993). In our data the c(4x2) streaks were also seen on the longer exposure time negatives (fig. 2.6). A temperature dependent x-ray study by Lucas et al. (1993) indicated that the alternating tilting continues for about 8 nm (20 unit cells) along dimer rows at room temperature. Based

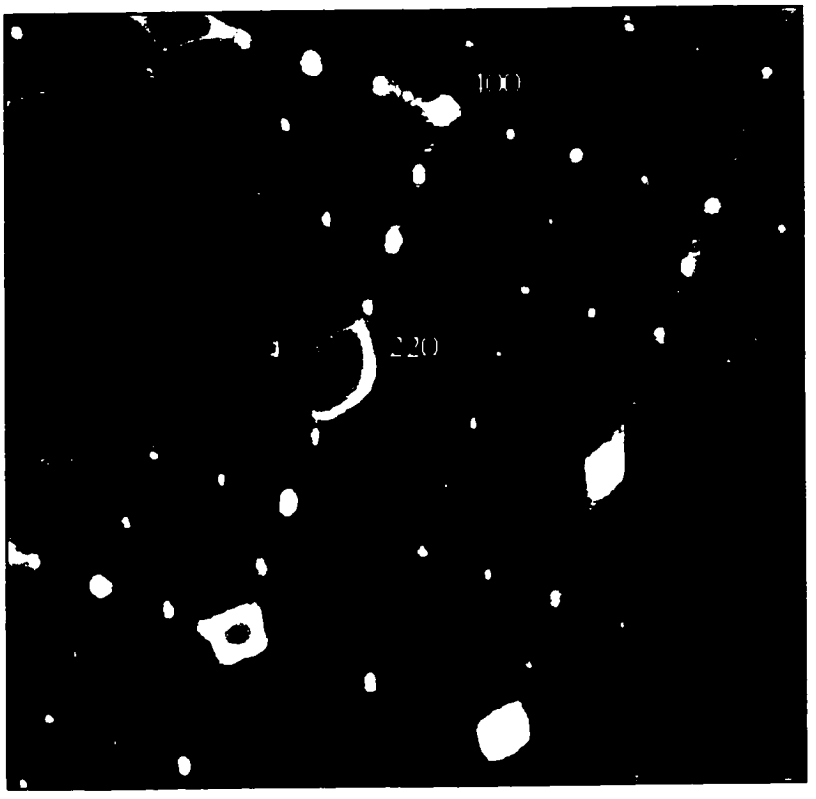

Figure 2.6. Ge(001)-(2x1) diffraction pattern that has been high-pass filtered to highlight the c(4x2) diffuse streaks. Arrows indicate two streaks passing through c(4x2) locations.

on temperature dependent photoelectron spectroscopy measurements, Landemark et al. (1994) have argued that the room temperature Ge(001)-2x1 and Si(001)-2x1 surfaces should actually be viewed as disordered c(4x2) surfaces. The similarity between the (2x1) dimer and the c(4x2) dimer seen in table 2.1 provides further evidence for the correlation of tilt directions along dimer rows.

Table 2.2 Comparison of Theoretical Results for Ge(001)-(2x1) Structure

Needels, Payne, and Joannopoulos (1987)	**Pollmann, Krüger, and Mazur (1987)**	**Spiess, Freeman, and Soukiassian (1994)**	
X	**X**	**X**	**Y**
0.1507	0.1404	0.1408	0.0*
0.4475	0.4423	0.4408	0.0*
0.0208	0.0069	0.0045	0.5*
0.4971	0.4933	0.4889	0.5*
0.2629	0.2451		0.5*
0.7566	0.7551		0.5*
0.25	0.25		0.0*
0.75	0.75		0.0*

Note: Positions are in terms of the (2x1) unit cell as in Table 2.1.

* denotes a parameter that is fixed.

The results of the three theoretical studies (Needels, Payne, and Joannopoulos 1987; Pollmann, Krüger, and Mazur 1987; Spiess, Freeman, and Soukiassian 1994) reporting atomic positions are shown in table 2.2. Both theory and experiment indicate a projected dimer bond length of 0.240 nm. All of the studies lie within 0.006 nm of this value. However, the theoretical calculations tend to overestimate the asymmetry of the dimer. Looking at the x position for the first atom in the dimer, one sees that the

experimental results range from 0.096 nm to 0.103 nm while the theoretical results range from 0.112 nm to 0.121 nm. This discrepancy is possibly due to differences in modeling. In each case the experimental data were fit best by a disordered array of buckled dimers, while in the theoretical (2x1) calculations a perfectly ordered array of dimers had to be assumed with all the dimers tilting in the same direction. Two of the theory studies (Needels, Payne, and Joannopoulos 1987; Spiess, Freeman, and Soukiassian 1994) also considered the c(4x2) structure. With its alternating dimer tilts the c(4x2) offers a more accurate description of the room temperature surface than a true (2x1) structure with all the dimers tilting the same way. The c(4x2) results are shown in table 2.3, and one can see that the values obtained by Needels et al. provide the best theoretical match to the experimentally determined structure.

Table 2.3 Comparison of Theoretical Results for Ge(001)-c(4x2) Structure

Needels, Payne, and Joannopoulos (1987)		**Spiess, Freeman, and Soukiassian (1994)**	
X	**Y**	**X**	**Y**
0.1174	-0.0067	0.1381	0.0
0.4112	-0.0049	0.4414	0.0
0.0087	0.4694	0.0078	0.5185
0.4839	0.5138	0.4922	0.4815
0.2467	0.5050		
0.7490	0.5013		
0.25	0.0		
0.75	0.0		

Note: Positions have been reduced relative to a (2x1) unit cell as in table 2.1.

In view of the experimental evidence, the lateral displacements in the Ge(001)-(2x1) structure can be regarded as known with a high degree of confidence. Four independent studies employing two distinct experimental techniques have reported atom positions for the first 6 layers. The positions agree to within a few hundredths of an angstrom. It was shown that the best agreement between the experimentally determined structure and a theoretical calculation was for a calculation assuming a full c(4x2) unit cell. When taken with the extensive experimental evidence for correlated buckling at room temperature, this suggests that for theoretical structure calculations of the Ge(001)-(2x1) surface, the surface may be best modeled with a c(4x2) unit cell.

CHAPTER 3: DIRECT METHODS FOR DETERMINING SURFACE STRUCTURES

The standard diffraction analysis method discussed in chapter 2 in which measured intensities are compared to those simulated from a trial model is a powerful but limited approach. If the number of possible structures can be restricted to just a few, then intensity fitting is excellent for differentiating between the possibilities and refining the atom positions to a high degree of precision once the correct structure is known. Unfortunately there are usually too many possible structures to all be compared to the measured diffraction intensities.

This chapter describes alternative ab-initio approaches to analyzing surface diffraction data known as direct methods. Direct methods can be used to determine the basic geometry of a surface reconstruction without any prior knowledge other than the symmetry elements present in the structure. Traditional intensity simulations can then be used to refine the atomic positions. Sections 3.1 and 3.2 describe the general direct methods approach used to analyze diffraction data, and section 3.3 illustrates the application of direct methods to the case of the previously unknown Ge(111)-(4x4)/Ag surface structure.

3.1 Introduction to Direct Methods

A surface structure can be represented by a two-dimensional function, f(**r**), where **r** = x**a** + y**b**. Rather than directly giving real-space information about f(**r**), diffraction experiments yield information about its Fourier transform, F(**h**), where **h** = h**a*** + k**b***, and **a*** and **b*** are unit vectors in reciprocal space. F(**h**) is a complex quantity which can be written in terms of its amplitude, |F(**h**)|, and phase, ϕ(**h**), as F(**h**) = |F(**h**)| exp[iϕ(**h**)]. Measured diffraction intensities, I(**h**), determine the amplitude of F(**h**) through the relation, I(**h**) = |F(**h**)|^2, but the phase remains unknown. If the phase was known then F(**h**) would be completely determined, and f(**r**) could be solved by inverse Fourier transforming F(**h**). The problem of finding the unmeasured phases is referred to as the "phase problem" of diffraction analysis, and it is the central concern of direct methods.

Direct methods use the amplitude measurements and other a-priori information about f(**r**) (e.g. it is non-negative, it consists of strong peaks localized at atom sites, or it is zero over a finite region) to obtain estimates for the phase. Direct methods approaches can be classified into two categories which are described in the next two sections. Section 3.1.1 discusses approaches which are based on probability relationships which exist between the amplitude and the phase, and section 3.1.2 covers approaches which use iterative mathematical projections.

3.1.1 Probabilistic Approaches

Probabilistic approaches to phase determination were the first successful direct methods, and they were developed entirely within the context of crystallography. In crystallography f(**r**) is periodic and consists of a discrete number of atoms within a unit cell. Therefore F(**h**) is zero everywhere except at isolated points where h and k are integers (**a*** and **b*** in this context are the reciprocal lattice vectors). F(**h**) is referred to as the structure factor and can be written in terms of the positions of atoms within the unit cell as,

$$F(\bar{h}) = \sum_{j=1}^{N} f_j \exp\left[2\pi i(\bar{h}\cdot\bar{r}_j)\right] \qquad (3.1)$$

where N is the number of atoms in the unit cell, f_j is the scattering factor for the j^{th} atom, and $\mathbf{r}_j$ represents the position of the j^{th} atom within the unit cell. The scattering factors themselves are decreasing functions of $|\mathbf{h}|$, so structure factors for large values of **h** will be small. It is common in crystallographic direct methods to scale the structure factors by the largest value F(**h**) can take, $\sum f_j$. The scaled structure factors are referred to as unitary structure factors (Woolfson 1961, 2) and are denoted by,

$$U(\bar{h}) = \sum_{j=1}^{N}\left(f_j \Big/ \sum_{\ell=1}^{N} f_\ell \right) \exp\left[2\pi i(\bar{h}\cdot\bar{r}_j)\right] = \sum_{j=1}^{N} n_j \exp\left[2\pi i(\bar{h}\cdot\bar{r}_j)\right] \qquad (3.2)$$

where n_j is called a unitary scattering factor. Defined in this way $|U(\mathbf{h})|$ must lie between 0 and 1.

Harker and Kasper (1948) were the first to show that knowledge of structure factor magnitudes could give information about structure factor phases in some cases. Using Cauchy's inequality they showed that for a centrosymmetric crystal (a crystal with an inversion center),

$$U^2(\bar{h}) \leq \frac{1}{2}\left[1 + U(2\bar{h})\right] \qquad (3.3)$$

With an inversion center all structure factors are forced to be real, and phase determination becomes a problem of sign determination. The term on the left of the inequality must be positive and could be large for a particular **h**. If |U(2**h**)| also happens to be large, then the sign of U(2**h**) could be determined to be positive in order to satisfy equation 3.3. For example, if |U(**h**)| = 0.7 and |U(2**h**)| = 0.6, then equation 3.3 gives 0.49 $\leq$ 1/2 [1 $\pm$ 0.6], and U(2**h**) must be positive for equation 3.3 to be true.

In 1952 Sayre took another approach by considering the fact that the electron density, f(**r**), consisted of non-overlapping atoms. If f(**r**) is squared, then the atom sites become more sharply defined, but they remain in the same positions. As a consequence the phases of the structure factors will remain unchanged since they only depend on the position of the atoms and not their shapes. Using this fact and the convolution theorem, Sayre derived his equation (Sayre 1952),

$$F(\bar{h}) = \frac{\theta(\bar{h})}{V}\sum_{\bar{k}} F(\bar{k})F(\bar{h}-\bar{k}) \qquad (3.4)$$

where V is the volume of the unit cell and $\theta(\mathbf{h})$ is the ratio of the normal scattering factor to the effective scattering factor for the squared atoms. Multiplying both sides of equation 3.4 by $F(-\mathbf{h})$ gives,

$$|F(\bar{h})|^2 = \frac{\theta(\bar{h})}{V}\sum_{\bar{k}} F(-\bar{h})F(\bar{k})F(\bar{h}-\bar{k})$$

$$= \frac{\theta(\bar{h})}{V}\sum_{\bar{k}} |F(-\bar{h})||F(\bar{k})||F(\bar{h}-\bar{k})|\exp\{2\pi i[\phi(-\bar{h})+\phi(\bar{k})+\phi(\bar{h}-\bar{k})]\} \qquad (3.5)$$

Equation 3.5 is valid for both centrosymmetric and non-centrosymmetric crystals, and it illustrates an important relationship between the amplitudes and the phases of vector-related structure factor triplets.

The Argand diagram in figure 3.1 shows the relationship geometrically. The left side of equation 3.5 is real and positive and it is indicated by a thick black arrow in figure 3.1. The sum on the right side of the equation is represented by the thinner arrows in figure 3.1 joined head to tail. If $|F(\mathbf{h})|$ is relatively large, and the magnitudes of $|F(\mathbf{k})|$ and $|F(\mathbf{h}-\mathbf{k})|$ also happen to be large for a particular value of $\mathbf{k} = \mathbf{k}_1$, then the sum will be dominated by the $\mathbf{k}_1$ term. The dominant $\mathbf{k}_1$ term is shown as a gray arrow in the Argand diagram. If equation 3.5 is to be satisfied, then the series of arrows representing the right hand side of equation 3.5 must end on the tip of the $|F(\mathbf{h})|^2$ vector. This is impossible unless the vector corresponding to the dominant $\mathbf{k}_1$ term lies close to the real axis. This implies that the angle between the real axis and the $\mathbf{k}_1$ vector, $\phi(-\mathbf{h}) + \phi(\mathbf{k}_1) + \phi(\mathbf{h}-\mathbf{k}_1)$, is close to zero.

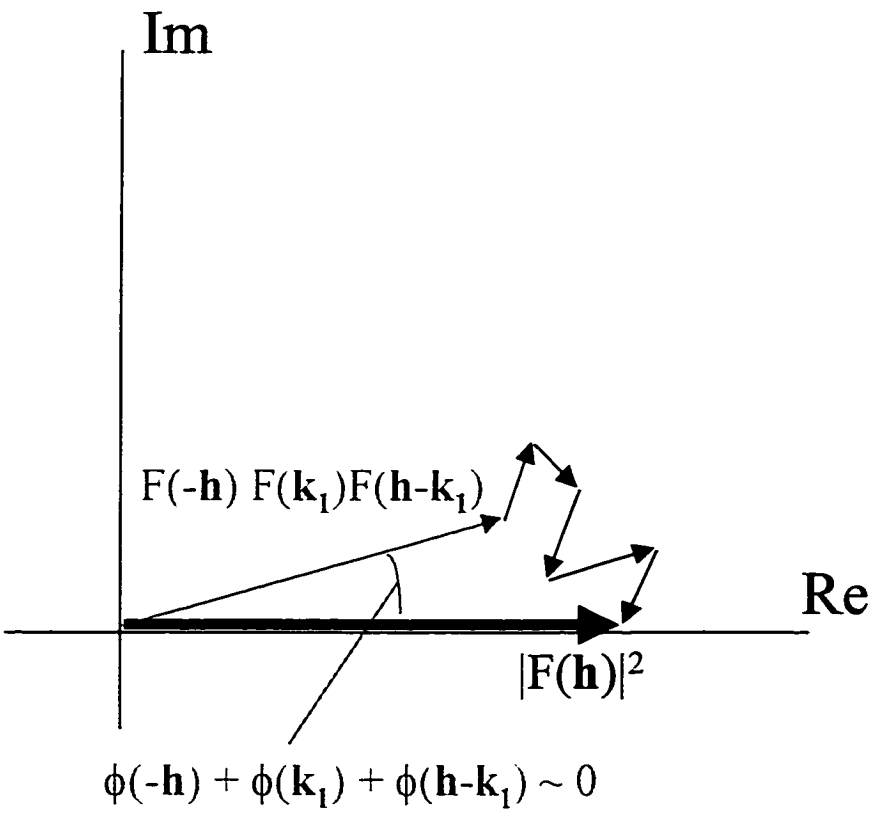

Figure 3.1 An Argand diagram illustrating the relationship, $\phi(-\mathbf{h}) + \phi(\mathbf{k}_1) + \phi(\mathbf{h}-\mathbf{k}_1) \sim 0$ when $|F(\mathbf{h})|$, $|F(\mathbf{k}_1)|$, and $|F(\mathbf{h}-\mathbf{k}_1)|$ are all large.

One can state the relationship between the phases $\phi(-\mathbf{h})$, $\phi(\mathbf{k})$, and $\phi(\mathbf{h}-\mathbf{k})$ in terms of probabilities if one asks the following question: given $|F(\mathbf{h})|$, $|F(\mathbf{k})|$, and $|F(\mathbf{h}-\mathbf{k})|$ what is the probability distribution for the sum, $\phi(-\mathbf{h}) + \phi(\mathbf{k}) + \phi(\mathbf{h}-\mathbf{k})$? Cochran derived this probability distribution (1955) and showed that the distribution is always centered around zero degrees and can become sharply peaked for large values of the amplitudes. Since $\phi(-\mathbf{h}) = -\phi(\mathbf{h})$, the relationship, $\phi(-\mathbf{h}) + \phi(\mathbf{k}) + \phi(\mathbf{h}-\mathbf{k}) \sim 0$, can be rewritten as $\phi(\mathbf{h}) \sim \phi(\mathbf{k}) + \phi(\mathbf{h}-\mathbf{k})$. In this form the relationship becomes useful for phase extension. If the phases of two reflections, $\mathbf{k}$ and $(\mathbf{h}-\mathbf{k})$, are known, then the phase of the reflection which

is the vector sum of the first two reflections, $\mathbf{h} = \mathbf{k} + (\mathbf{h}-\mathbf{k})$, is approximately equal to the sum of the two known phases. The probability that the phase assignment for $\phi(\mathbf{h})$ is correct can be calculated, and the probability increases with increasing amplitudes for the three involved reflections.

To find phases for a set of measured amplitudes, one can start by picking a few strong reflections and giving them phases. From this basis set the phases can be extended to get estimates for the phases of all measured reflections. The problem of phase extension quickly becomes one of self-consistency, however. For any given reflection, **h**, there are likely to be a number of pairs of vectors which give phase estimates for **h**. One must find a way to search through all possible basis sets of phases to find the ones which give the most self-consistent estimates for all reflections.

Going back to Sayre's original observation that structure factor phases should remain unchanged when $f(\mathbf{r})$ is squared, self-consistency can be looked at from a different perspective. A given set of phase estimates can be checked by squaring the corresponding $f(\mathbf{r})$ and checking to make sure that the phases of the structure factors for $f^2(\mathbf{r})$ have remained essentially unchanged. This approach is closely related to iterative projection methods which are discussed in the next section.

3.1.2 Projection Methods

The phase problem is not limited to crystallography, and similar challenges of finding either unmeasured phase information or unmeasured amplitude information exist

in many fields dealing with signal and image recovery. Progress in these areas has been made with iterative methods involving projections onto sets. In this context a set, denoted by S_1, consists of a group of functions which satisfy given constraints. A projection onto S_1 is accomplished through a projection operator, denoted by P_1, which can be applied to any given function, g(x), and will produce an output function which is the member of S_1 closest to g(x). For example, S_1 could be defined as the set of all functions of the variable, x, which are zero for $-\infty < x \leq 0$. Then the associated projection operator, P_1, would be defined by its action on a general function g(x) as: $P_1g(x) = 0$ for $-\infty < x \leq 0$, and $P_1g(x) = g(x)$ for $0 < x < \infty$.

In the language of projections, the problem of retrieving phase or amplitude information is stated as a problem of finding the intersection of m sets, S_1 S_2 . . . S_m. Usually m = 2 with S_1 consisting of all functions which satisfy all of the known real-space constraints, and S_2 consisting of all functions which satisfy all reciprocal-space constraints. A member of the intersection of S_1 and S_2 will be an answer to the problem as posed since it will satisfy every given constraint. To find the intersection an iterative algorithm is used in which $f_{n+1} = P_2P_1f_n$, where n is the iteration number. This simple iterative sequence has been shown to have strong convergence to the intersection of S_1 and S_2 if both sets are convex (Youla 1987). A set is convex if together with any $f_1(\mathbf{r})$ and $f_2(\mathbf{r})$, it also contains $\mu f_1(\mathbf{r})+(1-\mu)f_2(\mathbf{r})$ for all μ, $0 \leq \mu \leq 1$ (Youla 1987).

Unfortunately, the constraint of knowing only the amplitude information about a function is not a convex constraint, so for the crystallographic phase problem strong

convergence cannot be assured. However, for the general case of non-convex sets Levi and Stark (1984) have defined a summed-distance error as,

$$J(f_n) \equiv \int \{|P_1 f_n - f_n| + |P_2 f_n - f_n|\} \qquad (3.6)$$

and they proved that $J(f_{n+1}) \leq J(f_n)$. Therefore, even without convex sets, the iterative sequence of, $f_{n+1} = P_2 P_1 f_n$, can at worst only stagnate.

In practice, projection methods have been quite successful. An early example is due to Gerchberg and Saxton (1972) who developed a method to recover phase information from TEM images and diffraction measurements. The Gerchberg-Saxton algorithm is illustrated schematically in figure 3.2. A real-space TEM image gives amplitude information, $|f_T(\mathbf{r})|$, about the real-space function, $f(\mathbf{r})$, and a diffraction pattern gives information about the amplitude of the Fourier transform of $f(\mathbf{r})$ in reciprocal space, $|F_T(\mathbf{h})|$, where the subscript "T" is used to denote the fact that these amplitudes are taken to be the true values (neglecting measurement errors) for the sampled object, $f(\mathbf{r})$. To find the phase information in both domains, one starts out by randomly assigning phases, $\theta(\mathbf{r})$, to the measured real-space amplitudes. A Fourier transform then takes the function, $|f_T(\mathbf{r})| \exp[2\pi i\theta(\mathbf{r})]$, to the Fourier domain where it becomes, $|F(\mathbf{h})| \exp[2\pi i\phi(\mathbf{r})]$. Note that in general $|F(\mathbf{h})| \neq |F_T(\mathbf{h})|$ since the $\theta(\mathbf{r})$ are in general not the correct phases, $\theta_T(\mathbf{r})$. Therefore, the amplitudes of the Fourier domain function are corrected to their measured values giving the new function, $|F_T(\mathbf{h})| \exp[2\pi i\phi(\mathbf{r})]$. An inverse Fourier transform takes this corrected function back to the

real-space domain where it becomes, $|f(\mathbf{r})| \exp[2\pi i\theta(\mathbf{r})]$. Again the real-space amplitudes are corrected to the measured values, and the whole cycle repeats itself.

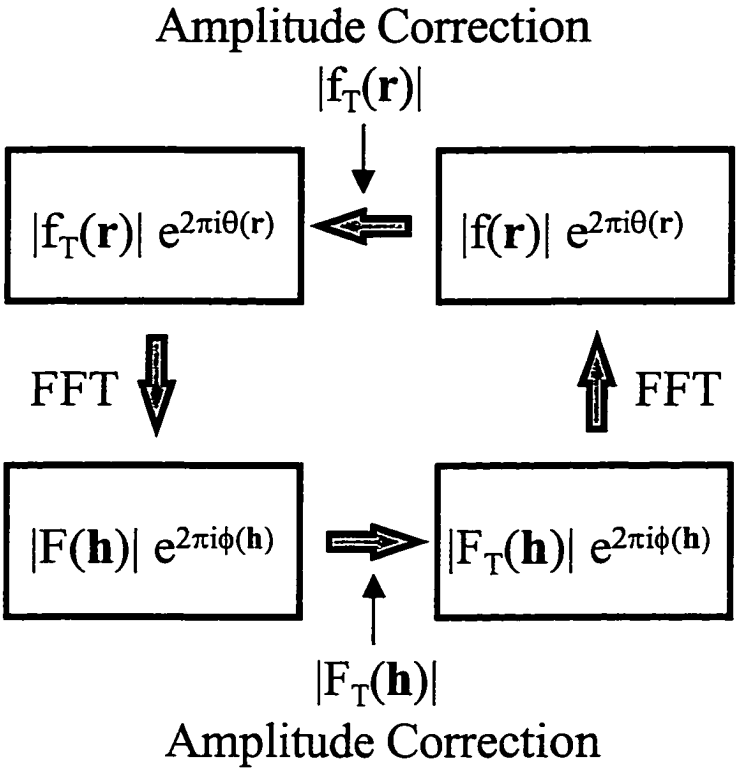

Figure 3.2. Diagram of the Gerchberg-Saxton algorithm.

For the Gerchberg-Saxton algorithm S_1 is the set of all functions whose real-space amplitudes equal $|f_T(\mathbf{r})|$, and S_2 is the set of all functions whose Fourier transform amplitudes equal $|F_T(\mathbf{h})|$. Gerchberg and Saxton defined a squared error as the sum of the squared differences between the measured amplitudes and the amplitudes generated after a Fourier transform operation during an iteration. They offered a geometrical proof that the squared error can never increase after a Fourier transform step in their algorithm.

The squared error will continually decrease, or at worst stay constant. They also showed that for test cases, the algorithm was effective at finding estimates of $\theta_T(\mathbf{r})$ and $\phi_T(\mathbf{h})$ such that the squared error closely approached zero.

3.2 Direct Methods for Solving Surface Structures

3.2.1 Challenges With Surface Diffraction Data

The probabilistic approaches to direct methods described in section 3.1.1 have been enormously successful in the field of bulk x-ray crystallography. The importance of the methods to the field was recognized when Hauptmann and Karle were awarded the 1985 nobel prize in chemistry for their contributions to the development of direct methods. Surprisingly, the application of direct methods to two-dimensional surface diffraction data has only been realized during the past two years through work done in our lab at Northwestern (Marks, Plass, and Dorsett 1997; Landree, Collazo-Davila, and Marks 1997; Gilmore et al. 1997; Marks and Landree 1998; Marks et al. 1998). The delay in applying direct methods in the field of surface science may be due in part to the unique challenges encountered in working with surface diffraction data.

For a bulk crystal, all of the intense reflections can be measured. A surface reconstruction however, resides on top of a bulk substrate which produces much stronger diffracted beams than the thin surface structure. Unless the surface structure is incommensurate with its substrate, which is uncommon, the bulk reflections will overlap the surface reflections at many points in reciprocal space. Since the bulk diffraction

intensities are much stronger than the surface diffraction intensities, the surface reflections cannot be separated from overlapping bulk reflections and therefore will go unmeasured. If one of the unmeasurable surface reflections happens to be a relatively strong reflection for the surface structure, then the probabilistic approach of phase determination will run into difficulties since it depends heavily on relationships between the large-amplitude structure factors. We have found that projection methods are more robust at handling data sets with unmeasured amplitudes, and they can even be used to interpolate amplitude values for the unmeasured reflections while still restoring the phase information.

Another challenge in analyzing surface diffraction data arises from the fact that measurements are usually made of only in-plane reflections. Therefore while the data are purely two-dimensional, the actual surface structure may consist of a few layers of atoms located at different heights above the substrate. The restored map of the atom positions will represent a projection of the surface structure onto a plane parallel to the surface, and the height of the atoms above the substrate will be unknown. Related to this height ambiguity is the problem that the registry of the surface structure relative to the substrate crystal lattice is also unknown. These difficulties are largely ones of interpretation in dealing with the two-dimensional projections of the surface atomic positions. In practice, various educated guesses about the registry of surface atoms can be tested through intensity simulation and refinement. The validity of guesses about the

height of atoms can only be evaluated by examining other available experimental measurements made on the particular surface structure.

3.2.2 Details of the Projection Method

As mentioned in section 3.2.1, work in our lab has shown that a method related to projections works best for phase determination with surface diffraction data. In the specific algorithm we use, modified unitary structure factors are defined as, $U(\mathbf{h}) = W(\mathbf{h})F(\mathbf{h})/\langle f^2(\mathbf{h})\rangle^{1/2}$, where $W(\mathbf{h})$ is a window function included to reduce truncation effects in the calculation of the Fourier transforms and can also be viewed as acting as a pattern recognition component for atom-like features (Marks et al. 1998). Since the unitary structure factors are used throughout the algorithm, the corresponding real-space function will be denoted by $u(\mathbf{r})$, emphasizing the fact that the amplitudes of its Fourier transform are the unitary structure factor amplitudes. Operators are defined as,

$$P_1 u(\bar{r}) = \begin{cases} 0 & \{u(\bar{r}) < 0\} \\ u(\bar{r}) \ln\left[u(\bar{r})/\langle u(\bar{r})\rangle\right] & \{u(\bar{r}) > 0\} \end{cases} \tag{3.7}$$

$$P_2 U(\bar{h}) = P_2 \left\{|U(\bar{h})|\exp[2\pi i\phi(\bar{h})]\right\} = |U_T(\bar{h})|\exp[2\pi i\phi(\bar{h})] \tag{3.8}$$

where $|U_T(\mathbf{h})|$ are the measured unitary structure factors. The function, $u(\mathbf{r})\ln[u(\mathbf{r})/\langle u(\mathbf{r})\rangle]$, seen in equation 3.7 acts as a sharpening operator in the same sense as the squaring operation discussed by Sayre (1952). Therefore, for non-overlapping atoms, the phases of $u(\mathbf{r})$ and of $u(\mathbf{r})\ln[u(\mathbf{r})/\langle u(\mathbf{r})\rangle]$ will be the same. The function is also

related to the relative entropy, $S_{rel} = \sum_r [u(\mathbf{r}) \ln\{u(\mathbf{r})/e\langle u(\mathbf{r})\rangle\} + \langle u(\mathbf{r})\rangle]$, which is discussed in information theory (Cover and Thomas 1991). The algorithm defined by the operators, P_1 and P_2 above, can be shown to minimize the relative entropy (Marks and Landree 1998).

The progress of the algorithm is monitored with a figure of merit (FOM) which is a scaled version of the summed-distance error discussed by Levi and Stark (1984),

$$FOM = \sum_{\bar{h}\neq 0} |U_{n+1}(\bar{h}) - \alpha U_n(\bar{h})| / |U_{n+1}(\bar{h})| \qquad (3.9)$$

where α is chosen to minimize equation 3.9. For the correct solution with no measurement errors the FOM will be zero. In practice, it is found to be about 0.1 to 0.2 for accurate estimates of the phases.

3.2.3 Genetic Algorithm

To begin the iterative algorithm described in section 3.2.2, a set of starting phases must be assigned to the measured unitary structure factors. For each new set of starting phases the algorithm may converge to a different point. This is a consequence of the non-convex nature of the sets and of measurement errors. Rather than the existence of one unique point of intersection between the real-space constraints and the reciprocal-space constraints, there are likely to be a number of local minimum approach distances between the two sets. The true solution which is being sought could in general be any one of these local minima.

We use a genetic algorithm to globally search through all possible sets of starting phases to find those sets which lead to the various local minima (Landree, Collazo-Davila, and Marks 1997). The genetic algorithm encodes sets of starting phases as binary strings of 1's and 0's. A single binary string corresponding to one complete set of starting phases is referred to as a chromosome. For a given "population" of chromosomes, an FOM is calculated for each chromosome by running the iterative projection algorithm for each set of starting phases and keeping track of the summed-distance error FOM (equation 3.9). A new population of chromosomes is then created by combining pieces of chromosomes from the old population while favoring old chromosomes with the lowest FOM's. An element of mutation is also included by randomly switching a given number of bits in the chromosomes of the new population. Genetic algorithms have been shown to be effective global optimization methods, and the particular implementation we have used for direct methods has been successfully tailored to find many local minima.

3.3 Solution of the Ge(111)-(4x4)/Ag Surface Structure

Two GIXRD data sets were used in this study and were collected at the Hamburger Synchrotron Radiation laboratory (HASYLAB) by Dr. Robert Feidenhans'l and coworkers. The data was then sent to out lab at Northwestern University in the form of symmetry-averaged intensities along with estimated measurement errors. At Northwestern the data were analyzed using direct methods to determine a basic model

for the surface structure, and then the model was refined according to the procedure described in chapter 2.

3.3.1 Background

For low coverages of Ag on the Ge(111) surface, (4x4) and (3x1) surface reconstructions are formed. Around 1 ML of Ag, a ($\sqrt{3}$x$\sqrt{3}$)R30° structure appears, and at coverages above 1 ML the ($\sqrt{3}$x$\sqrt{3}$)R30° structure transforms into a (6x6) reconstruction (Le Lay 1983). Of these four structures, only the ($\sqrt{3}$x$\sqrt{3}$)R30° is known. As in the case of the Si(111)-($\sqrt{3}$x$\sqrt{3}$)R30°-Ag surface (Ding, Chan, and Ho 1991; Takahashi and Nakatani 1993), the Ge(111)-($\sqrt{3}$x$\sqrt{3}$)R30°-Ag surface has the honeycomb-chained trimer (HCT) structure (Huang et al. 1994; Göthelid et al. 1995; Spence and Tear 1998), where the top layer of Ge-atoms are missing and the remaining Ge-atoms in the outermost double layer form trimers which are surrounded by Ag atoms. The (3x1) reconstruction has only been seen as small insets between (4x4) domains and domains of the native Ge(111)-c(2x8) reconstruction, and it may have the same structure as the Si(111)-(3x1)-Ag surface discussed in section 4.2.

Although the (4x4) structure has been studied by STM and photoelectron spectroscopy, little is known about its atomic geometry. The coverage of Ag has been determined to be around 0.3 ML (Bertucci et al 1979), and high resolution core level photoelectron spectroscopy shows that all Ag atoms sit in nearly the same site (Göthelid et al. 1995). Furthermore, the binding energy of the Ag atoms does not change as the

($\sqrt{3}x\sqrt{3}$)R30° reconstruction is formed, suggesting that the Ag site in the two structures is similar (Göthelid et al. 1995).

STM images show that the unit cell is composed of two triangular subunits with widely varying images depending on the tip bias (Hammar et al. 1993; Le Lay et al. 1994; Weitering and Carpinelli 1997; Spence and Tear 1998). The filled-state images show six protrusions in one of the subunits, and the empty-state images show three protrustions in the other triangular subunit. However, the protrusions seen with STM may represent electronic effects rather than atomic positions, and previous to the application of direct methods, a model was not able to be constructed which could accurately account for measured diffraction intensities.

3.3.2 Experimental Details

Cycles of sputtering and annealing at 650 °C were used to clean Ge(111) samples until LEED measurements showed a sharp native Ge(111)-c(2x8) reconstruction. Silver was then deposited onto the Ge(111) surface from a Knudsen cell while keeping the sample at 400 °C. After LEED, RHEED, and STM all verified the presence of a uniform, well-ordered (4x4) surface reconstruction, the sample was moved into a portable UHV chamber which could be detached from the deposition chamber and mounted onto the X-ray diffractometer.

Two sets of intensities were recorded from two separate samples: one on the wiggler beamline W1 at HASYLAB using an X-ray wavelength of 1.40 Å, and the other

on beamline BW2 at a wavelength of 1.24 Å. Throughout the measurements the angle of incidence was kept fixed at the angle for total external reflection in order to maximize the surface diffraction intensities (Feidenhans'l 1989). The active area on the samples were defined by a 1mm slit in front of the sample and a 1.5 mm slit on the detector arm directly after the sample. A position-sensitive detector with an acceptance angle of 0.6° in the surface plane and 2.8° perpendicular to the surface plane was used to measure the diffracted intensities. Integrated intensities were measured through rocking scans (ω-scans) about the surface normal. The measured intensities were corrected for variations in the active area using a Lorentz factor (Feidenhans'l 1989). For the first data set 107 in-plane, fractional-order reflections were measured and then symmetry-average giving estimates for 64 non-equivalent reflections. For the second data set a total of 112 intensity measurements were recorded and symmetry-average resulting in 71 non-equivalent reflections. The measurement errors were estimated to be about 13% by checking the reproducibility between strong, symmetry-equivalent intensities.

3.3.3 Direct Methods Analysis

STM images from the Ge(111)-(4x4)-Ag surface (Hammar et al. 1993; Le Lay et al. 1994; Weitering and Carpinelli 1997; Spence and Tear 1998) belong to the p3m1 plane group. While slight deviations from p3m1 symmetry could go undetected by STM, the deviations would have to be minor and would not significantly alter the phasing results. The 14 beams forming the basis set for the direct methods analysis are

Table 3.1
Reflections Making up the Basis Set

(h,k)	|F| Set 1	|F| Set 2	Phase (degrees)
(7,7)	1.96	2.15	360
(5,2)	3.23	3.23	180-360
(4,3)	2.82	2.82	30-120
(7,1)	1.29	1.38	45-360
(5,3)	2.11	1.62	45-360
(7,0)	1.94	2.12	45-360
(8,3)	0.89	1.22	45-360
(6,1)	0.81	1.14	45-360
(4,2)	1.51	1.19	45-360
(7,5)	0.84	0.76	45-360
(11,1)	1.59	1.64	45-360
(7,3)	0.72	0.80	45-360
(8,2)	0.85	0.72	45-360
(11,2)	0.69	0.46	45-360

Notes: The measured amplitudes for the second data set have been scaled to the first, and their absolute magnitudes are arbitrary. The phase of (7,7) was fixed at 360° through triplet relationships. The phases of all other reflections were varied within the ranges shown. The limits on (5,2) and (4,3) were used to define an origin and to select an enantiomorph. The phases of (5,2) and (4,3) were varied in steps of 60° and 30° respectively, while all other phases were varied in steps of 45°.

shown in Table 3.1 along with their measured amplitudes and the limits placed on their phases for each of the two data sets. With p3m1 symmetry, beams belonging to the class of reflections (n,n), where n=any integer, have a phase of either 0° or 180°. Also due to the p3m1 symmetry, $\phi(4,3) = -\phi(3,4)$, where $\phi(h,k)$ is used to represent the phase of the (h,k) reflection. Since (7,7) = (4,3) + (3,4) and all three reflections are strong, $\phi(7,7) \sim \phi(4,3) + \phi(3,4) = 0$ (see section 3.1.1). A similar relationship between the (7,7), (5,2), and (2,5) reflections exists which again indicates that $\phi(7,7) \sim 0$, so the (7,7) beam was

assigned a phase of 0°. Origin definition and enantiomorph selection were achieved by restricting the ranges of the phases of the (4,3) and the (5,2) reflections.

The 20 best sets of phases found by the genetic algorithm were used to generate electron density maps. All of the maps showed the same basic structure with only minor variations. Figure 3.3 shows typical maps for each data set. Since the data used in this

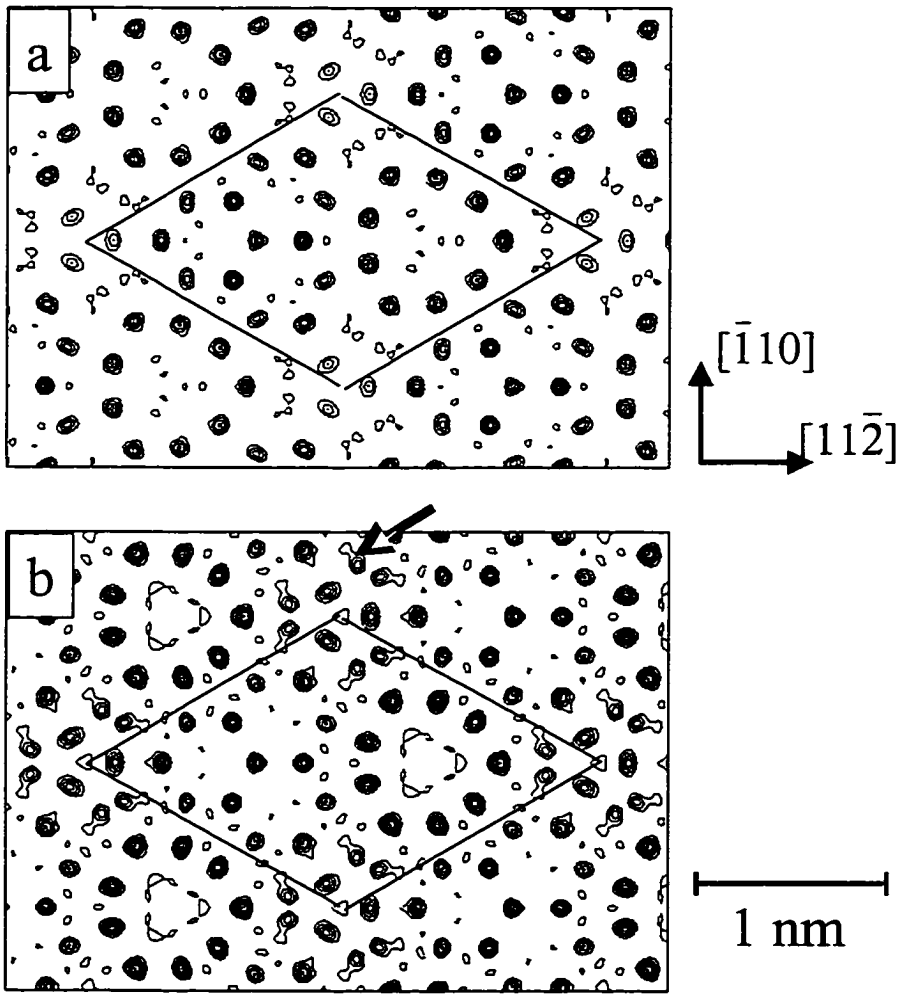

Figure 3.3. Contour map of the calculated electron density using phases estimated through direct methods for a) data set 1 and b) data set 2. For each map 6 contour levels were evenly spaced between zero and the maximum electron density. The arrow in b) indicates a partially occupied Ag site which has a lower occupancy for the first data set.

study were purely two dimensional, the electron density maps are projections of the (4x4) structure onto a plane parallel to the Ge surface as discussed in section 3.2.1. While the relative intensities of the peaks seen in figure 3.3 changed from map to map within the top 20 phasing solutions, the positions of the peaks were always the same. The site arrowed in figure 3.3 was more prominent in maps from the second data set and failed to appear at all in some maps from the first data set. The two possibilities that this site could be either partially occupied or an artifact due to noise in the data were both considered in the subsequent analysis. However, each non-arrowed site in figure 3.3 appeared in all 20 maps and was considered to correspond to either a Ge or a Ag atom site.

3.3.4 Structure Refinement

Allowing for a silver coverage between 1/4 ML and 5/8 ML, models were considered with 4 and 10 sites in each unit cell occupied by Ag atoms and the remaining sites filled with Ge. The agreement between the measured and simulated intensities was quantified using both an R-factor and a χ measure of agreement. While the numbers listed in the tables and used to make the figures are exclusively from the χ refinements, the R-factor is quoted along with the χ value obtained from each model for reference, since the R-factor is a widely used test.

As an initial refinement step atoms were not placed at the site which is arrowed in figure 3.3, and the simulated intensities were compared only with the first data set for

which the arrowed site was not prominent. Assuming that all of the phasing analysis sites represent atoms in the top surface layer, a complete double layer of Ge atoms was also added to each model to simulate relaxations extending into the bulk. Accordingly, the three possible registries between the surface layer and the relaxed bulk double layer were investigated for each different distribution of Ge and Ag atoms among the surface sites. All refinements of the atom positions were done within the p3m1 plane group. Two Debye-Waller factors were included in the refinement, one for the surface Ge and one for the Ag. The Debye-Waller factor for the relaxed double layer was set at the value for bulk Ge. Under these conditions, the best fit to the measured intensities was obtained with the model shown in figure 3.4 which yielded χ=2.31 and R=0.21. Counting a scaling term, 21 variables were used in this fit for the 71 measured reflections in data set 1.

It should be noted that other permutations of Ag and Ge among the phasing analysis sites cannot be conclusively ruled out. For example, a model with Ag placed at the six nearest surface sites surrounding the trimers at the corners of the (4x4) unit cell in figure 3.4 refines to a χ value of 2.91 and an R-factor of 0.23. Other rearrangements of Ag and Ge also lead to models with only a slightly worse diffraction intensity fit than that for the distribution of Ag shown in figure 3.4. However, the model in figure 3.4 is consistent with all of the experimental data available on submonolayer coverages of Ag on Ge(111) as will be expanded upon in section 3.3.5.

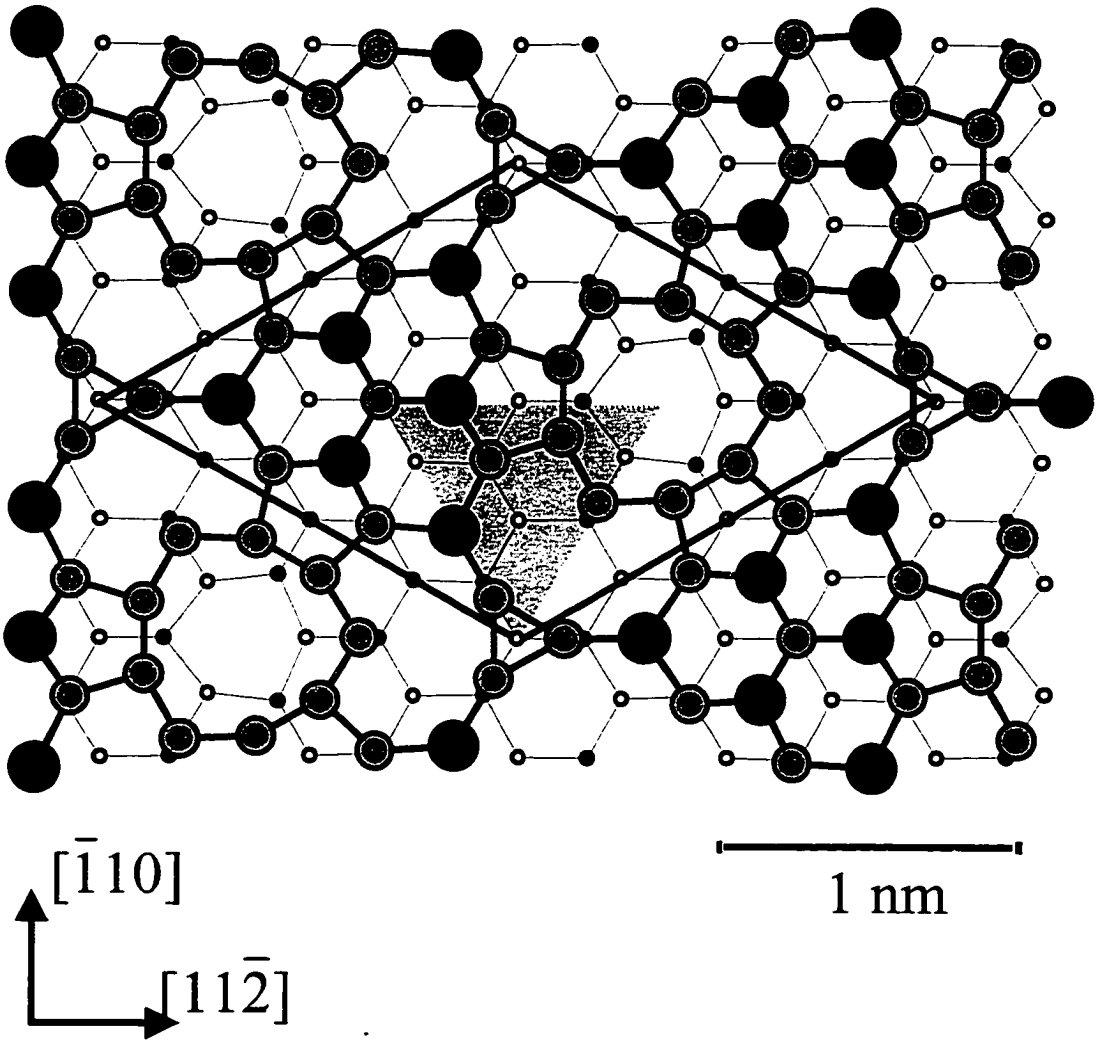

Figure 3.4. Proposed model for the Ge(111)-(4x4)-Ag surface. Large black circles represent Ag, and everything else is Ge. The (4x4) unit cell (a=b=16.002Å, γ=120°) is outlined, and the asymmetric unit for the plane group p3m1 is shaded in gray.

The model shown in figure 3.4 was also refined using the measured intensities from the second data set. While the atom positions did not significantly change (the largest shift was 0.017 nm), the fit was not as good for the second data set with χ=3.26 and R=0.29. To look for additional atom sites, a Fourier difference map was created and

is shown in figure 3.5. A strong peak in the difference map is seen at the location corresponding to the arrowed site in figure 3.3. This suggests that the arrowed site is not an artifact and is likely due to a partially occupied Ag site which has a higher occupancy for the second data set. The other strong peak seen in figure 3.5 is located slightly displaced from a site already occupied by Ge. The possibility that this site was Ag instead of Ge was investigated, but a better fit to the intensities was not obtained.

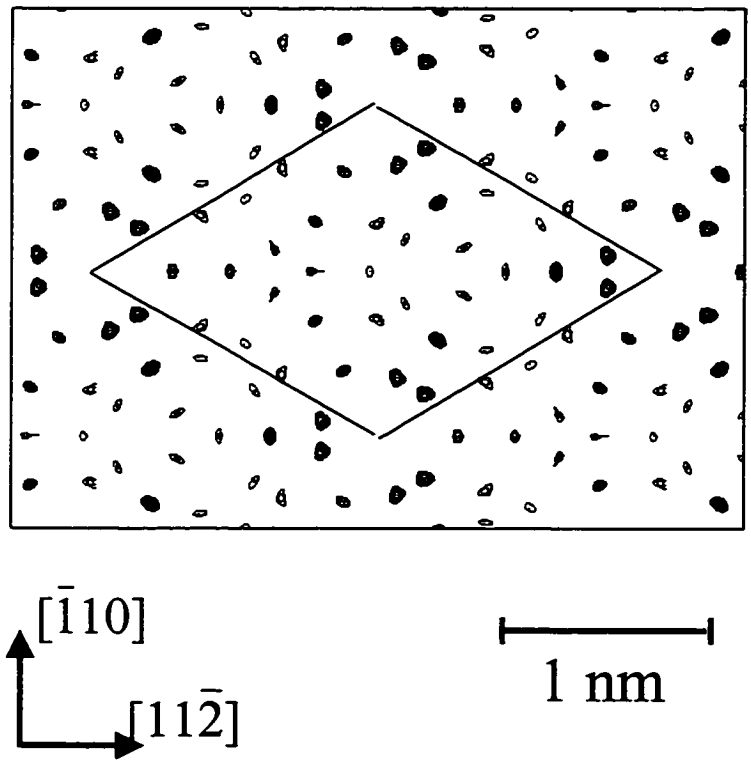

Figure 3.5. Fourier difference map calculated for the second data set using the model shown in Fig. 3.4. Six contour levels were evenly spaced between half the maximum and the maximum electron density to highlight the strongest peaks.

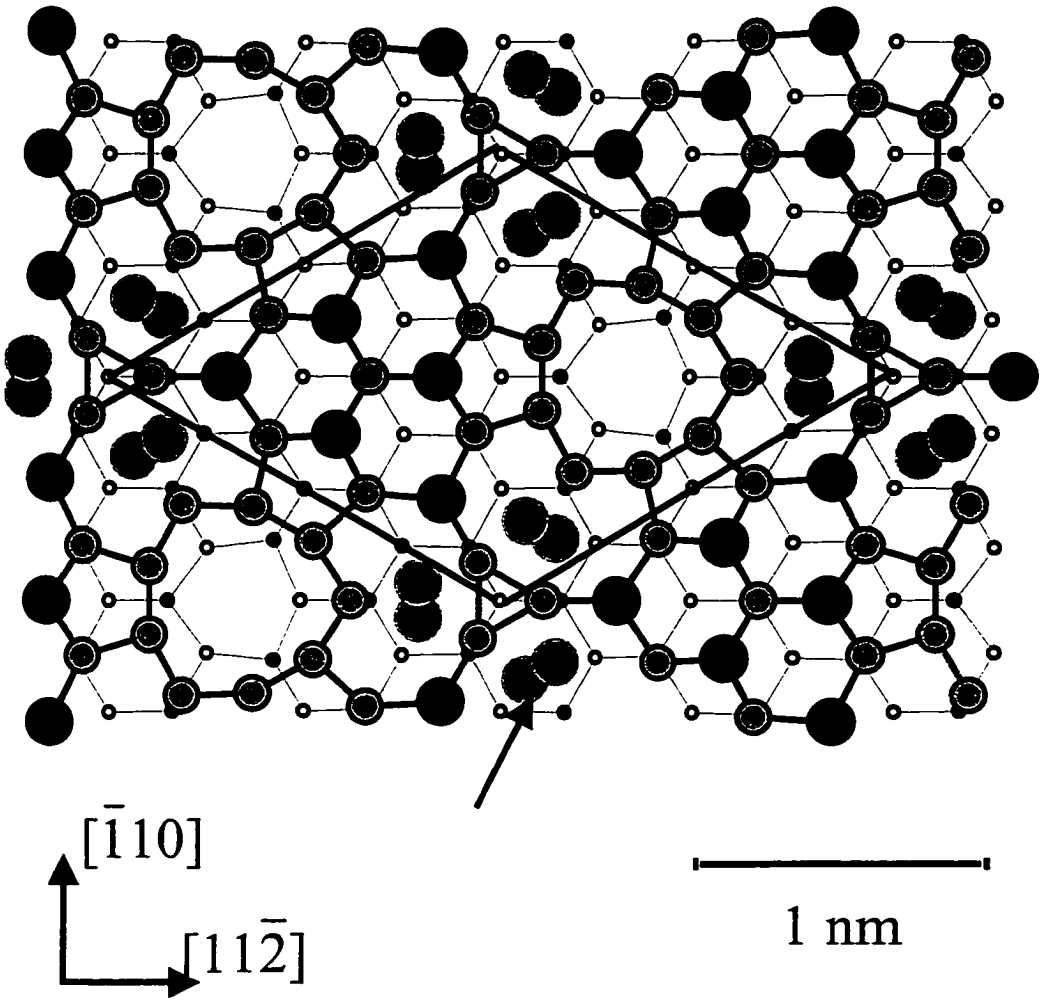

Figure 3.6. The proposed (4x4) model structure with a partially occupied Ag site shown by large dark-gray circles (arrowed). The occupancy of this site was refined to 0.27 and 0.36 for data sets 1 and 2 respectively.

Working with the hypothesis that the Ge(111)-(4x4)-Ag structure can accommodate a variable range of Ag through a partially occupied site, we refined a new model with the second data set (fig. 3.6). The new model contained four new variables: an x and a y position for the new partially occupied Ag site, a variable for the occupancy of the site, and a Debye-Waller factor for the site. A better fit was obtained with χ=2.63

and R=0.13 at an occupancy of 0.3 for the new Ag site. Using the new model for the first data set yielded χ=2.15 and R=0.14 with an occupancy of 0.2 for the Ag site. Finally, both data sets were fit together with a single set of values for all of the atomic positions and Debye-Waller factors. A separate occupancy for the partial Ag site was refined for each data set. In the final fit, the occupancies refined to 0.27 and 0.36 for the first and second data sets respectively yielding χ=2.22 and R=0.18. The atomic positions and Debye-Waller factors for this fit are shown in table 3.2. With a separate scaling factor for each data set, 28 parameters were varied, and including both data sets gave a total of 137 measurements. Fourier difference maps created from this final model for both data sets were essentially featureless with no well-resolved peaks.

3.3.5 Discussion of Results

Weitering and Carpinelli (1997) have already noted strong indications that the (4x4) and the ($\sqrt{3}$x$\sqrt{3}$)R30° reconstructions induced by Ag on Ge(111) are related. The structure for the Ge(111)-($\sqrt{3}$x$\sqrt{3}$)R30°-Ag surface, the honeycomb-chained-trimer structure (Huang, Over, and Tong 1994; Göthelid et al. 1995; Spence and Tear 1998), is illustrated in figure 3.7. It consists of an array of Ge trimers, with each trimer surrounded by six Ag atoms. Consequently, Weitering and Carpinelli suggested that the Ge trimer serves as a common building block for the (4x4) structure as well. The proposed model supports this view. The Ge trimer with the three nearest neighboring Ag atoms found at the corners of the unit cell in figure 3.4 matches the basic structural

Table 3.2
Atomic Positions for the Ge(111)-(4x4)/Ag Structure

Atom	x	x(unrelaxed)	y	y(unrelaxed)	Wyckoff	z
Ag	0.4197	-	0.5803	-	d	Surface
Ag	0.1511	-	0.3021	-	d	Surface
Ag	0.2099	-	0.1444	-	e	Surface
Ge	0.0563	-	0.1125	-	d	Surface
Ge	0.3826	-	0.1913	-	d	Surface
Ge	0.4774	-	0.3706	-	e	Surface
Ge	0.3436	-	0.4102	-	e	Surface
Ge	0.3333	-	0.6667	-	b	Surface
Ge	0.3349	0.3333	0.1674	0.1667	d	Layer 1
Ge	0.5772	0.5833	0.4228	0.4167	d	Layer 1
Ge	0.0793	0.0833	0.1586	0.1667	d	Layer 1
Ge	0.3272	0.3333	0.4074	0.4167	e	Layer 1
Ge	0.3333	0.3333	0.6667	0.6667	b	Layer 1
Ge	0.2475	0.2500	0.4951	0.5000	d	Layer 2
Ge	0.5102	0.5000	0.2551	0.2500	d	Layer 2
Ge	0.5012	0.5000	0.4988	0.5000	d	Layer 2
Ge	0.2512	0.2500	0.2474	0.2500	e	Layer 2
Ge	0.0000	0.0000	0.0000	0.0000	a	Layer 2

Notes: Atom positions are in terms of a (4x4) unit cell in the p3m1 plane group: a=b=16.002Å, γ=120°. The Wyckoff letter corresponds to the site symmetry. A Wyckoff letter of "d" indicates a site on a mirror plane and therefore the x and y positions are symmetry related and only one variable is used to describe the atom position. "e" is a general site and so both the x and the y values are independently refined variables. "a" and "b" are fixed sites lying on a three-fold axis and are not refined. The occupancy of the partial Ag site was fit with 0.27 for data set 1 and 0.36 for data set 2. Isotropic Debye-Waller factors (defined as $B=8\pi^2\langle u^2\rangle$, where $\langle u^2\rangle$ is the mean square atomic displacement) were fit at 6.60 $Å^2$ for fully occupied Ag, 3.14 $Å^2$ for partially occupied Ag, 3.74 $Å^2$ for Ge in the surface layer, and 0.84 $Å^2$ for Ge in layers 1 and 2. [In pure bulk samples at 280K, B=0.70 $Å^2$ for Ag and B=0.57 $Å^2$ for Ge (Peng et al. 1996).]

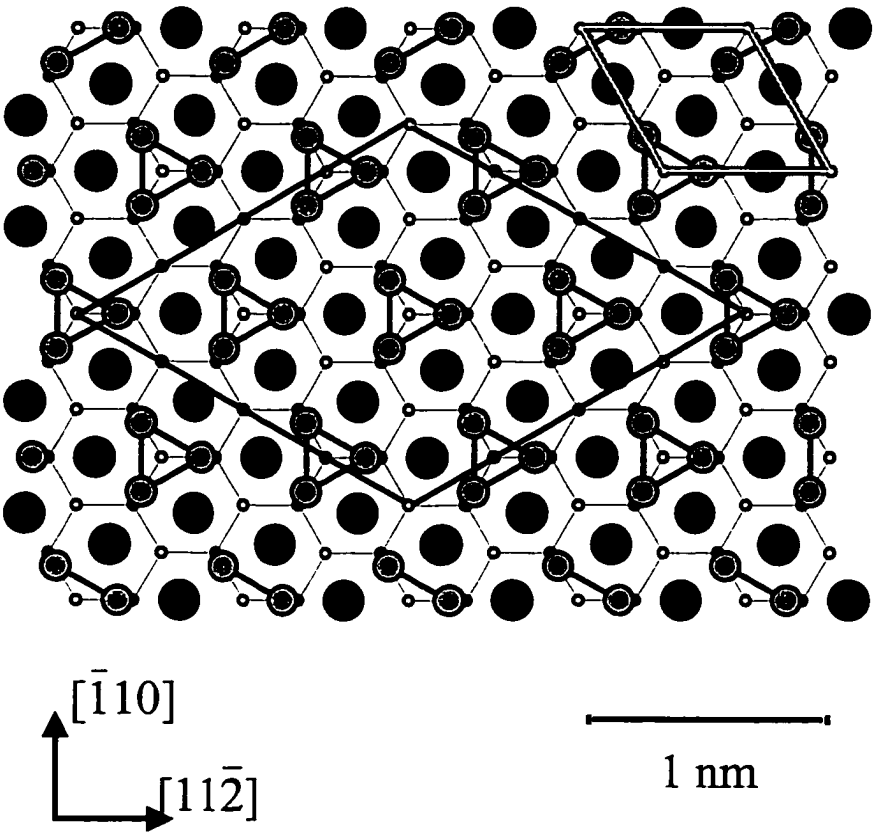

Figure 3.7. Honeycomb-chained-trimer model for the Ge(111)-($\sqrt{3}$x$\sqrt{3}$)R30°-Ag surface. Large black circles represent Ag, and everything else is Ge. A (4x4) unit cell has been outlined in black to facilitate comparisons with figs. 3.4 and 3.6. The ($\sqrt{3}$x$\sqrt{3}$) R30° unit cell is outlined in gray and white in the top right corner.

unit of the ($\sqrt{3}$x$\sqrt{3}$)R30° surface. The model is also in agreement with the high resolution core level photoelectron spectroscopy results which suggest that all of the Ag atoms are in nearly identical sites, in both the (4x4) and the ($\sqrt{3}$x$\sqrt{3}$)R30° structures (Göthelid et al. 1995). The Ag coverage for the proposed (4x4) model is 3/8 ML while the coverage for the ($\sqrt{3}$x$\sqrt{3}$)R30° surface is 1 ML. The comparison of figure 3.4 with figure 3.7 reveals an easy path of transformation from the (4x4) structure to the

($\sqrt{3}$x$\sqrt{3}$)R30° surface upon the addition of 5/8 ML of Ag (or 10 Ag atoms per (4x4) unit cell). All that is required in each unit cell is the removal of 3 Ge atoms and the addition of the 10 Ag atoms. The six Ag atoms already in the (4x4) unit cell only need to be slightly displaced, and apart from the removal of the 3 Ge atoms, the bonds between the surface layer Ge and the first bulk double layer remain intact.

The partially occupied Ag site included in the final model suggests that the two data sets were collected from a (4x4) surface already in the process of transformation to the ($\sqrt{3}$x$\sqrt{3}$)R30° structure with the second data set taken from a slightly more Ag-rich sample. The position of the partially occupied site is shown in figure 3.6. The six positions per unit cell for this site can be grouped into three pairs. The two positions in a pair are too close to both be occupied at the same time so the maximum possible occupancy is 0.5. An occupancy of 0.5 would correspond to a disordered arrangement of Ag atoms randomly distributed among the positions under the constraint of exactly one Ag atom allowed in each pair. Having only one of the two positions in each pair occupied will break the mirror symmetry locally and induce disorder in the basic (4x4) structure.

The random site occupancy disorder described above would give rise to a diffuse background in diffraction experiments. Transmission electron diffraction data from surfaces with regions of (4x4) mixed with regions of ($\sqrt{3}$x$\sqrt{3}$)R30° indicate an additional type of disorder giving rise to structured diffuse scattering. Figure 3.8 shows two diffraction patterns: the first from a region that is predominantly covered by the (4x4)

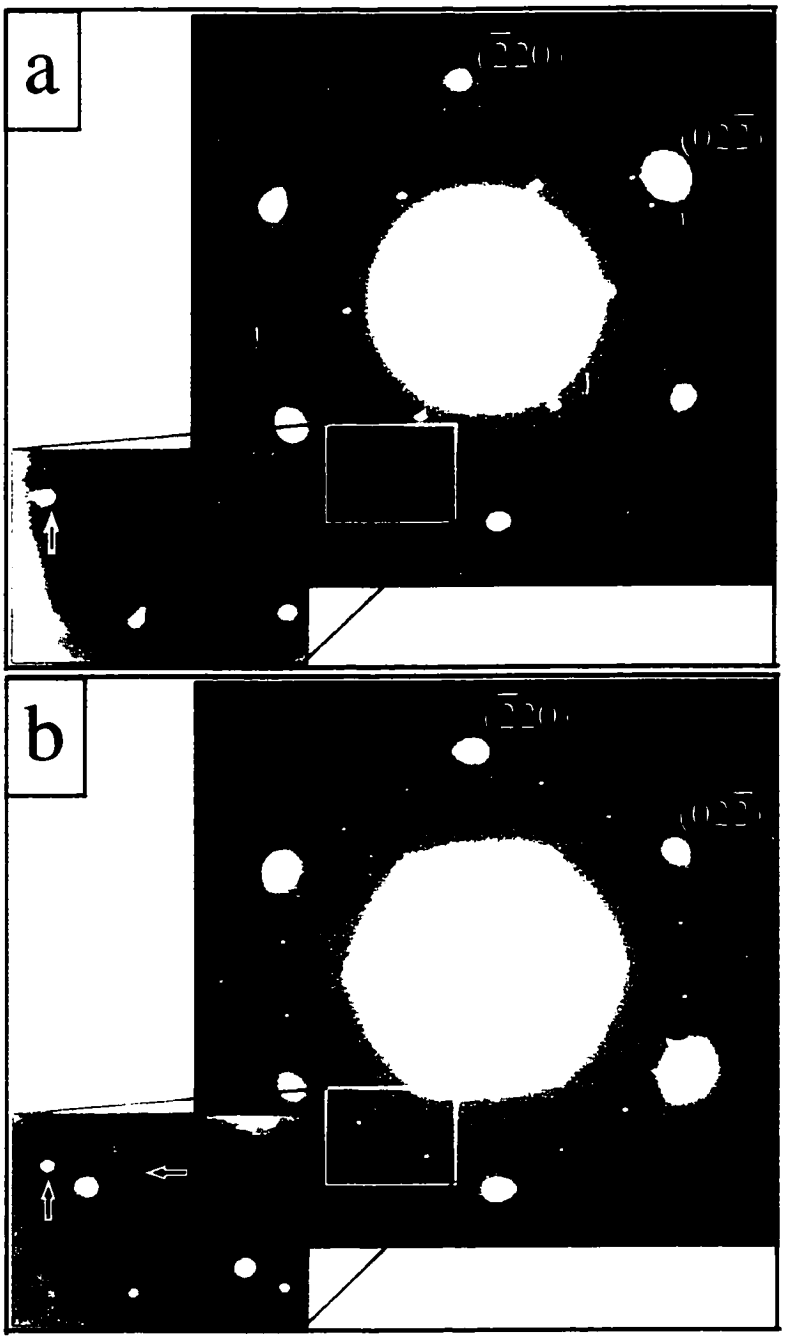

Figure 3.8. Transmission electron diffraction patterns taken close to Ge(111) zone-axis. a) From a region covered by the (4x4) structure. b) From a region with both (4x4) and ($\sqrt{3}$x$\sqrt{3}$)R30° domains. The magnified region in (b) shows diffuse rings (horizontal arrow) surrounding the most intense ($\sqrt{3}$x$\sqrt{3}$)R30° spots. The diffuse rings are not present in (a). The vertical arrows point to the same (4x4) surface reflection in both (a) and (b). [Both TED patterns are courtesy of Mr. Daniel Grozea].

structure and the second from a region in which the (4x4) and ($\sqrt{3}$x$\sqrt{3}$)R30° structures coexist. In the second diffraction pattern, diffuse rings surround the strongest ($\sqrt{3}$x$\sqrt{3}$) R30° spots. These rings are remarkably similar to the diffuse scattering reported on the Au/Si(111) surface during the transformation between the Si(111)-($\sqrt{3}$x$\sqrt{3}$)R30°-Au and the Si(111)-(6x6)-Au structures (Higashiyama, Kono, and Sagawa 1986; Nogami, Baski, and Quate 1990; Takahashi, Tanishiro, and Takayanagi 1991; Yuhara, Inoue, and Morita 1992; Takami et al. 1994; Falta et al. 1995). In the Au/Si(111) case, the rings can be attributed to a rotationally disordered yet evenly-spaced array of domain walls separating regions of local ($\sqrt{3}$x$\sqrt{3}$)R30° order. In the case of Ag/Ge(111), the situation may be similar with evenly-spaced boundaries forming between the ($\sqrt{3}$x$\sqrt{3}$)R30° and the (4x4) domains.

CHAPTER 4: LINEAR RECONSTRUCTIONS ON THE SI(111) SURFACE

When coupled with transmission electron diffraction (chapter 2) the direct methods approach discussed in chapter 3 provides a powerful technique for solving and refining surface structures. The utility of this methodology is shown by the work discussed in this chapter. Two previously unknown surface reconstructions on the Si(111) surface were solved and refined by applying direct methods to TED data. Both of these reconstructions, the Si(111)-(3x1)/Ag and the Si(111)-(4x1)/In, can be classified as "linear" reconstructions as explained in section 4.1. The solution of the Si(111)-(3x1)/Ag surface is detailed in section 4.2, and the Si(111)-(4x1)/In surface is discussed in section 4.3. Finally, section 4.4 offers conclusions about the general characteristics of linear reconstructions on the Si(111) surface.

4.1 Definition of Linear Reconstructions

Figure 4.1 shows the unreconstructed (111) surface of a diamond cubic crystal (e.g. silicon or germanium). Among the symmetry elements present is a three-fold rotation axis perpendicular to the surface, and as one might suspect many two-dimensional structures forming on this surface display a three-fold axis as well. The Ge(111)-(4x4)/Ag structure discussed in chapter 3 is one such example. However, there

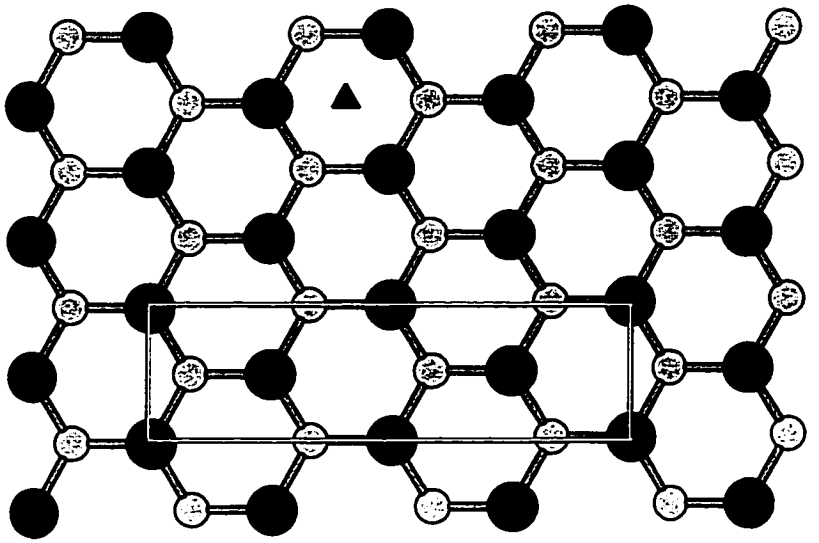

Figure 4.1. The unreconstructed (111) surface of a diamond cubic crystal. The surface has a double-layer structure with the darker atoms sitting slightly higher than the lighter atoms. Along the [111] direction the crystal has three-fold rotational symmetry, and one three-fold axis is indicated by the black triangle at the top. Linear reconstructions on this surface have either two-fold or only one-fold rotational symmetry. A possible rectangular unit cell for such a reconstruction is shown at the bottom.

is another general class of structures which form on the (111) surface which can be called "linear" reconstructions. Rather than sharing the full symmetry of the substrate, these structures have a rectangular unit cell with a two-fold rotation axis. While the structures of many linear reconstructions remain unknown, the ones that have been solved consist of chains or rows of atoms which appear as continuous lines or rows of peaks in STM images.

The most familiar and thoroughly understood linear reconstruction is the native Si(111)-(2x1) structure (Zitzlsperger et al. 1997) (fig. 4.2a). It forms upon cleaving in a

UHV environment and is metastable. Heating the Si(111)-(2x1) surface above ~330 °C (Monch 1995, 223) irreversibly leads to the formation of the Si(111)-(7x7) native reconstruction. A key element of the (2x1) structure is the presence of silicon dimer chains which are highlighted as lighter-shaded atoms in figure 4.2a. Recently it has been recognized by several researchers that similar dimer chains may be a part of other linear reconstructions on the Si(111) surface. Most notably, all models currently proposed for the (3x1) structure, which is induced by many different metals on Si(111), contain at least one dimer chain. The importance of the work described in this chapter is to show that similarities between different linear reconstructions on the Si(111) surface are more widespread and more general in nature than previously thought. The Si(111)-(3x1)/Ag structure described in section 4.2 (Collazo-Davila, Grozea, and Marks 1998), the Si(111)-(4x1)/In structure described in section 4.3 (Collazo-Davila et al. 1997), and the Si(111)-(5x2)/Au structure (Marks and Plass 1995) can all be described in the same general terms. A partial silicon double layer containing a silicon dimer chain and either one or two missing rows leaves a trench parallel to [$\bar{1}$10] in which the metal adsorbate atoms lie. Discovering such a general trend may aide in the solution of linear surface structures which remain unknown like Si(111)-(5x1)/Ba (Weitering 1996) and Si(111)-(6x1)/Cs (Park et al. 1995).

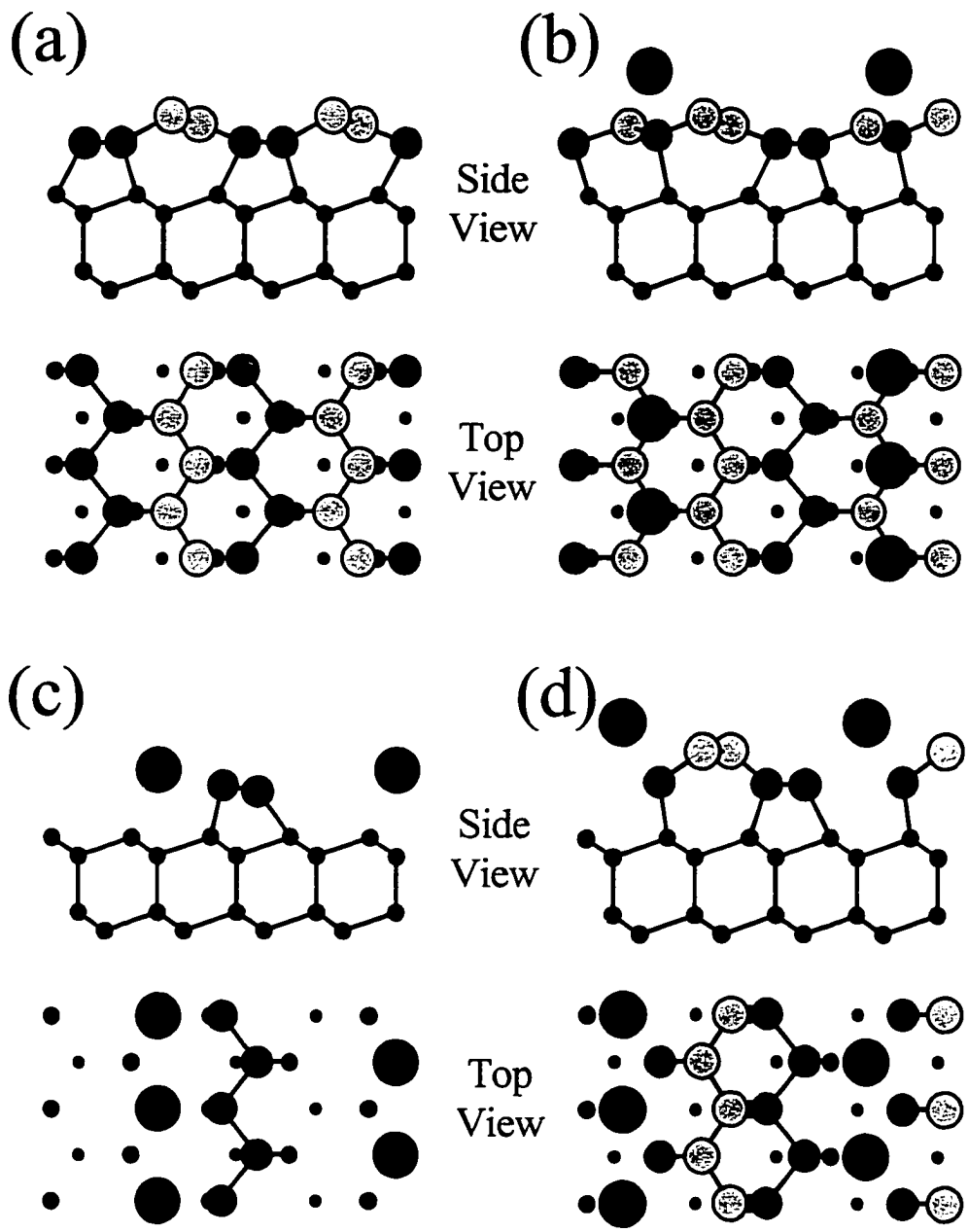

Fig. 4.2 Three models proposed for the metal-induced Si(111)-(3x1) reconstruction shown along with the native Si(111)-(2x1) surface. The metal adsorbate atoms are represented by the large, black atoms. Surface dimer chains are highlighted as two different shades of gray. a) Native (2x1) reconstruction on Si(111) surface. b) Extended Pandey chain model for Si(111)-(3x1) reconstruction. c) Seiwatz chain model for (3x1). d) Missing-row Pandey chain model for (3x1).

4.2 Si(111)-(3x1)/Ag Reconstruction

Much research has focused on submonolayer coverages of alkali metals on the Si(111) surface due to their unique effects on Si oxidation. When deposited at room temperature the alkali metals promote oxidation and could be useful in a low temperature microchip processing step to form gate oxides without loosing sharp doping profiles (Muscat, Rjeb, and Roy 1994). When deposited at elevated temperatures, they form the (3x1) surface structure which inhibits oxidation (Tikhov, Surnev, and Kiskinova 1991). The mechanisms giving rise to such widely differing behaviors are not completely understood, in part due to the fact that the (3x1) structure was previously unknown.

The TED data used for this investigation were collected in the SPEAR system described in section 1.2.1. Mr. Daniel Grozea was responsible for the Si(111) sample preparation and the formation of the (3x1) surface structure. Both myself and Mr. Grozea recorded and analyzed the diffraction data.

4.2.1 Background

LEED I-V curves suggest that the same Si(111)-(3x1) structure is induced by Li, Na, Mg, and Ag independent of adsorbate type (Fan and Ignatiev 1990; Quinn and Jona 1991). While the adsorbate coverage was initially debated, careful measurements based on ion scattering spectrometry (ISS) (Hashizume et al. 1993) and on AES combined with

STM (Fukuda 1994) have shown that the saturation coverage is 1 adsorbate atom per 3x1 unit cell. Similarities between STM images of Li/(3x1) and Ag/(3x1) (Wan, Lin, and Nogami 1992) along with the similar Si *2p* core level spectra obtained from Na/(3x1) (Okuda et al. 1994; Paggel et al. 1995), Mg/(3x1) (An et al. 1995), and Li/(3x1) (Weitering, Shi, and Erwin 1996) have reinforced the idea that one structure, predominately made up of Si atoms, is formed by many different elements on the Si(111) surface.

Several groups have noted that the (3x1) surface electronic properties resemble those of the native Si(111)-(2x1) structure. Figure 4.2 shows three models proposed by Okuda et al. for the 3x1 surface (Okuda et al. 1994) along with the 2x1 structure (Zitzlsperger et al. 1997). All three models contain silicon dimer chains. The model shown in figure 4.2b was independently proposed by Erwin (1995) who has referred to it as an extended Pandey chain (Pandey 1981). The structure in figure 4.2c can be described as a Seiwatz chain (Seiwatz 1964) with a neighboring row of adsorbate atoms sitting in T_4 sites. Sakamoto et al. (1994), Weitering et al. (1994), and Wong et al. (1994) each proposed a variant of the Seiwatz model with the adsorbate atoms moved to T_1 sites halfway in-between the silicon chains. The model in figure 4.2d has received relatively little attention since being proposed. Even though total energy calculations showed that either the extended Pandey (Erwin 1995) or the Seiwatz (Jeong and Kang 1996) structure has the lowest surface energy for the previously proposed models,

neither structure can fully account for experimental angle-resolved photoemission data (Weitering, Shi, and Erwin 1996; Okuda et al. 1997).

4.2.2 Experimental Details

For the TED study a 3 mm silicon disc was prepared as described in section 1.2.2. Cycles of ion milling (1kV Ar^+) and annealing at 750 °C were used to clean the surface until a sharp Si(111)-(7x7) diffraction pattern was seen in the microscope. After room temperature deposition of Ag and an anneal at 550 °C for several seconds, both the (3x1) and the ($\sqrt{3}$x$\sqrt{3}$) diffraction patterns could be detected. The Si(111)-($\sqrt{3}$x$\sqrt{3}$)/Ag reconstruction is a well-known structure induced at higher Ag coverages. Diffraction intensities were recorded as described in section 2.2. Two separate data sets from different regions of the sample and at different values of crystal tilt were collected and reduced to give a total of 90 different (3x1) surface beam measurements. Of the 90 measured intensities, 56 had errors between 4% and 30%, 26 had errors between 30% and 55%, and 8 had errors between 55% and 90%.

4.2.3 Structure Determination Through Direct Phasing

STM images of the 3x1 structure belong to the p1 plane group, although the deviations from cm symmetry appear to be minor. For completeness the TED data was analyzed by direct phasing in both p1 and cm plane groups. Taking the most probable sets of phases found in the phasing analysis and combining them with the measured

intensities, the diffraction pattern was Fourier transformed back into a scattering potential. The solutions found by the direct phasing analysis all showed slight variations of one basic scattering potential which is shown in figure 4.3. Four well-resolved peaks labeled A, B, C, and D can be seen along with one double-lobed area labeled E.

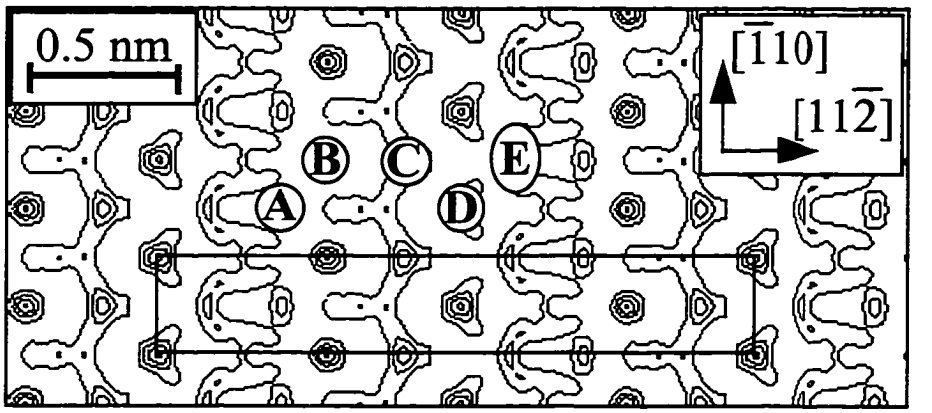

Figure 4.3. Contour map of the scattering potential for the Si(111)-(3x1)/Ag surface reconstructed using direct methods. A centered (6x1) unit cell is outlined. Four well-resolved independent sites within the unit cell have been labeled A, B, C, and D. A weak, double-lobed feature has been labeled E.

The four well-resolved peak positions were taken as initial atom sites from which to start simulating the measured diffraction intensities. The double-lobed region was considered to represent either two partially-occupied atom sites or an artifact arising from the lack of a complete data set in reciprocal space. As an initial diffraction intensity fitting step, both interpretations for the double-lobed area were tried along with the permutations of placing one Ag atom at one of the sites and Si atoms at the remaining sites. Only one layer of atoms was modeled kinematically, and the effects of

the bulk crystal and dynamical diffraction were neglected. The best fit found under these conditions gave a reduced χ^2 value of 4.49 for the case of Si atoms at positions A, B, C, and D and two half-occupied Ag sites at position E. The next best fit for another permutation of Ag and Si atoms among the A-E sites was much worse with χ^2=8.46.

The atom positions found through the phasing analysis and the initial refinement step suggest a new model (fig. 4.4) for the Ag/Si(111)-(3x1) surface. In this new model a partial silicon double layer with a silicon chain has a missing row where the adsorbate atoms lie. The Ag atoms bond to a single atom in the silicon chain on one side of the trench and can bond to one of two atoms in the partial double layer on the other side. In this way, by choosing either the partial double layer atom in the $[\bar{1}10]$ direction or the one in the opposite direction, the Ag atom breaks the mirror symmetry along $[11\bar{2}]$. Both possible Ag sites are shown in figure 4.4. All of the Ag atoms in a single row would have to shift in the same direction to accommodate all the dangling bonds, but one can postulate the propagation of a surface dislocation traveling the length of a trench thereby shifting every Ag atom in that row. Such a picture explains the deviation from cm symmetry towards p1 symmetry seen in STM images (Wan, Lin, Nogami 1992; Ohnishi et al. 1994; Carpinelli and Weitering 1995) as well as the tip-induced shifting of entire rows between scans (Carpinelli and Weitering 1995). The model in figure 4.4 can also account for data linking the Ag/Si(111)-(3x1) and the Ag/Si(111)-($\sqrt{3}$x$\sqrt{3}$) structures. The fact that the ($\sqrt{3}$x$\sqrt{3}$) structure can be formed at room temperature by deposition of Ag on a preexisting (3x1) surface reveals a low activation energy

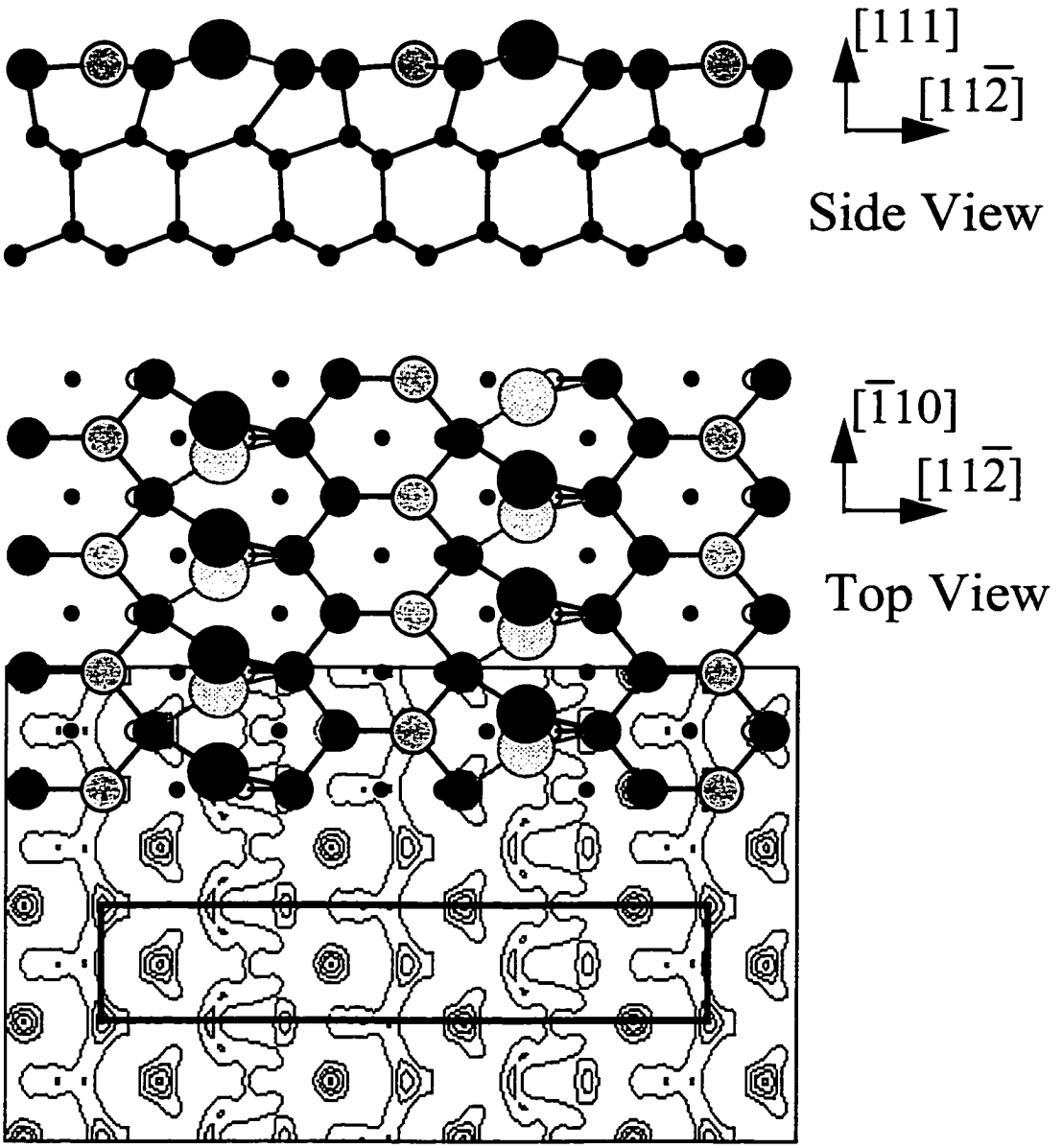

Figure 4.4. Structure of the Si(111)-(3x1)/Ag surface derived from direct methods. A contour map of the scattering potential calculated from the measured intensities and the estimated phases is shown at the bottom. The atomic positions used to construct the ball-and-stick models are the refined positions listed in table 4.1. The refined atom sites agree very well with the locations indicated by the contour map. As in figure 4.3 a centered 6x1 unit cell is outlined.

barrier (Carpinelli and Weitering 1996). This coupled with the observation of similar Ag MNN Auger line shapes for (3x1) and ($\sqrt{3}$x$\sqrt{3}$) (Fukuda 1994) points to a similar local bonding geometry for Ag in both structures. Each Ag atom in figure 4.4 bonds most strongly to a single Si atom in the Si chain and has two other Si atoms surrounding it. Similarly, in ($\sqrt{3}$x$\sqrt{3}$) an Ag atom bonds most strongly to a single Si atom in a Si trimer and has two other Si neighbors on the surface.

4.2.4 Structure Refinement

For the final fitting procedure the bulk crystal and dynamical effects were accurately modeled. Both the angle of crystal tilt and the thickness of the sample were found by measuring the bulk diffraction intensities and fitting them with the sample thickness and tilt as the only two variables in a multislice calculation (section 2.3.2). The best fit values for the thickness of the two sample areas (45 nm and 48 nm) agreed with the thickness estimated from PEELS data (Malis, Cheng, and Egerton 1988) within the PEELS measurement error. With the values for the bulk parameters, two reconstructed double layers were added to the surface, and again multislice calculations were used to find the (3x1) surface beam intensities. Allowing one bulk double layer to relax with the new model for the surface atoms gave χ^2=2.81. The fit included 14 parameters: 12 for atom sites and a Debye-Waller factor for both the Ag and the surface Si. The Ag occupancy was set at 0.5 for the two equivalent Ag positions to model a disordered arrangement of the [$\bar{1}$10] shifts on the surface. It should be noted that the

disorder is not inconsistent with the STM images. While Ag atoms in a single row parallel to $[\bar{1}10]$ are well ordered and predominately shift in the same direction, the correlation between neighboring Ag rows is weak and the disorder along the $[11\bar{2}]$ direction is high.

For comparison, diffraction intensities from the other currently proposed structures for the (3x1) surface were simulated. Several variations on each model were explored including different registries between the substrate and the surface atoms and possible displacements of Si surface atoms in the $[\bar{1}10]$ direction. One relaxed double layer and 2 or 3 Debye-Waller factors were always included keeping the number of fitting parameters between 12 and 16. The best fit obtained with an extended Pandey chain model was χ^2=7.54. Seiwatz models were tried with Ag at T_1 and T_4 sites resulting in a best χ^2 of 6.35. The type of model shown in figure 4.2d yielded a χ^2=4.33. Only the new model obtained from direct phasing was able to give a reasonable fit to the measured intensities.

Allowing two bulk double layers to relax with the new model lowers the χ^2 value to 1.62. The 18 atomic sites varied in this fit are shown in table 4.1 along with 3 Debye-Waller factors and a refined occupancy for the Ag sites. Estimated errors were calculated within a 68% confidence limit taking into account correlations between all variables. For the relaxed subsurface layers, in which the atoms are only slightly displaced from their bulk positions, the relative atomic positions within the layer were determined more precisely than the position of the layer as a whole with respect to the

Table 4.1
Refined Atomic Positions for Si(111)-(3x1)/Ag

Atom	x	x [unrelaxed]	y	z [inferred]	σ [layer]	<σ rel>
Ag	0.132	-	0.350	Surface	0.0015	0.0015
Si	0.449	-	0.000	Layer		
Si	0.028	-	0.000			
Si	0.327	-	0.000			
Si	0.252	-	0.500			
Si	0.000	0.000	0.500	Layer 1	0.0020	0.0012
	0.172	0.167	0.000			
	0.344	0.333	0.500			
Si	0.068	0.056	0.500	Layer 2	0.0040	0.0014
	0.229	0.222	0.000			
	0.397	0.389	0.500			
Si	0.068	0.056	0.500	Layer 3	0.0084	0.0014
	0.235	0.222	0.000			
	0.401	0.389	0.500			
Si	0.139	0.111	0.000	Layer 4	0.0023	0.0009
	0.309	0.278	0.500			
	0.470	0.444	0.000			

Notes: Atomic positions are in terms of a c(6x1) unit cell in the cm plane group: a=19.953 Å, b=3.840 Å. All y positions were fixed except for the Ag site, $\sigma_y = \pm 0.0029$. The silver occupancy was fit with 0.43 ±0.04, and isotropic Debye-Waller factors (defined as $B=8\pi^2\langle u^2\rangle$, where $\langle u^2\rangle$ is the mean square atomic displacement) were fit at 6.32 ±1.5 Å^2 for Ag, 3.20 ±0.46 Å^2 for surface Si, and 0.47 ±0.22 Å^2 for layers 1 and 2 Si. In pure bulk samples at 280K, B=0.70 Å^2 for Ag and B=0.46 Å^2 for Si (Peng et al. 1996). For the errors σ [layer] and <σ rel> see text.

bulk crystal. This is a consequence of the fact that the data set includes no bulk reflections and consists entirely of surface superstructure intensities. Accordingly, two errors are listed for each layer in table 4.1. The first, σ[layer], represents the 68% confidence limit with respect to shifting the entire layer as a whole relative to the bulk.

The second, $<\sigma_{rel}>$, is an average value for the uncertainties in the relative atomic positions within the layer. Individual values of σ_{rel} for pairs of atoms were all found to lie within 50% of $<\sigma_{rel}>$ for a given layer. The possibility of Si atoms shifting in the $[\bar{1}10]$ direction was also explored, however displacements of Si atoms along $[\bar{1}10]$ were not significant and did not improve the fit.

4.2.5 Discussion of Results

The value 0.43 ± 0.04 which was fit for the Ag occupancy suggests a slightly lower coverage than 1/3 of a monolayer and is consistent with previous estimations of the adsorbate coverage on (3x1) surfaces. Weitering et al. (1994) have suggested that different surface preparation conditions may lead to different levels of adsorbate vacancy defects thus explaining the range of coverages reported in the literature. While the current observation is consistent with this view, it is not conclusive as the error on the occupancy increases to ± 0.12 at the 99% confidence limit. It is interesting to note possible differences between the Ag-induced (3x1) structure and alkali-induced (3x1). Surface X-ray data from Li/(3x1) and Na/(3x1) have been fit by a similar model (Lottermoser et al. 1998) to the one proposed here for Ag/(3x1). The X-ray model for the alkali metals is more symmetric than the Ag/(3x1) model with no deviations from cm symmetry. This agrees well with STM images which show cm symmetric images for the alkali (3x1) surfaces (Hashizume et al. 1993; Wan, Lin, and Nogami 1992) and p1 symmetric images for Ag/(3x1) (Wan, Lin, and Nogami 1992; Ohnishi et al. 1994;

Carpinelli and Weitering 1995). The difference may be due to atomic size and number of valence electrons. Ag may readily form two bonds long enough to bridge the trench parallel to $[\bar{1}10]$ thus breaking the cm symmetry, while the monovalent alkali metals might only form one bond on one side of the trench and thereby preserve the mirror along the $[1\bar{1}2]$ direction.

4.3 Si(111)-(4x1)/In Reconstruction

The Si(111)-(4x1)/In surface is an interesting subject of study for a couple of reasons. First, the behavior of indium is unique when compared to the behavior of the other group III elements on the Si(111) surface. Indium forms the linear (4x1) structure while boron, aluminum, and gallium do not form any kind of linear structures on Si(111). Second, indium on silicon is an important system which displays surfactant-mediated epitaxial growth. Surfactant-mediated epitaxy (SME) has received a lot of attention recently due to the possibility of high-quality film growth at low temperatures.

In SME, less than a monolayer of surfactant material (typically around 0.2 ML) is seen to promote smooth layer-by-layer growth at temperatures that would give 3D island growth on the bare substrate. Most models of the phenomena are based on kinetic arguments and include ideas such as a decrease of the diffusion barrier for crossing a surface step (Esch et al. 1994) or a decrease in surface mobility leading to an increase in the 2D island nucleation density (Oppo, Fiorentini, and Scheffler 1993). In either case, for a quantitative description of experimental data the models need accurate values for

the activation energies. These can be derived theoretically through first principles calculations, but only if the exact atomic structure of the surface or of the surface steps is known.

The two TED data sets used for this study were collected by Prof. Y. Tanishiro and Dr. K. Nishii at the Tokyo Institute of Technology. The intensities in one data set were measured in Japan and then sent to Northwestern as a list of numbers to be analyzed by direct methods. The other data set was sent to Northwestern University in the form of a 12-bit digitized image of a single diffraction pattern to be measured and analyzed.

4.3.1 Background

Indium forms a rich variety of surface structures on Si(111). The ($\sqrt{3}$x$\sqrt{3}$) reconstruction consists of 1/3 of a monolayer of In adatoms sitting in T_4 sites (Nicholls et al. 1985; Woicik et al.1993). With increasing In coverages first a ($\sqrt{31}$x$\sqrt{31}$) structure appears followed by the 4x1 (Tanishiro et al. 1996). Little is known about the ($\sqrt{31}$x$\sqrt{31}$) structure other than it has a higher In coverage than the ($\sqrt{3}$x$\sqrt{3}$) reconstruction, and no consensus exists for the (4x1) structure with proposed models ranging from two to four In atoms within the unit cell (0.5 ML to 1 ML coverage). Between 1.0 ML and 1.2 ML still more 2D structures form before the creation of 3D metallic In islands. These high In coverage surfaces have been studied almost

exclusively through STM and are seen to have periodicities of (1x1) and ($\sqrt{7}$x$\sqrt{3}$) (Kraft, Ramsey, and Netzer 1997). Filled-state STM images of the (4x1) surface (Nogami, Sang-il Park, and Quate 1987; Sang-il Park, Nogami, and Quate 1988; Tanishiro et al. 1996; Stevens, Worthington, and Tsong 1993) show two lines per unit cell running parallel to the shorter side of the unit cell. In some particularly good quality images, these lines can be seen to consist of broad peaks which overlap each other and blur together to form the line. Broad peaks in one line lie in-between the peaks from a neighboring line so that a zigzag pattern is formed.

Based largely on the STM images, several models for the (4x1) structure have been proposed. The most straight-forward interpretation of the STM images, namely that the broad peaks each correspond to one In atom adsorbed on an unmodified Si(111) surface, leads to the model shown in figure 4.5a. This model was proposed by Cornelison, Worthington, and Tsong (1991) and by Stevens, Worthington, and Tsong (1993) and was shown to be the best fit to their ion-scattering spectrometry (ISS) data. The coverage for this model is 0.5 ML. In contrast, Auger (Nakamura, Anno, and Kono 1991; Saranin et al. 1997) and photoemission (Abukawa et al. 1995) measurements indicated a higher In coverage of 0.75 - 1.0 ML, and three different structures in this coverage range have been proposed (figs. 4.5b, 4.5c, and 4.6). Figure 4.5b shows a model proposed by Nakamura et al. (1991) and refined by Finney et al. (1994) in which 1 ML of In sits on T_4 and H_3 sites of an unreconstructed Si double layer. Finney et al. justified a coverage of 1 ML by showing a Patterson map calculated from X-ray

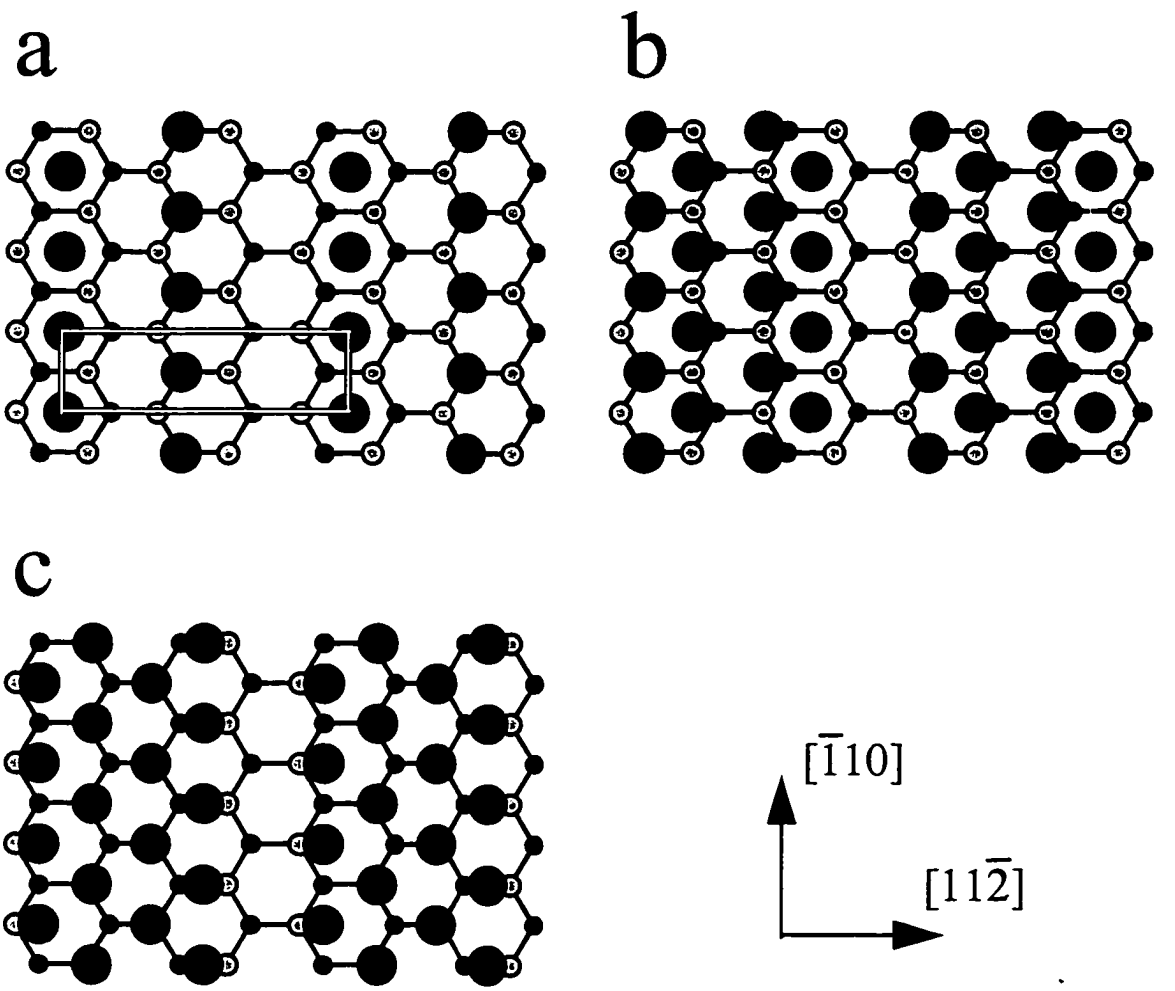

Figure 4.5. Indium adatom models for the Si(111)-(4x1)/In surface. The large black atoms represent indium. a) Half of a ML of indium in H_3 and T_4 sites as suggested by Cornelison, Worthington, and Tsong (1991). The (4x1) unit cell is outlined. b) One ML of indium in H_3, T_4, and bridge sites as suggested by Nakamura et al. (1991). c) One ML of indium in T_1 sites as suggestd by Abukawa et al. (1996).

diffraction data from the Si(111)-(4x1)/In surface and pointing out that it contains too many peaks to be explainable with a 0.5 ML coverage. While this is true if one assumes that no Si atoms participate in the reconstruction, the inclusion of Si allows for a consistent explanation of the Patterson map at lower In coverages. Figure 4.5c shows

another 1 ML model proposed by Abukawa et al. (1996). In their study, Abukawa et al. looked at photoemission spectra and concluded that the silicon substrate was ideally terminated in a one-to-one bonding arrangement with the In overlayer, i.e. every In atom resides in a T_1 site. Finally, figure 4.6 shows a model that was recently proposed by Saranin et al. (1997). Saranin et al. showed that STM images of the surface still revealed a (4x1) periodicity even when the In atoms in the Si(111)-(4x1)/In structure were displaced with hydrogen. This, they argued, proves that the reconstruction is due largely to a rearrangement of substrate Si atoms. Following the extended Pandey chain model proposed for the Si(111)-(3x1)/Metal surface (Erwin 1995) they constructed the Si dimer chain model shown in figure 4.6. The coverage of 0.75 ML for this model was estimated from auger data in conjunction with STM observations. However, a coverage of 0.75 ML is unlikely since it would prohibit the mirror or glide planes which have been shown to be a part of the structure by several diffraction and scattering techniques (see section 4.3.4).

4.3.2 Experimental Details

Since the data was collected in Japan, the sample preparation procedure differed from the one described in section 1.2.2. In this new sample preparation procedure a 7 mm x 1 mm piece of silicon is cut from a 0.4 mm thick (111) wafer. A hollow is mechanically ground into the wafer, and the bottom of the hollow is thinned by in-situ DC heating and oxygen etching (Ozawa et al. 1990) in a 100 kV UHV electron

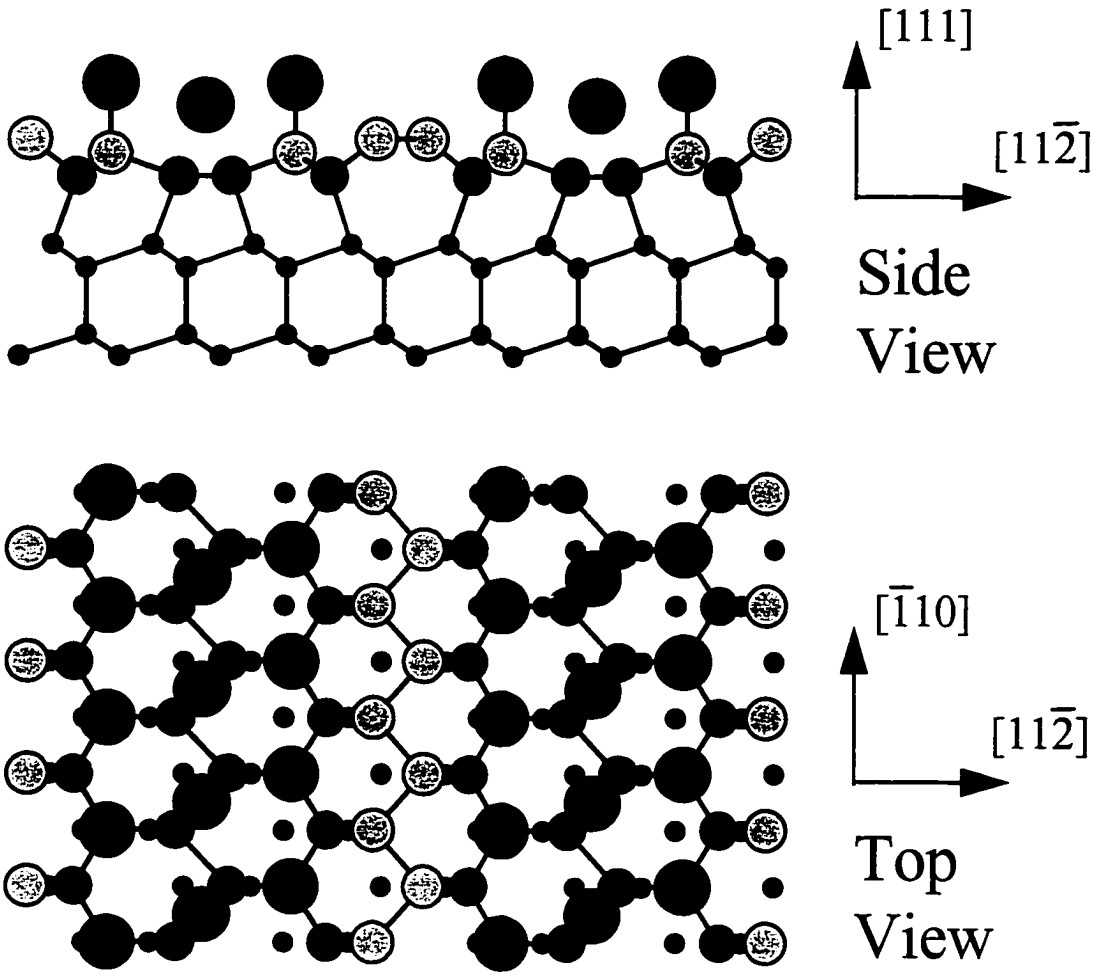

Figure 4.6. Model of Si(111)-(4x1)/In surface proposed by Saranin et al. (1997) which includes silicon dimer chains. The large black atoms represent indium, and everything else is silicon.

microscope (Takayanagi et al. 1978). After the 7x7 native reconstruction is seen to form, 1 ML of In (as measured by a quartz oscillator) is deposited onto the Si substrate which is kept at about 300 °C. During the In deposition the surface periodicity changes from 7x7 to 1x1. A 450 °C anneal then desorbs some of the indium and produces the ($\sqrt{3}$x$\sqrt{3}$) structure. Finally, another deposition of 0.4 - 0.5 ML of In onto the surface at

300 °C creates the (4x1) structure. TED intensities were recorded on either Fuji FG films or on Imaging Plates.

4.3.3 Measurement of the Diffraction Intensities

The data set which was processed in Japan was recorded on film. The single 12-bit digitized image that was sent to Northwestern for processing was recorded on an imaging plate. The 15 strongest measured intensities for the two data sets are shown side by side in table 4.2. It should be noted that the two data sets came from two

Table 4.2
Comparison of Strongest Reflections

h	k	Image Plate	Film
6	0	8.33	8.53
3	1	7.10	7.54
5	0	6.05	6.95
5	1	5.38	6.22
4	1	4.78	5.48
1	1	3.94	5.01
6	2	2.74	3.05
9	1	2.40	2.72
2	0	2.40	1.31
8	1	2.27	2.61
11	0	2.22	1.63
3	2	1.97	1.12
5	2	1.96	2.03
7	0	1.96	2.15
3	0	1.96	2.00

Notes: The image plate data was measured using the cross-correlation technique at Northwestern University. The film data set was measured and symmetry averaged in Japan.

different samples. The close agreement for the strongest intensities highlights the fact that the effects of crystal tilt and sample thickness are more significant for the weaker reflections, and they have relatively small percentage effects on the strongest reflections. This is critical for both the direct methods analysis of the TED data and for the kinematical intensity R-factor refinement step of this investigation, both of which hinge on the stronger reflections. Multislice and dynamical scattering theory were not used to simulate diffraction intensities, since in this case the sample thickness and amount of crystal tilt were not measured.

The cross-correlation technique (section 2.2) was used to measure the surface beam intensities from the 12-bit image sent to Northwestern. The intensities were then symmetry averaged according to the assumed symmetry of the reconstruction. With an assumption of p2mm for the Patterson symmetry (the symmetry seen in the diffraction pattern) 27 independent intensities comprised the final data set. The lack of repeat measurements (a through-exposure time series) for the intensities made accurate error estimates impossible, and the structure refinement process was done using an R-factor measure of agreement between simulated and measured intensities.

4.3.4 Structure Determination

Although the symmetry of the structure is not completely known, ISS data (Cornelison, Worthington, and Tsong 1991) and RHEED data (Nakamura, Anno, and Kono 1991) have suggested glide or mirror planes parallel to $[1\bar{1}2]$ (the longer side of

the unit cell). A glide plane along this direction seems unlikely, since its existence would require the extinction of all (h,0) reflections where h is odd, and the TED data show significant intensities at these points. Accordingly, the diffraction pattern was analyzed with the three possible plane groups of p2mm, p1m1, and p2gm. It was also noted that the (0,1) reflection is too weak to be detected in the TED pattern. With a mirror along the $[1\bar{1}2]$ direction, the absence or near absence of the (0,1) spot suggests that the scattering potential on each of the two mirror planes within a unit cell is the same or nearly the same (a strong argument against an odd number of In atoms in the unit cell). Alternatively, without a mirror along the $[1\bar{1}2]$ direction, the extinction of the (0,1) spot could be caused by a glide plane parallel to $[\bar{1}10]$. For completeness, the pg plane group was also investigated.

Of all the symmetries investigated, only three plausible scattering potential maps were generated and are shown in figure 4.7. The map shown in figure 4.7a suggests 4 In atoms per unit cell (1 ML coverage) and is consistent with the models proposed by Abukawa et al. (1996) and Nakamura et al. (1991). This map also shows the possibility of a slight modification to the Abukawa model by having faint peaks at locations which could be interpreted as arising from a silicon dimer chain (arrowed sites in figure 4.7a). The map shown in figure 4.7b is not interpretable in terms of any previously proposed model. Instead it suggests a structure of zigzag chains of In separated by rows of Si, or possibly chains of Si separated by rows of In. Finally, the map seen in figure 4.7c also

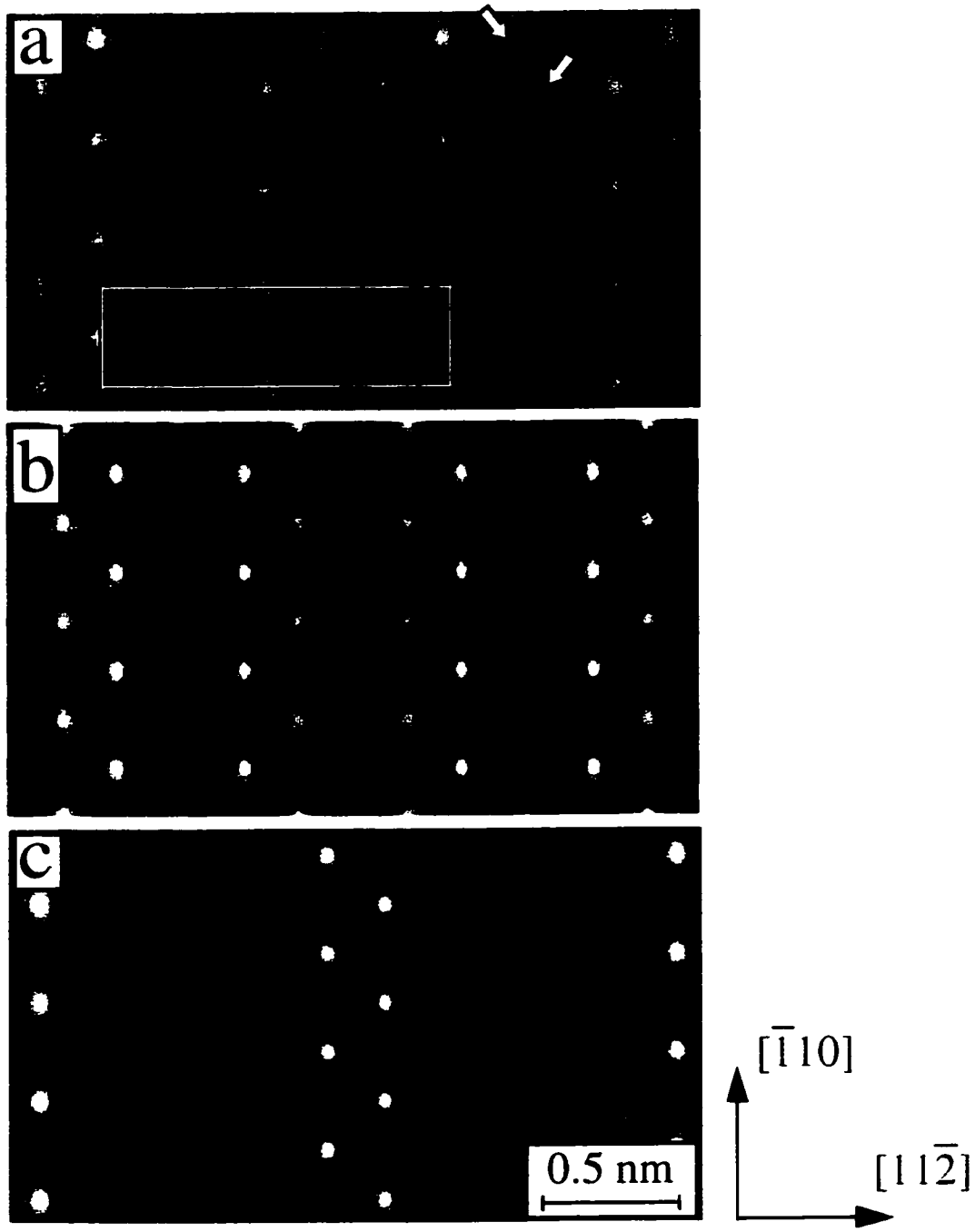

Figure 4.7. Three possible scattering potentials for the Si(111)-(4x1)/In surface, calculated using measured amplitudes and phases estimated through direct methods. Arrows in (a) show a possible Si dimer chain, and a (4x1) unit cell is outlined. The symmetry for each image is a) p2mg, b) p2mm, and c) p2mg.

cannot be interpreted in terms of previously proposed models and suggests a new structure for the surface. It appears to indicate a single chain of In atoms and a neighboring partial Si double layer containing a Si chain.

All of the possibilities discussed above were tried as initial starting structures for refinement based on kinematically simulated diffraction intensities. As mentioned before, reliable error estimates for the intensity measurements were not available, and an R-factor was used as a measure of agreement between the simulated and the measured intensities. Along with the surface atom positions, one underlying double layer was allowed to relax for the fit, and two Debye-Waller terms (one for In and one for the surface Si) were allowed to vary resulting in either 8 or 10 fitting parameters depending on the particular model. All refinement calculations were done with the restriction of p1m1 symmetry. Only two of the models gave adequate fits to the measured intensities. The modified Nakamura model (with a Si dimer chain added) shown in figure 4.8a gave an R-factor of 0.18, and the completely new model shown in figure 4.8b gave an R-factor of 0.19. The new model seen in figure 4.8b was suggested by the scattering potential map shown in figure 4.7c. The next best R-factor achieved out of all of the other initial starting structures was for the unmodified Abukawa model with R=0.34.

While diffraction intensity simulations alone are not able to discriminate between the two models shown in figure 4.8, the 0.5 ML model in figure 4.8b can be chosen as the correct structure based on the other available experimental data. Abukawa et al. (1995) interpreted features in their photoemission measurements as arising from

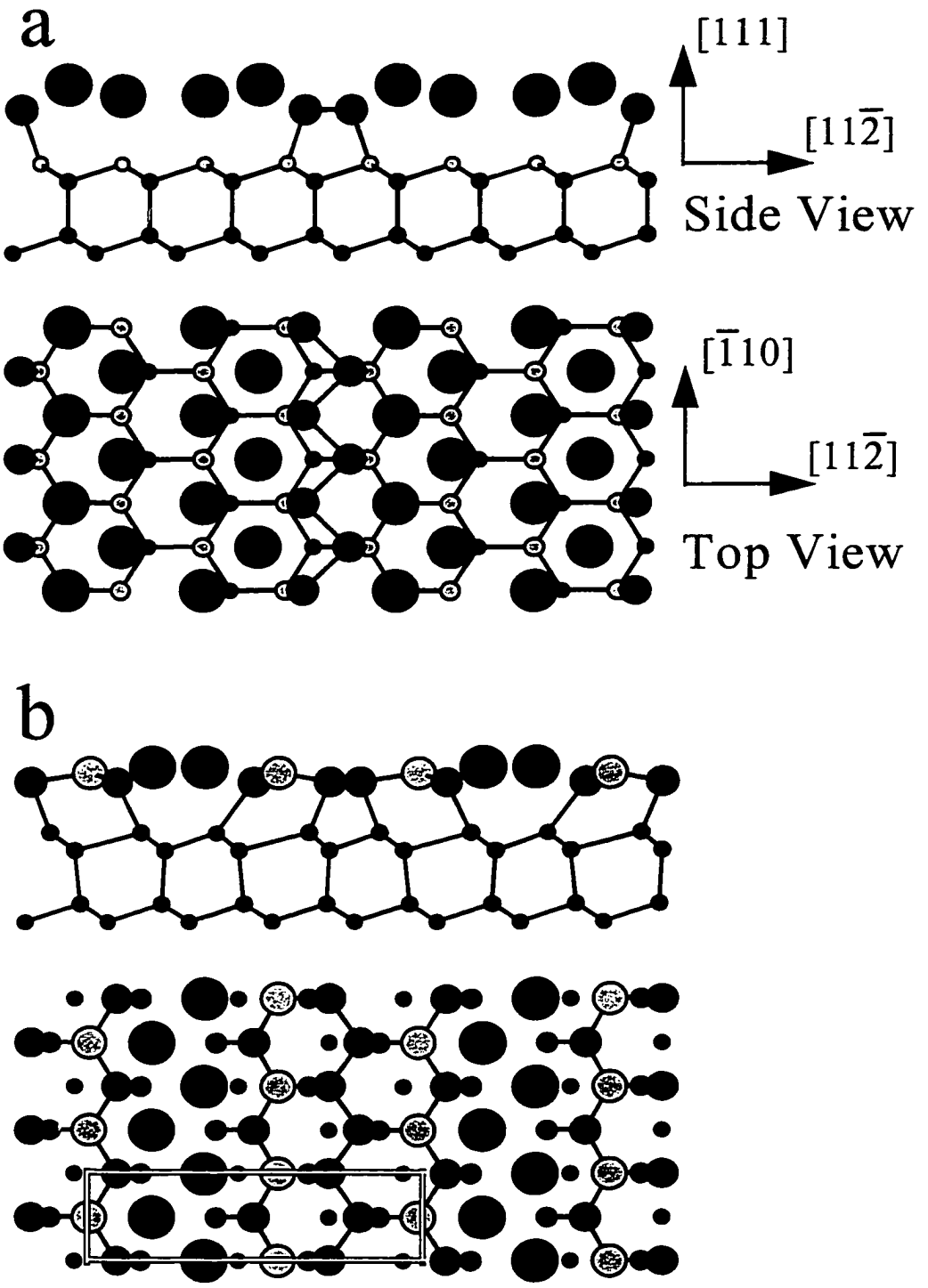

Figure 4.8. Two models for the Si(111)-(4x1)/In surface which provide a good fit to the measured diffraction intensities. a) Modified model of Nakamura et al. (1991) with silicon dimer chain added (R=0.18). b) New 0.5 ML model with silicon dimer chain (R=0.19).

sp^3 hybridized dangling silicon bonds. Two such bonds can be seen in each 4x1 unit cell for the structure in figure 4.8b (on the lighter-shaded Si atoms). The dangling bonds can also explain the filled-state STM images. It seems likely that if the In atoms sit low enough in the missing silicon row trench in the Fig 4.8b structure, a positively biased STM tip would primarily image the electrons residing in the dangling bond states on the uppermost silicon atoms. If this is true, then the filled-state STM images would consist primarily of a zigzag chain of peaks separated by about 0.5 nm, which is precisely what the filled-state STM images do show. Also, if the 1 ML In coverage for the figure 4.8a structure was the correct coverage, then there would be four distinct 2D surface phases all existing in the narrow coverage range of 1.0 to 1.2 ML (the 4x1, the 1x1, and two different $\sqrt{7}x\sqrt{3}$ structures). While not impossible, such a situation is unlikely, and again one is led to favor the lower-coverage figure 4.8b model over the structure shown in figure 4.8a. Finally, both photoemission (Abukawa et al. 1995) and inverse photoemission (Hill and McLean 1997) experiments have indicated that the 4x1 surface has a one-dimensional metallic electronic structure. Along the $[11\bar{2}]$ direction (the long side of the unit cell) the surface is semiconducting. However along $[\bar{1}10]$ (the short side of the unit cell) the surface shows metallic character, suggesting metallic In bonds extending only in this direction. With the indium chains extending in the $[\bar{1}10]$ direction and isolated from each other along the $[11\bar{2}]$ direction, the 0.5 ML model shown in

figure 4.8b is able to explain the 1D metallic behavior. The atomic positions in the final refinement of the figure 4.8b structure are shown in table 4.3.

Table 4.3
Refined Atomic Positions for Si(111)-(4x1)/In

Atom type	x	y	z
In	0.00	0.0	0.000
In	0.85	0.5	0.000
Si	0.22	0.0	0.000
Si	0.66	0.5	0.000
Si	0.38	0.0	-0.043
Si	0.46	0.5	-0.043
Si	0.18	0.5	-0.043
Si	0.71	0.0	-0.043
Si	0.28	0.0	-0.280
Si	0.05	0.5	-0.280
Si	0.79	0.0	-0.280
Si	0.52	0.5	-0.280
Si	0.12	0.0	-0.363
Si	0.37	0.5	-0.363
Si	0.61	0.0	-0.363
Si	0.87	0.5	-0.363

Notes:. The x-axis is taken along the $[1\bar{1}2]$ direction, and the y-axis is along the $[\bar{1}10]$ direction. The positions of the Si atoms along the [111] direction have been estimated from their bulk values. The positions are listed in terms of the unit cell with dimensions of A=13.30 Å, B=3.84 Å, and C=9.40 Å.

4.4 Conclusions

Figure 4.9 shows the two linear reconstructions discussed in sections 4.2 and 4.3 along with the linear Si(111)-(5x2)/Au reconstruction (Marks and Plass 1995). The similarities between the structures are striking. Each reconstruction consists of a partial

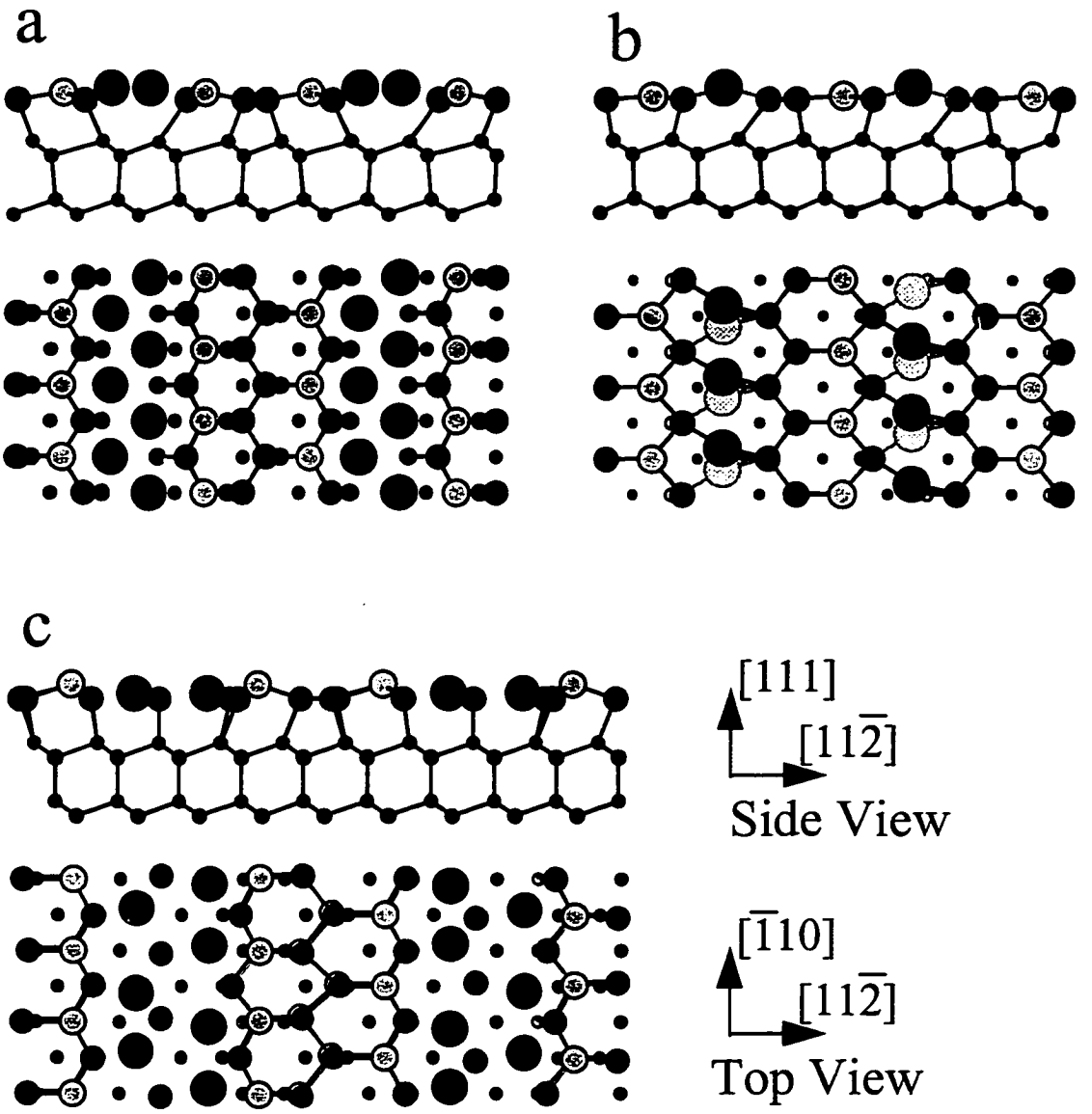

Figure 4.9. Solved linear reconstructions on the Si(111) surface. Large black circles are the metal atoms. a) Si(111)-(4x1)/In b) Si(111)-(3x1)/Ag c) Si(111)-(5x2)/Au.

silicon double layer containing a silicon dimer chain. In both the (3x1)/Ag and the (4x1)/In structures a missing Si row is replaced by the metal atoms, and in the (5x2)/Au structure two Si rows have missing top layers which are replaced by Au atoms. The

similarities show that the metal-induced linear reconstructions of the Si(111) surface are primarily a substrate reconstruction.

General comparisons can even be made with the native Si(111)-(7x7) reconstruction as pointed out by Saranin et al. (1997) for the case of (4x1)/In. (While the model proposed by Saranin et al. (fig 4.6) cannot explain the diffraction data, it does correctly incorporate a reconstructed silicon double layer with dimer chains which led them to make some interesting observations.) Saranin et al. noted that a silicon row on one side of a dimer chain must form a stacking fault, while the row on the other side of the dimer chain will remain unfaulted. A similar interplay between faulted and unfaulted halves of the unit cell exists in the (7x7) surface structure. Therefore, the metal-induced linear reconstructions on Si(111) in once sense can be viewed as hybrids of the native (2x1) structure with its dimer chains and the native (7x7) structure with its stacking faults. The main distinction for the (7x7) surface is the fact that the faulted and unfaulted regions are separated by dimer rows rather than dimer chains. However, in the formation of both dimer rows and dimer chains the basic energetics are the same. While a price is paid in raising strain energy and in producing a stacking fault, it is more than made up for by a reduction in surface energy obtained through the saturation of dangling bonds.

CHAPTER 5: NUCLEATION MECHANISM IN CUBIC BN FILM GROWTH

5.1 Motivation for Study

The cubic form of boron nitride (c-BN) has the same crystal structure as diamond and shares many of its attractive properties. It is extremely hard (60 - 70 GPa), has a high thermal conductivity (2 - 9 W $cm^{-1} K^{-1}$), and possesses a wide band gap (~6 eV) (Vel, Demazeau, and Etourneau 1991). Furthermore, unlike diamond which currently can only be p-type doped, c-BN has been successfully doped both p and n type making it a strong candidate for wide band gap semiconducting applications. Also c-BN will not react with iron at high temperatures as diamond will, so c-BN has potential as a tool coating for machining ferrous based alloys.

With such widespread potential uses, the growth of high quality c-BN films has been extensively studied. While some progress has been made, the current quality of c-BN films is not good enough for commercial applications, and many questions about growth mechanisms remain unanswered. By far the most important question concerns the role played by ion bombardment. It is generally accepted that some form of ion bombardment is needed during growth to form the cubic phase. It is also known that the ion bombardment creates large compressive stresses in the growing material, and that these compressive stresses contribute to film adhesion problems. A combination of compressive stress and chemical attack by ambient water vapor has been blamed for

cracking and delamination typically seen for c-BN films grown to a thickness of 200 nm or greater (Cardinale et al. 1994).

Recently the work of McKenzie et al. (1995) and Hahn et al. (1997) have shown that the ion bombardment is most important for nucleating the cubic phase. Once the nucleation step has occurred, less-severe bombardment (lower ion energy and/or flux) is capable of sustaining c-BN growth. By lowering the ion energy after c-BN nucleation took place, Mirkarimi et al. (1997) was able to grow a 700 nm cubic BN film which did not delaminate from its substrate. While this represents a significant breakthrough, 700 nm is still not thick enough for commercial applications. Further progress is hindered by the lack of an atomic-scale understanding of the ion-induced nucleation mechanism. In order to optimize the nucleation and growth process to minimize the level of residual compressive stress, one needs an accurate model from which to gain new insight and to predict better techniques. The c-BN film formation process is simply too complex with too many variables (e.g. substrate temperature, ion incidence angle, ion energy, ion mass, ion flux, boron and nitrogen flux, vacuum level, and substrate material) to expect rapid progress to be made through trial-and-error based attempts at film growth.

The work described in this chapter gives an atomic-scale description of the ion bombardment induced nucleation of c-BN. The proposed nucleation mechanism is consistent with all of the experimental observations on c-BN film growth reported in the literature, and it even offers an explanation of difficulties in reproducibility which has been seen by a number of researchers working in the field.

5.2 Background

5.2.1 Crystal Structures of Boron Nitride

Figure 5.1 shows the four basic crystal structures of BN. Hexagonal BN (h-BN) and rhombohedral BN (r-BN) are characterized by an ordered stacking sequence of sp^2-bonded sheets analogous to the sp^2-bonded sheets found in graphite. Another form of sp^2 BN, turbostratic BN (t-BN), has a disordered stacking sequence with each sheet

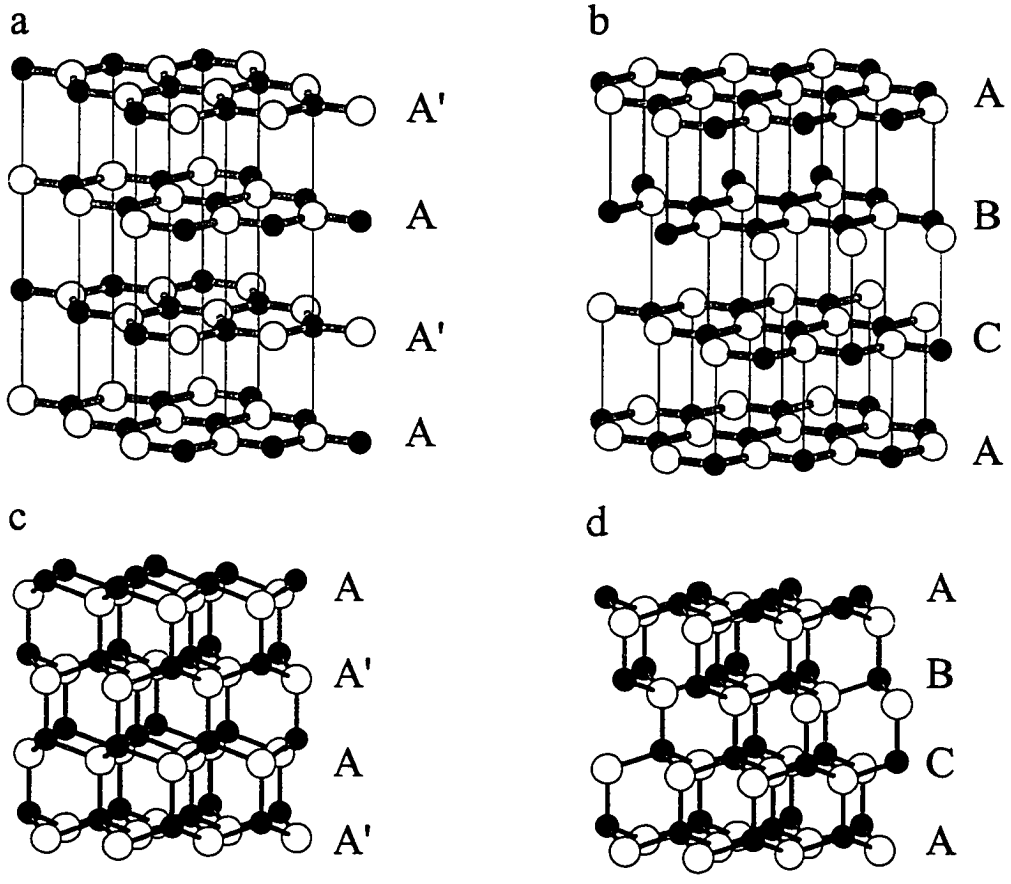

Figure 5.1. Four crystal structures of BN. Letters to the right indicate the stacking sequence of the layers. a) hexagonal b) rhombohedral c) wurtzitic d) cubic.

randomly rotated about an axis parallel to the stacking direction. Cubic BN and wurtzitic BN (w-BN) are characterized by sp^3-bonded networks analogous to diamond. Cubic BN crystallizes in the zinc blende structure, and w-BN has the wurtzite structure.

Early work on the formation of c-BN was done at high temperatures and pressures (Wentorf 1961; Bundy and Wentorf 1965), and the BN phase diagram was formulated from data taken under these extreme conditions. The coexistence line between hexagonal BN and cubic BN was extrapolated from the region of high temperature and pressure down to the region of room temperature and atmospheric pressure under the assumption that BN behaved essentially the same as carbon (Vel, Demazeau, and Etourneau 1991). Therefore, it has long been thought that the thermodynamically stable form of BN under standard conditions is h-BN, and that c-BN is a metastable phase. However, these assumptions have recently been challenged, and it has been suggested that the cubic phase is actually the thermodynamically preferred form of BN at room temperature and atmospheric pressure (Nakano and Fukunaga 1993; Solozhenko 1993; Sachdev et al. 1997). In either case, as pointed out by Mirkarimi, McCarty, and Medlin (1997) and by Kulisch and Reinke (1997), a large activation barrier must be overcome to transform h-BN to c-BN or to transform c-BN back to h-BN. What matters is that hexagonal BN is the less-dense phase, and although it may be due entirely to kinetics, h-BN forms much more readily than c-BN under standard conditions of pressure.

5.2.2 Synthesis of Cubic Boron Nitride

c-BN was first synthesized from h-BN in 1957 using high temperatures and high pressures (Wentorf 1957). Current commercial production using catalysts still involves pressures around 6 GPa at temperatures near 1700 °C to produce a powder of small c-BN crystals (Vel, Demazeau, and Etourneau 1991). The c-BN powder can then be used as an abrasive or sintered to form cutting tools. The extreme conditions needed for these fabrication techniques make them costly, and alternative routes to obtaining c-BN are desirable.

In 1979 M. Sokolowski showed that w-BN could be deposited with a pulsed plasma deposition method. This sparked an interest in using thin-film growth techniques to grow c-BN, and several different methods have been shown to work. These include plasma enhanced chemical vapor deposition (PE-CVD) (Okamoto et al. 1990; Yokoyama et al. 1991; Saitoh and Yarbrough 1991; Ichiki, Momose, and Yoshida 1994; Song et al. 1994; Dworschak, Jung, and Ehrhardt 1995), ion beam assisted pulsed laser deposition (Doll et al. 1991; Ballal et al. 1993; Friedmann et al. 1994; Medlin et al. 1994; Mirkarimi et al. 1995), ion beam enhanced vapor deposition (Ikeda 1992; Kester and Messier 1992), ion plating (Ikeda, Kawate, and Hirai 1990; McKenzie 1993), and rf sputter deposition (Mieno and Yoshida 1990; Kidner, Taylor, and Clarke 1994). The one common element found in all of these techniques is the bombardment of the growing film with a flux of energetic ions. The range of ion energies used in typical cubic BN growth experiments varies from 100 eV up to 1 keV. While some isolated

reports have appeared claiming the formation of c-BN without ion bombardment (Pryor et al. 1994; Phani, Roy, and Rao 1995), the results have not been found to be reproducible and are generally viewed with great skepticism.

5.2.3 Microstructure of c-BN Thin Films

The films deposited by the above mentioned techniques always show the same basic microstructure which is illustrated in figure 5.2. First, an amorphous layer about 2 nm thick forms. Two nanometers is comparable to the ion range for the ion energies

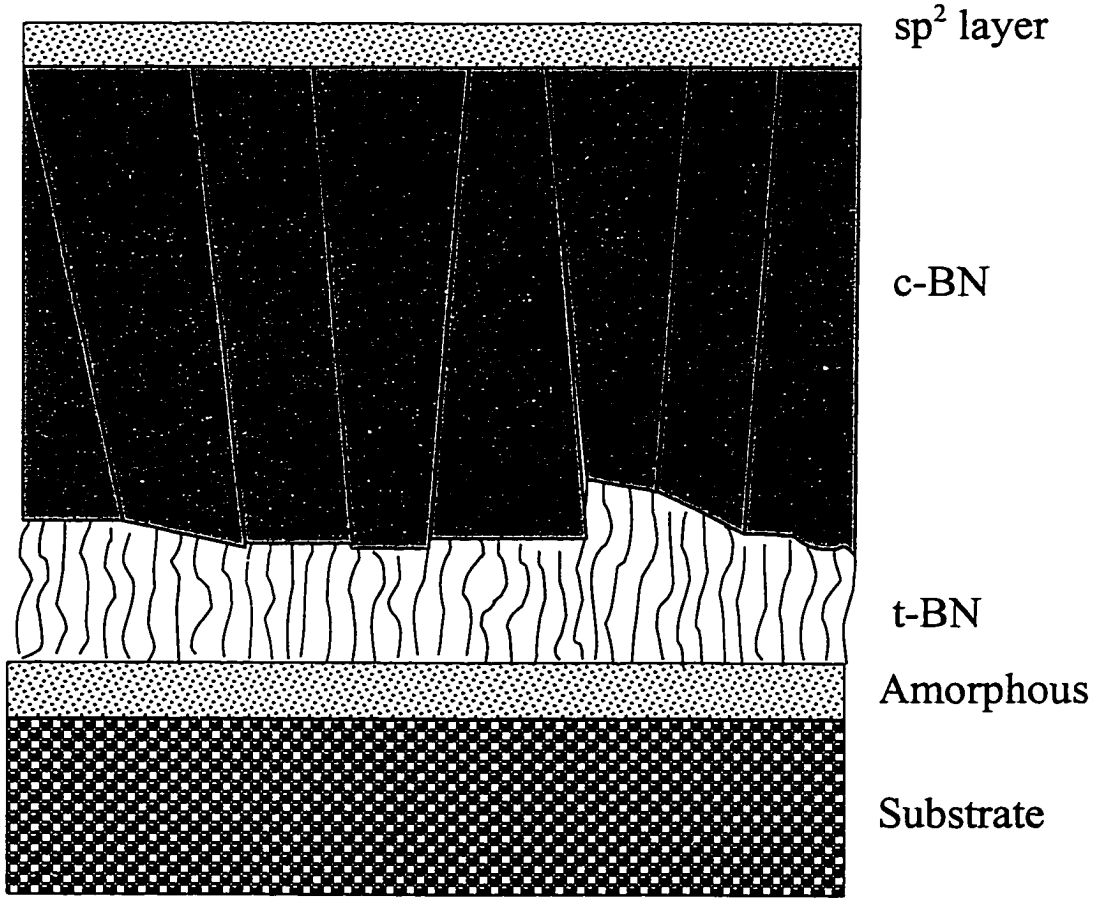

Figure 5.2. Diagram of the microstructure of c-BN films grown with ion bombardment assisted techniques.

typically used, and the amorphous layer has been attributed to intermixing between the substrate material and the boron nitride by several researchers (Kulisch and Reinke 1997). Above the amorphous layer a textured turbostratic BN layer extends for another 2 to 5 nm. The graphite-like sheets in the t-BN layer are oriented vertically with their edges exposed on the growth surface. McKenzie (1993) claimed that this texture was thermodynamically driven by compressive stress. He showed that in a biaxial compressive stress field, the Gibbs free energy of vertically oriented graphitic sheets was lower than the free energy of graphitic sheets oriented parallel to the compressive stress (in the plane of the substrate). Cardinale et al. (1997) refuted this argument by considering all possible orientations of the sheets within a biaxial stress field, and showed that the orientation with lowest free energy was actually one with the sheets tilted 45° to the stress plane. Instead of being thermodynamically driven, they proposed that the texture is due to plastic deformation of the t-BN. They argued that the compressive stress should cause slip along the basal planes and kinking of the graphitic sheets. These deformation mechanisms tend to orient the sheets perpendicular to the stress field, and once all of the t-BN is oriented vertically, no further plastic deformation can take place (McCarty and Medlin 1997).

On top of the textured t-BN layer the cubic BN is seen to grow. The c-BN layer shows a columnar grain structure with the width of the columns ranging from 5 nm to 100 nm. The grains are also preferentially oriented with a cubic (111) plane parallel to

the basal planes in the t-BN layer (Zhou, Ikuhara, and Suzuki 1995; Medlin et al. 1996; Johansson et al. 1996). To explain this alignment of the (111) cubic planes with the t-BN basal planes, it has been suggested that the exposed edges of the graphitic sheets act as nucleation sites for the cubic phase (Medlin et al. 1996; Widany, Frauenheim, and Lambrecht 1996). The work presented in section 5.4 shows that it is actually an ion-induced modification of the exposed basal plane edges which allows them to act as nucleation sites as will be discussed in more detail in that section. Finally, on top of the cubic BN layer, recent results indicate the presence of 1 nm to 2 nm of sp^2-bonded material (Friedmann et al. 1994; Bouchier et al. 1994; Sene et al. 1996; Park et al. 1997; Hofsäss et al. 1997). This thin sp^2-bonded surface layer has important implications for previously proposed growth models which will be discussed in section 5.3.

5.2.4 Effect of Growth Parameters

The body of experimental work studying the effects of various growth parameters on the formation of cubic BN thin films is extensive and has recently been reviewed by Mirkarimi, McCarty, and Medlin (1997) and also by Kulisch and Reinke (1997). Here general trends in the effects of the growth parameters are identified with reference only to a few pivotal studies.

The most thoroughly investigated parameters are those involving the ion bombardment: the ion energy, the ion mass, and the ion flux. Kester and Messier (1992) were the first to show that the effect of the ion bombardment could be described by one

critical parameter related to the ion momentum available per atom incorporated into the growing film. Regardless of the species of ion, its energy, or its flux, as long as the total momentum of the ions per film atom was above a threshold value of 200 $(eV\ amu)^{1/2}$ then cubic BN would form. They also showed an upper bound in ion bombardment near 300 $(eV\ amu)^{1/2}$ above which complete resputtering of the film took place and no net growth occurred. These observations were later confirmed and refined in a study by Mirkarimi et al. (1994). With this behavior then, a decrease in ion flux can be offset by an increase in ion energy or ion mass, and a decrease in ion energy can be compensated for by an increase in the ion flux. The cubic phase will still form as long as the total momentum transferred to the film per incorporated atom remains within the window of ~200 $(eV\ amu)^{1/2}$ to ~300 $(eV\ amu)^{1/2}$. However there is evidence that the $(m_{ion}E_{ion})^{1/2}$/atom scaling for the threshold of c-BN formation breaks down for relatively low energy ions (50 eV to 200 eV) (Kulisch and Reinke 1997).

Another well-studied effect is that of the substrate temperature. Cubic BN has been grown on substrates in the temperature range of ~ 100 °C up to ~1300 °C. Reinke et al. (1995) compiled data from a number of earlier studies and showed that higher ion flux or energy levels are necessary to form c-BN as the temperature is lowered from 400 °C down to 100 °C. It has not been possible to form c-BN for substrate temperatures below ~ 100 °C. Hofsäss et al. (1997) noted that the graphitic sheets in the oriented t-BN layer underneath the c-BN became more ordered with increasing temperatures. Moreover, the work of Kester et al. (1994) indicated that the overall thickness of the t-

BN layer also increased at higher growth temperatures. The increase in t-BN thickness could be compensated for by increasing the ion flux or energy.

Finally, one potentially important and useful parameter that has not been extensively studied is the angle of ion incidence. One study by Bouchier et al. (1994) showed that for increasing incidence angles (measured from the substrate normal), a lower level of ion bombardment is necessary for c-BN growth. In another study by Mirkarimi et al. (1995), two different angles of incidence were used. For the larger angle depositions, slightly higher c-BN contents were found, and c-BN formation was possible at lower temperatures.

5.3 Current Theories

There have been a large number of theoretical treatments published on c-BN film growth, and again the reader is referred to Mirkarimi, McCarty, and Medlin (1997) and to Kulisch and Reinke (1997) for a detailed account. The goal of this section is to describe the four basic types of theories, and to point out their individual strengths and weaknesses with respect to their capabilities of explaining experimental observations.

5.3.1 Quenching

Quenching theories attribute the formation of c-BN to rapid cooling of thermal spikes caused by ion impacts. The idea of a thermal spike was first treated quantitatively by Seitz and Koehler (1956). In their treatment, an ion was modeled as depositing all of its energy as phonons at a single point in a crystal upon impact. Heat diffusion

equations were then solved to find the distribution of energy as a function of time after the ion impact. It was found that for ion energies in the range of a few hundred eV, a small region of the crystal a few nm in diameter would effectively experience temperatures of several thousand degrees for about 1 ps before the energy was dissipated. It has been argued by some researchers that the rapid quenching of the thermal spike region may allow a metastable phase to be frozen in.

Quenching models have been criticized for not being able to explain cubic BN crystal sizes of tens of nm, and for not offering a reason for the low temperature boundary seen for c-BN formation. However, Hofsäss et al. (1998) have recently revised the calculations of Seitz and Koehler (1956) with more accurate assumptions including estimating the ion energy actually transferred to phonons (which is not the ion's entire kinetic energy) and modeling the energy transfer to occur along a line in the crystal rather than at a single point. Arbitrarily taking 3 eV as the activation energy for an "atomic rearrangement process", and using the phonon frequency as the rate of rearrangement attempts, Hofsäss et al. find that all of the atoms within a cylindrical volume of length equal to the ion penetration depth and of radius of about 0.2 nm will have at least one chance to rearrange their bonding. They claim that larger crystal sizes may easily be explained by a templating effect. Once a small cylinder of the cubic phase forms, a neighboring thermal spike will solidify epitaxially on the original small grain, and eventually a large grain will build up. With respect to the cutoff temperature criticism, Dworschak, Jung, and Ehrhardt (1995) argued that the temperature in the

thermal spike zone is additive with that of the substrate. Higher substrate temperatures allow for more time before a thermal spike reaches equilibrium with its surroundings. Below a certain temperature, the spike may simply be quenched too rapidly for any c-BN to form.

In any case, one of the biggest questions about quenching is whether or not the thermal spikes are actually able to permanently rearrange any atoms at all. Mirkarimi, McCarty, and Medlin (1997) claim that recent atomistic simulations of ion impacts show that melting within the thermal spike core does not occur for high-melting-point ceramics like h-BN. Also, work done as part of this thesis at Argonne National Labs with Dr. Mark Kirk has shown that 50 keV Xe^+ ions are not able to produce significant atomic rearrangements in h-BN at room temperature. 50 keV Xe^+ ions have enough energy to create a substantial defect cascade region several nm^2 in volume in which practically every atom is knocked off of its lattice site. If this amorphized region is frozen into place or transforms into another phase apart from h-BN, then it should be easily visible in dark-field microscopy images which are sensitive to lattice strain.

In an experiment using the Hitachi H-9000 TEM at Argonne National Labs, a sample of h-BN was viewed in dark-field mode while simultaneously being bombarded with 50 keV Xe^+ ions at a dose rate of 10^{10} cm^{-2} s^{-1}. Even up to a total fluence of 10^{13} ions/cm^2, not a single amorphous region or alternate-phase inclusion was seen. Also, the transmission electron diffraction pattern from the h-BN crystal remained sharp without any indications of disorder in the h-BN lattice. These observations indicate that

diffusion occurs so rapidly in h-BN that any ion-induced damage can be quickly annealed out even at room temperature. Therefore the quenching of thermal spikes by themselves are not able to account for the formation of a new phase from h-BN. Since the Argonne experiments were done under vacuum, the possibility of thermal spikes working in conjunction with large compressive stresses to produce a new phase cannot be ruled out.

5.3.2 Compressive Stress

The early compressive stress models for c-BN growth can be classified as static stress models. It is well-known that ion-induced interstitial defects lead to film densification and cause the large residual compressive stresses seen in c-BN thin films. McKenzie et al. (1993) measured the compressive stress in-situ during c-BN growth and found a cutoff value around 4 GPa below which no cubic BN formed. They suggested that the high pressures from the compressive stress and the high temperatures provided by thermal spikes pushed the BN into a region of its phase diagram where the cubic phase is stable. As mentioned before though, the previously accepted phase diagram for BN has come into question, and a similar investigation by Cardinale et al. (1996) did not find the same sharp cutoff value of compressive stress.

Alternatively Mirkarimi et al. (1994) proposed a dynamic stress model. In their model a local instantaneous stress is determined by the steady state production and annihilation rates of interstitials and vacancies. An additional factor describing the

accumulation of defects at sinks accounts for the build-up of residual stress. They predict that the highest instantaneous stress, and hence the formation of c-BN, will take place at a depth corresponding to the maximum defect production rate. From their model they are able to account for the $(m_{ion}E_{ion})^{1/2}$/atom scaling discussed in section 5.2.4.

The major shortfall of the compressive stress models is their inability to explain the effect of the substrate temperature. Higher temperatures should allow for more defect relaxation processes to occur, thus decreasing the overall dynamic or static stress. Therefore one would expect c-BN to become more difficult at higher temperatures if compressive stress is the controlling factor, but exactly the opposite trend is observed experimentally.

5.3.3 Subplantation

Subplantation as described in detail by Lifshitz et al. (1990) to explain the growth of tetrahedral amorphous carbon (ta-C), refers to the "shallow implantation" of ions in the energy range of 1eV to 1000eV. The penetration depth of an ion in this energy range will typically be a few nm. As the ion transfers its energy to the substrate, it displaces target atoms and causes a densification of the film with the creation of many interstitials. As the density reaches a certain critical level, a spontaneous athermal transformation to sp^3-bonded material takes place. Lifshitz et al. also believed that sp^2-bonded atoms had a lower displacement energy than sp^3-bonded atoms, and they claimed

that the cubic phase would be favored due to a higher resistance to ion damage. This preferential displacement mechanism, however, has been refuted by measurements which indicate that the difference in displacement energies is only around 10 eV (Steffen, Marton, and Rabalais 1992; Koike, Parkin, and Mitchell 1992).

As in the case of the compressive stress models, subplantation models cannot account for the substrate temperature effects found for c-BN deposition. One would again expect increased temperatures to promote the relaxation of defects resulting in a less dense film. It should be noted that subplantation does a better job at describing the growth of ta-C for which it was originally formulated. In the case of ta-C there is no low temperature cutoff, and sp^3-bond formation becomes more difficult at elevated temperatures.

5.3.4 Preferential Sputtering

The preferential sputtering model has been championed by one group (Reinke et al. 1995, Kulisch and Reinke 1997). They agree that the formation of the textured t-BN layer preceding c-BN is governed by compressive stress, and they claim that the c-BN nucleation mechanism is an independent process which is not related to preferential sputtering. However, once c-BN nuclei have formed, they postulate that at a critical ion energy and flux, h-BN is preferentially sputtered to the point that the cubic phase grows more rapidly in volume than the hexagonal phase. As part of their model they also state that an incoming atom being incorporated into the film automatically takes on the

bonding hybridization of the particular phase upon which it lands. Eventually, the entire growth surface will be covered by c-BN.

To compare results from the literature, they defined the flux ratio, F, as the ratio of the flux of ions at the growth surface to the flux of boron atoms, and they plotted F vs. ion energy, E_{ion}, for many different studies. They defined F_h as the boundary line between h-BN formation and c-BN, and F_c as the boundary between c-BN and complete resputtering of the film. By a simple consideration of mass balance Reinke et al. derived the equation for the boundary lines as a function of E_{ion}, the ion angle of incidence, θ, and the temperature, T,

$$F_{h,c} = \frac{2 s_B(T)}{Y_{h,c}(E_{ion}, \theta)} \qquad (5.1)$$

where s_B is the sticking probability of boron and $Y_{h,c}$ is the sputter yield for either the hexagonal or the cubic phase. For net c-BN growth to be possible Y_h must be greater than Y_c. Measurements show that $Y_h/Y_c \sim 1.5$ (Reinke et al. 1995). At a constant temperature, equation 5.1 predicts the boundary lines to be proportional to the inverse sputter yield. For comparison, Reinke et al. fit the inverse sputter yield for Si under argon bombardment to the compiled data at 500eV and found better agreement to the boundary line than for the momentum dependence predicted by Kester and Messier (1992), and by Mirkarimi et al. (1994).

One of the strengths of the sputter model is its qualitatively correct prediction of the influence of substrate temperature. According to equation 5.1, the effect of temperature is seen in the boron sticking probability, s_B. As the temperature is lowered, s_B increases and both F_h and F_c are raised. Therefore, in agreement with experiment, a higher ion flux or ion energy is needed for c-BN growth. Also, the variation of F_h with the ion incidence angle as predicted by the sputter model is supported by the available studies of the effect. As θ increases (θ being measured from the surface normal), the sputter yield will increase and F_h should be lowered. Such a trend is shown in a limited study by Bouchier et al. (1994) and by the work of Mirkarimi et al. (1995).

The sputter model has been dealt a blow by the studies which revealed the presence of the 1 nm to 2 nm surface layer of sp^2-bonded BN sitting on top of the c-BN (Friedmann et al. 1994; Bouchier et al. 1994; Sene et al. 1996; Park et al. 1997; Hofsäss et al. 1997). The mechanism of preferential sputtering clearly predicts that the growth surface should end up consisting entirely of the cubic phase. Kulisch and Reinke (1997) have tried to explain the surface sp^2 bonding by suggesting the presence of an sp^2-hybridized surface reconstruction, but such a reconstruction would only involve the first layer of atoms and could not account for the estimated thickness of a few nm.

Although the sputter model is not able to explain the growth of cubic BN, it is still relevant to the nucleation of the cubic phase. The nucleation mechanism which is described in the next section is able to incorporate the greatest strengths of the sputter model in describing the influences of substrate temperature and ion incidence angle.

5.4 Identification of Nucleation Mechanism

5.4.1 Transmission Electron Microscopy for the Study of Ion Bombardment Effects

An accurate description of the effects of ion bombardment on BN at an atomic level is the key to understanding the formation of cubic BN thin films. In this regard, high resolution transmission electron microscopy (HREM) is a powerful tool with its spatial resolution of ~ 0.2 nm. One could expect significant insight to be gained through a basic experiment in which a sample of hexagonal BN is subjected to ion bombardment and then placed into a TEM for examination. Unfortunately, such a basic experiment is made difficult by practical considerations involving the mechanical properties of h-BN and the requirements of TEM sample preparation.

Standard TEM sample preparation techniques are incapable of producing self-supporting h-BN samples with areas that are thin enough to be electron transparent. The only alternative is to support micron-size pieces of h-BN on a fine grid structure of another material (the sample preparation process for which is described in section 5.4.2). Having a grid-supported sample does not hinder the electron microscopy in any way, but it does create problems in an ion-bombardment study. The levels of bombardment which are typically used for growing c-BN also produce a significant amount of sputtering. On a h-BN/grid sample, some of the material which is sputtered from the grid will redeposit onto the h-BN, and thereby create a contamination problem. Ion sources cannot be focused onto an individual micron-size h-BN particle, so the sputtering problem with ions is unavoidable.

Useful experiments with h-BN samples in a TEM can still be realized, however, if one uses electron irradiation as an alternative to ion bombardment. The high energy electron beam in a TEM can accomplish the same ballistic displacement of atoms from their lattice sites without sputtering any material from the support grid. An electron beam in a standard high resolution TEM using a LaB_6 filament can be focussed onto an area on the order of a micron across. A section of an h-BN piece away from the support grid can be subjected to intense electron irradiation, thus producing the required ballistic atomic displacements, and then the same section can be immediately imaged to record any changes occurring on an atomic scale.

Table 5.1 lists common accelerating voltages used in TEM's along with the corresponding maximum possible ballistic energy transfer from an electron to a boron or a nitrogen atom which occurs for a direct head-on collision. The estimates of the average number of displacements per atom (dpa) were calculated assuming a displacement energy of 30 eV and a 1 minute exposure to an electron flux of 100 Amp/cm^2 (6.24×10^{20} electrons $cm^{-2}\ s^{-1}$). A beam current density of 100 Amp/cm^2 at the sample represents an upper range estimate of what can be achieved in a TEM with a LaB_6 filament. For comparison, typical c-BN growth conditions result in an average of about 5 displacements per atom in the film (Sene et al. 1996). An examination of the dpa estimates in table 5.1 indicates that a similar number of ballistic displacements will be achieved for electron beam irradiations lasting about ten minutes at 100 Amp/cm^2.

The expectation that such electron irradiation experiments will be relevant to the deposition of c-BN films is supported by the literature. As discussed in section 5.2.3, BN always deposits first as a textured sp^2-bonded layer. It is the action of the ion irradiation on this sp^2-bonded layer which is responsible for the nucleation of c-BN. The fact that it has not been possible to form c-BN with ion energies under 50 eV (Mirkarimi, McCarty, and Medlin 1997) is consistent with the assumption that ballistic displacements play a role of primary importance. Since high energy electrons can produce the same ballistic displacements in h-BN, useful insight into ion irradiation processes can be obtained.

Table 5.1
Energy Transfer from Electrons to Boron and Nitrogen Atoms in a TEM

	Boron		Nitrogen	
Accelerating Voltage (kV)	**Max Energy Transfer (eV)**	**Estimated dpa†**	**Max Energy Transfer (eV)**	**Estimated dpa†**
1,000	402	1.0	310	1.3
400	113	0.5	87	0.5
300	79	0.4	61	0.4
200	49	0.3	38	0.3
100	22	0.0	17	0.0

†The dpa are calculated for 1 minute of electron bombardment at a current density of 100 Amp/cm^2 assuming a displacement energy of 30 eV for both B and N. The total displacement cross sections were calculated using the McKinley and Feshbach (1948) approximation to the Mott series (1929). The modified Kinchin and Pease (1955) relation was used to account for secondary displacements occurring for primary energy transfers greater than twice the displacement energy.

5.4.2 Sample Preparation

Polycrystalline hexagonal boron nitride (99.5% purity) was obtained from Advanced Ceramics Corp. in the form of a sintered rod (15 cm long, 1 cm diameter). Small flakes were scraped from the rod with a razor blade and then placed into a mortar and pestle with methanol. The h-BN flakes were crushed by hand in the methanol, and then a drop of the h-BN/methanol slurry was put onto a 1000-mesh gold grid. The methanol evaporates in minutes leaving behind micron-size h-BN pieces loosely attached to the grid. By searching through the grid square by square in the TEM, one can find several h-BN pieces favorably oriented near a major zone axis that also have regions thin enough for HRTEM.

5.4.3 Observation of Nanoarches

Figure 5.3 shows high resolution TEM images for two h-BN crystals: one viewed along the $(11\bar{2}0)$ zone axis and the other along the (0001) zone. Looking along the $(11\bar{2}0)$ zone the sp^2-bonded sheets are parallel to the beam, and each dark lattice fringe in figure 5.3a corresponds to a single sp^2-bonded sheet viewed edge-on. The (0001) zone is rotated 90° with respect to $(11\bar{2}0)$, and in this orientation the sp^2-bonded sheets lie perpendicular to the beam. The pictures in figure 5.3a and 5.3b were taken in SPEAR's UHV-H9000 TEM at an accelerating voltage of 300 kV taking care to limit the photographed regions' exposure to the electron beam. Under normal operating conditions for HREM, the current density at the sample will be roughly 1 Amp/cm^2.

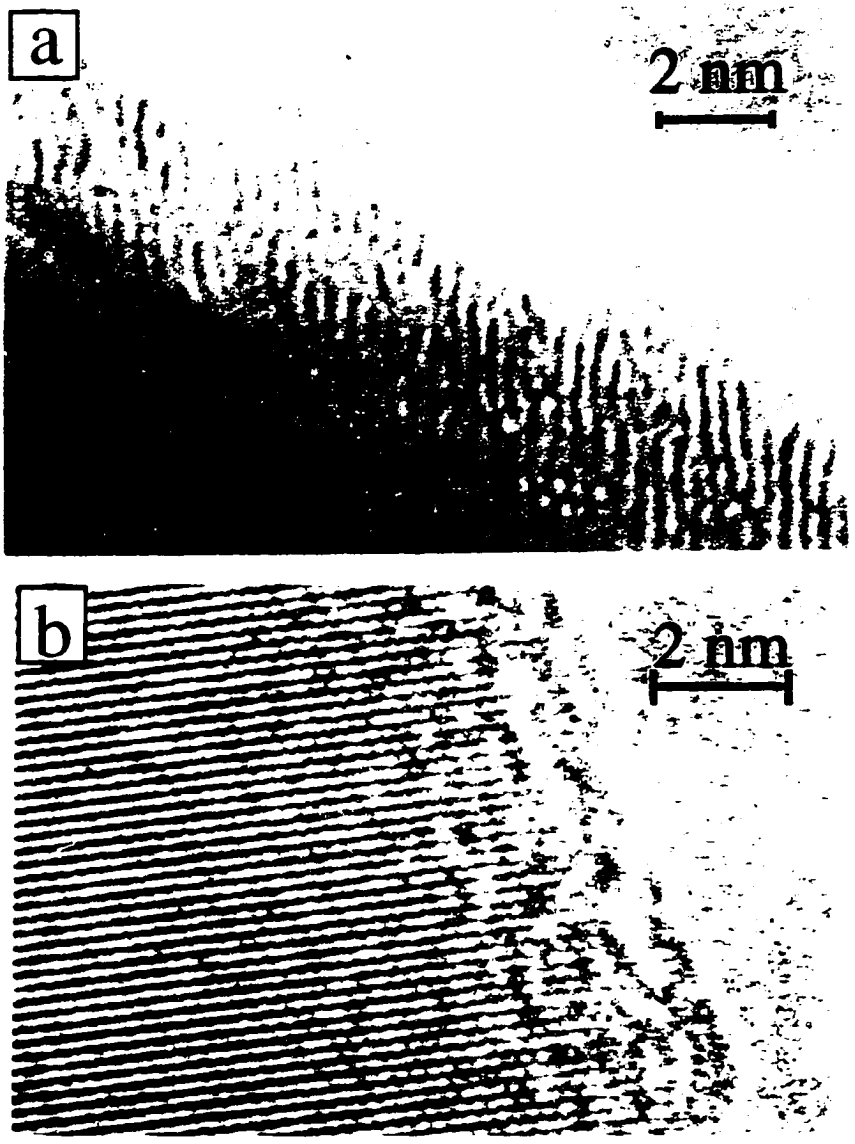

Figure 5.3 High resolution TEM images of h-BN. a) $(11\bar{2}0)$ zone. b) (0001) zone.

With 300 keV electrons, a current density of 1 Amp/cm^2 will produce only 0.004 dpa after 1 minute of irradiation (assuming a 30 eV displacement energy). The regions shown in figure 5.3a and 5.3b were not subjected to much more than a minute of

exposure to the electron beam before the images were recorded, so any ballistic displacement damage is minimal.

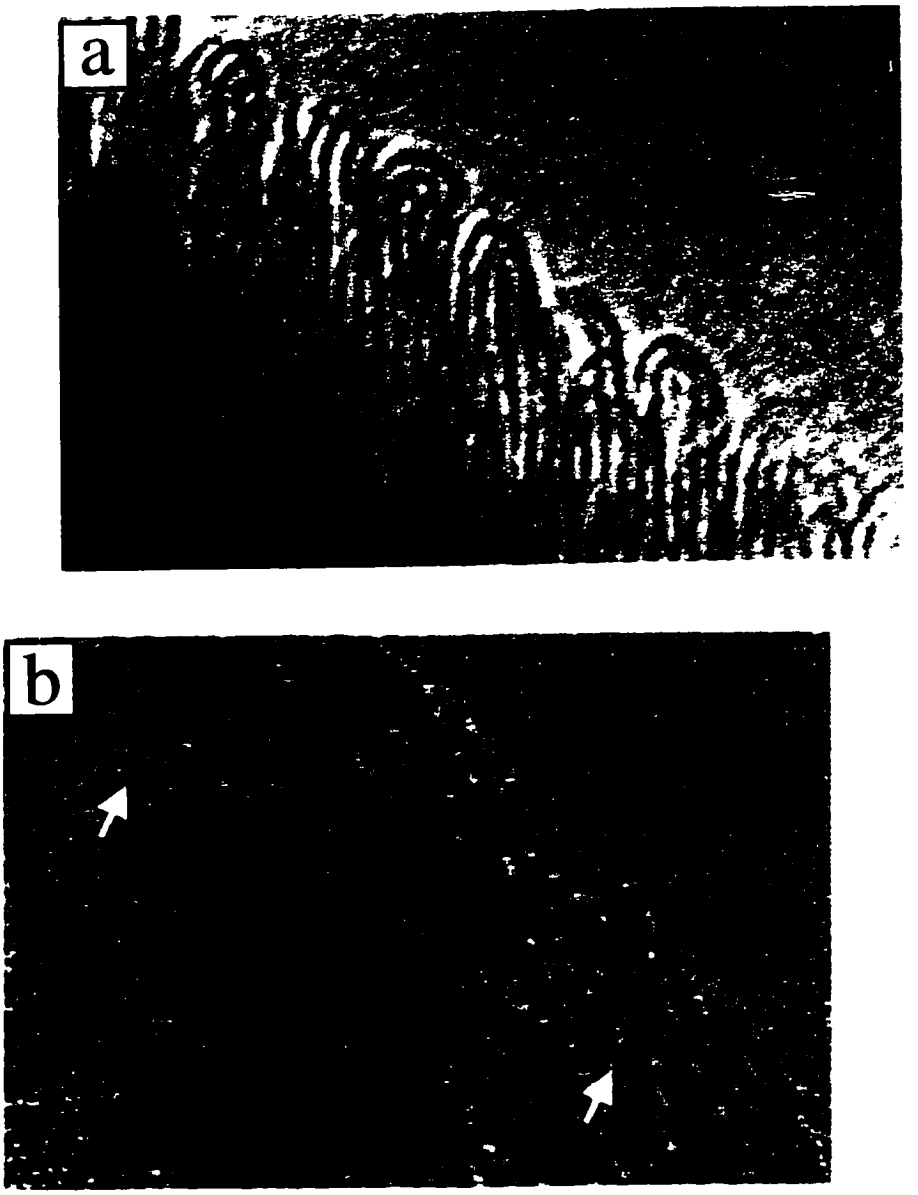

Figure 5.4. The same areas that are shown in figure 5.3 after 10 minute exposure to 300 keV electron beam with 50 - 100 Amp/cm^2 current density. a) $(11\bar{2}0)$ zone. b) (0001) zone. Arrows in (b) indicate the arches which are located at the edges of surface steps.

The pictures shown in figure 5.4a and 5.4b are from the same areas as in figure 5.3a and 5.3b, but they were recorded after an exposure to 50 - 100 Amp/cm^2 for 10 minutes. The high current density was obtained by removing the condenser aperture from the electron beam path and adjusting the bias on the Wehnelt cup in the electron gun. These irradiation conditions will produce 1.8 - 3.9 dpa - a range which is comparable to the estimated 5 dpa occurring for standard ion-induced c-BN formation (Sene et al. 1996).

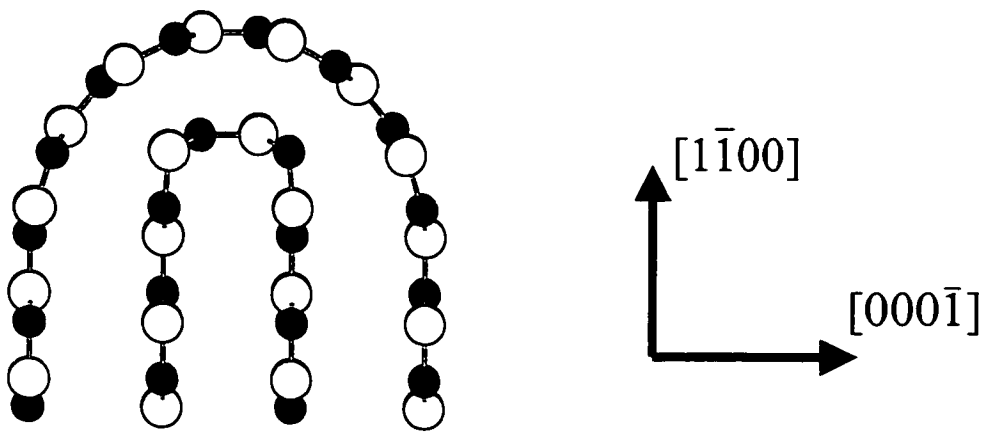

Figure 5.5. Basic model of nanoarch with 1 nm diameter.

The structures which are seen to form with the intense electron irradiation can be referred to as nanoarches. They are essentially half-nanotubes capping the ends of the sp^2-bonded sheets. A model of their basic structure as viewed along the (11$\bar{2}$0) zone axis is shown in figure 5.5. The observation of the curling of sp^2-bonded sheets under intense electron beam bombardment is nothing new. The formation of onion-like structures has

been reported for both carbon (Ugarte 1992; Banhart and Ajayan 1996; Qin and Iijima 1996) and boron nitride (Banhart, Zwanger, and Muhr 1994). However, the well-ordered semi-cylindrical capping seen here has only previously been reported for high-temperature / high pressure treatments (Horiuchi, He, and Akaishi 1995; Boulanger et al. 1995).

Before discussing the relevance of nanoarches for the nucleation of cubic BN, a few more details about their formation should be mentioned. As shown in table 5.1, 300 keV electrons are capable of transferring up to 79 eV to boron atoms and 61 eV to nitrogen atoms through ballistic collisions. These values are certainly over the displacement energies for both atoms in the h-BN lattice. The electron irradiation experiments were repeated for an accelerating voltage of 200 kV, and again the BN nanoarches were seen to form. However, 100 keV electrons were not able to create arches even for irradiations lasting up to an hour. These results show that the arches are created by the ballistic atomic displacements rather than by electronic interactions. As the electron energy is lowered, the energy transferred to atoms through nuclear collisions decreases while the energy transferred through electronic interactions increases. At 100 keV the maximum possible ballistic energy transfer has dropped to 22 eV which is less than estimated displacement energies in BN. Therefore, the lack of arch formation at 100 keV can be easily explained by the absence of ballistic atom displacements.

Another important observation was made when the experiment was repeated in a different microscope. Figure 5.6a shows a $(1\bar{1}20)$ zone-axis image taken before intense

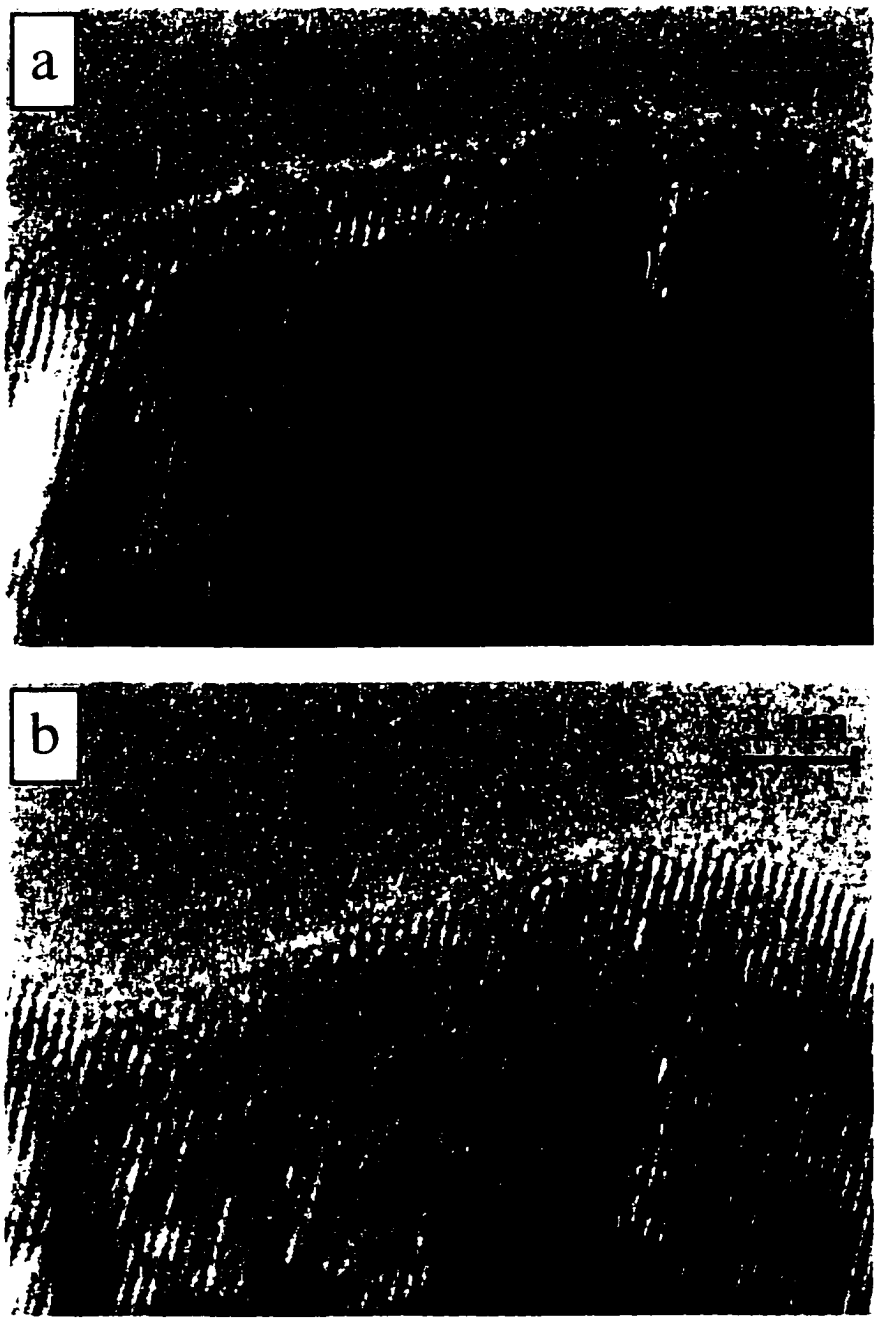

Figure 5.6. Images along $(11\bar{2}0)$ zone recorded on H-9000 TEM operating at vacuum level of ~ 10^{-7} torr. a) Before electron irradation. b) Same region after 10 minute exposure to 300 keV electrons at 50 - 100 Amp/cm^2 current density.

electron irradiation, and figure 5.6b shows the same region just after a 10 minute, 300 keV irradiation at 50-100 Amps/cm^2. The mottled contrast in figure 5.6b indicates that the h-BN crystal has sustained damage, but no evidence of nanoarch formation can be seen. The images in figure 5.6 were taken on the standard Hitachi H-9000 TEM at Northwestern University. Apart from its base vacuum level (~ 10^{-7} torr) it is identical to the UHV H-9000 connected to the SPEAR system used for the images shown in figures 5.3 and 5.4. Longer irradiation times were tried on the standard H-9000 TEM lasting up to an hour, but nanoarches could not be produced. This is in sharp contrast to the observations made with the UHV H-9000 TEM, for which nanoarch formation was easily reproduced and was verified for several different samples. Further confirmation of the vacuum level dependence was obtained through experiments on two other transmission electron microscopes. In the H-9000 at Argonne National Labs operating at a pressure around $5x10^{-7}$ torr, nanoarches could not be created. However, in a 1 MeV microscope in Japan operating at a pressure of $1x10^{-8}$ torr, arches could be easily formed in 20 minutes with irradiations of ~ 20 Amp/cm^2.

If one assumes that the driving force for the formation of the nanoarches is a reduction in the number of dangling bonds at the surface, then the difficulty in forming arches in poorer vacuum environments can be readily interpreted. Instead of the graphitic sheets creating a considerable strain energy by curling around onto themselves to saturate the dangling bonds, it is likely to be more energetically favorable for atoms

from the ambient gas to bond to the edges of the sheets (e.g. termination with a single hydrogen or with an OH group). To form an arch, the edges of the sheets must be stripped free of the contaminates, and this can only be accomplished if the incident irradiation removes atoms faster than they arrive from the residual gas.

For an order-of-magnitude estimate, we can take 10 eV for the energy required to sputter a hydrogen or oxygen atom from the surface. Then with 300 keV electrons at 100 Amp/cm^2 current density (the conditions for the H-9000 TEM experiments), each surface hydrogen or oxygen atom will experience about 4 sputtering events during a 1 minute time period. Assuming that the contaminate gas is water, the arrival rate of water molecules can be estimated assuming ideal gas behavior and a temperature of 300 K. With a partial pressure of water of 10^{-10} torr (UHV conditions), the H_2O arrival rate is 4.8×10^{-10} cm^{-2} s^{-1}. Using the density of bonding sites available on the $(1\bar{1}00)$ surface of h-BN (1.2×10^{15} cm^{-2}), the H_2O arrival rate can be written in a more useful form as 0.0024 molecules per bonding site per minute. This shows that the sputtering rate is about 3 orders of magnitude greater than the contaminate arrival rate, and in the steady state the h-BN surface will be stripped almost entirely clean.

For the 1 MeV microscope in Japan operating at 20 Amp/cm^2, the sputtering rate was about 1 per minute per oxygen or hydrogen atom. This is to be compared with an H_2O arrival rate of 0.24 per bonding site per minute (1×10^{-8} torr). Since the sputtering rate is several times greater than the contaminate arrival rate, the h-BN surface sites will again be predominately occupied by dangling bonds, and arch formation can be

expected. In the case of the standard H-9000 microscopes however, the pressure at the sample was at best 10^{-7} torr. This corresponds to a contaminate arrival rate of 2.4 per bonding site per minute, which is approaching the sputtering rate of ~ 4 per minute. It is not surprising then that arch formation doesn't take place, as contaminate atoms are replaced as quickly as they are sputtered.

It should be noted that these calculations are only rough estimates which include assumptions about the surface binding energy, the chemical identity of the contaminate atoms, and the contaminate sticking probability (implicitly taken as unity). Nevertheless, the binding energy estimate and the mass of the contaminate molecule are only likely to be off by at most a factor of 2 or 3, and so we can expect the order of magnitude to be accurate. The fact that the contaminate atom arrival rate is estimated to be about equal to the sputtering rate for a pressure near 10^{-7} torr, indicates that the proposed mechanism for the vacuum level influence is consistent with our experimental observations.

5.4.4 Significance of Nanoarches for Nucleation of Cubic Boron Nitride

The creation of BN nanoarches by ballistic atom displacements reveals a direct link between ion irradiation and the nucleation of the cubic phase of boron nitride. As mentioned briefly in section 5.4.3, the formation of nanoarches lowers the total surface energy by saturating dangling bonds at the expense of creating a significant amount of strain energy. Assuming a constant radius of curvature for an arch with a diameter of 1

nm (4 sp^2-bonded sheets across), a B-N-B bond on the outer loop of the arch will be bent by ~ 11° as projected along the [11$\bar{2}$0] direction. Eleven degrees represents a minimum estimate since some bonds will be bent to an even greater degree if the radius of curvature does not remain constant. Some experimental evidence exists for large variations in the radius of curvature for nanotubes. EELS measurements on BC_2N nanotubes (Weng-Sieh et al. 1995) suggested a puckered geometry for the tube walls since the B edge retained its sp^2-hybridized signature while the N edge indicated a relaxation towards sp^3 bonding.

We postulate that for nucleation of c-BN, the bond strain in the nanoarches lowers the barrier to sp^3 hybridization. The deposition of boron or nitrogen atoms on an arch and the formation of sp^3 bonds will release some of the strain energy. The addition of more B and N atoms will extend the sp^3 bonding network, and a small cubic BN crystal will be formed. Figure 5.7 illustrates possible steps in this cubic BN nucleation process. The structure shown in the final step (fig. 5.7d) is actually modeled after the interfacial structure proposed by Widnay, Frauenheim, and Lambrecht (1996). Through density-functional based tight-binding calculations they showed that the structure was stable. It also agrees with the texture seen in c-BN thin films (basal planes in h-BN parallel to a (111) plane in c-BN). Along the [111] direction in the cubic crystal, 3 cubic (111) planes match almost perfectly 2 hexagonal basal planes. The 5 % mismatch can be easily taken up by the h-BN with its high compressibility along the [0001] direction.

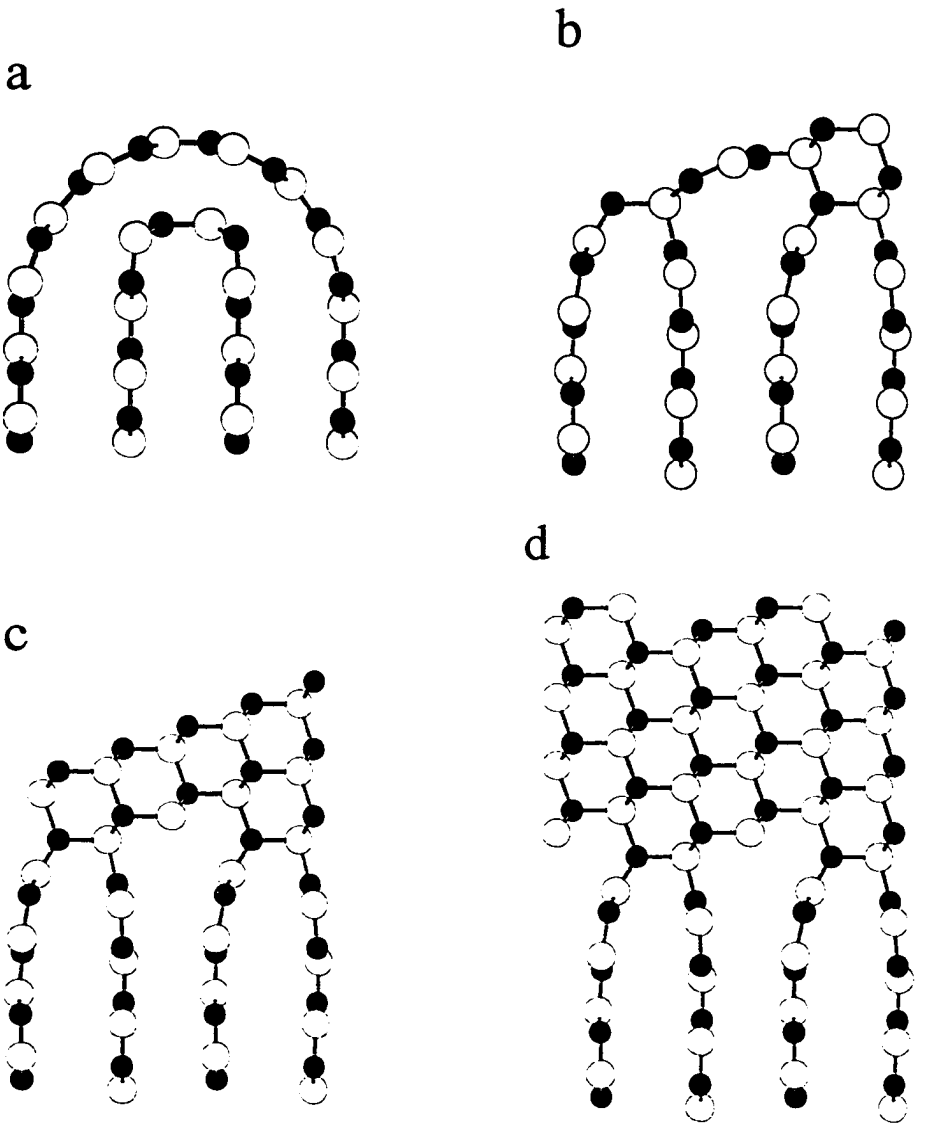

Figure 5.7. Conversion of a nanoarch to a c-BN nucleus. The structure in (d) has been shown to be stable by Widnay, Frauenheim, and Lambrecht (1996).

A new picture of c-BN film growth emerges based on the BN nanoarch nucleation mechanism. The film formation process is illustrated schematically in figure 5.8. First the ion bombardment creates the textured t-BN layer (fig. 5.8a) -- most likely through a compressive stress mechanism. The compressive stress may even be

important for compressing the sp^2-bonded sheets by ~ 5 % to obtain a good lattice match to c-BN, but the key element for nucleation is the formation of the nanoarches (fig. 5.8b). Finally, the nuclei formed through the nanoarches grow and coalesce, and the nanocrystalline c-BN film is formed (fig. 5.8c).

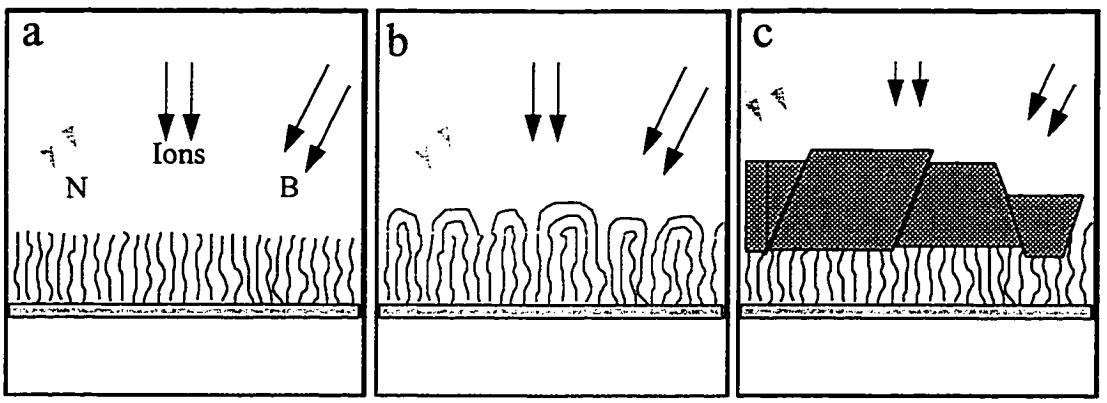

Figure 5.8. Depiction of c-BN growth process based on nanoarch nucleation mechanism. a) Formation of textured t-BN layer. b) Formation of nanoarches. c) Cubic BN nucleation and growth.

This new picture of c-BN film growth is consistent with the large body of experimental evidence available on the process. Since the removal of contaminate species which is necessary for nanoarch formation is essentially a sputtering process, the correct behavior with substrate temperature and the angle of ion incidence is predicted as in the sputter model. None of the other theories (quenching, stress, or subplantation) can explain the temperature behavior. The sputtering model itself fails to explain both the continued growth of the cubic phase at lower ion bombardment levels after nucleation has taken place and the presence of the thin sp^2 surface layer. However these

observations are still consistent with the arch nucleation model. The critical values reported for the ion energy, ion flux, and temperature are all critical values needed for nucleation and therefore are well-described as a sputtering process. After nucleation, homoepitaxial growth can continue through a different process and will not depend on sputtering. Also, while largely unpublished, a number of labs have been unable to grow c-BN even though their deposition parameters matched those published for other workers. This irreproducibility can be attributed to the vacuum level dependence found for nanoarch formation. If the contaminate arrival rate is too high, nanoarch formation will not be possible and the cubic phase will never nucleate.

5.5 Implications

The identification of the nucleation mechanism in cubic BN film growth opens up many new possibilities. To minimize the compressive stress, one can reduce the level of ion bombardment necessary to form c-BN nuclei by working in UHV conditions and raising the ion incidence angle to increase the sputter yield. It might also be possible to seed c-BN nucleation without ion bombardment using BN fullerene structures placed on the substrate before growth, as was demonstrated in the case of C_{60} with diamond (Meilunas et al. 1991). It even becomes reasonable to consider using ion beam lithography to define c-BN structures. A thin layer of t-BN could be grown on a substrate and then a pattern could be written into it using a rastered ion beam to form c-BN nuclei only in selected areas. Of course some of these ideas are highly speculative,

but it would not even have been possible to consider them without first understanding the nucleation mechanism of c-BN on an atomic scale.

CHAPTER 6: FUTURE WORK

6.1 Surface Structure Determination

The direct methods algorithm used in our lab is continuously being improved and refined. However, the current implementation is highly developed and will be effective for the solution of most surface x-ray or transmission electron diffraction problems. The most likely barriers that will be encountered will be experimental in nature, and will have to be dealt with at the data collection stage. The formation of twin domains or rotationally equivalent domains for which the reflections from one domain overlap the reflections from another have already prevented a direct methods analysis of one surface, the Sn induced Si(111)-($2\sqrt{3}$ x $2\sqrt{3}$)R30° structure. The ambiguities presented by such a data set can be avoided if the sample preparation procedure is capable of being tailored to produce a predominantly single-domain surface. For example, it has been demonstrated by Stevens, Worthington, and Tsong (1993) that a single-domain Si(111)-(4x1)/In surface can be created by using a miscut Si(111) substrate. Apart from these occasional "degenerate" domain structures, the direct methods algorithm is ready to be applied to any of a number of interesting surface structure problems.

One of the more interesting systems which could be studied further is the indium on Si(111) surface. The lowest-coverage ($\sqrt{3}$x$\sqrt{3}$) reconstruction (1/3 of a ML of In) has

been determined using a number of conventional surface-sensitive techniques (Nicholls et al. 1985; Woicik et al. 1993), and the higher-coverage (4x1) reconstruction (1/2 of a ML of In) was solved during the course of the work of this thesis (section 4.3). Yet, while the ($\sqrt{31}$x$\sqrt{31}$) structure forming for an In coverage between 1/3 and 1/2 of a ML acts as a link between the ($\sqrt{3}$x$\sqrt{3}$) and the (4x1) surfaces (Tanishiro et al. 1996), the atomic geometry for the ($\sqrt{31}$x$\sqrt{31}$)/In structure itself remains completely unknown. One might expect parts of the ($\sqrt{31}$x$\sqrt{31}$) structure to bear some similarity to fragments of the (4x1) or the ($\sqrt{3}$x$\sqrt{3}$) structures just as the (4x4)/Ag and ($\sqrt{3}$x$\sqrt{3}$)/Ag structures on the Ge(111) surface were seen to be related in chapter 3. It might also be possible that the Si(111)-($\sqrt{31}$x$\sqrt{31}$)/In surface is similar to the Ge(111)-(4x4)/Ag surface since their unit cells are close in size and both structures occur for nearly the same coverage of metal atoms. In any case, a transmission electron diffraction data set from Si(111)-($\sqrt{31}$x$\sqrt{31}$)/In should be readily analyzed through direct methods, and its solution would represent the largest previously unknown surface structure solved by applying direct methods to TED data.

Also, with all of the submonolayer structures induced by In on the Si(111) surface solved, one can work on formulating a complete surface phase diagram for the system as was done for the case of gold on the Si(111) surface (Plass and Marks 1997). Collaborative work with other groups may be required to obtain information about theoretical surface energies and accurate measurements of phase transition temperatures, however such an effort should be valuable to the surface science community.

6.2 Cubic Boron Nitride Film Growth

As described in chapter 5, the deposition of cubic boron nitride thin films is a highly complicated process, and the formation of nanoarches can only offer an explanation for the nucleation step. It may be possible that other factors work in conjunction with the formation of nanoarches to nucleate c-BN. Two limited studies (McCarty et al. 1996; Hofsäss et al. 1997) have indicated that the substrate temperature plays a role in the ordering of the textured turbostratic BN layer which forms prior to c-BN nucleation. The low temperature cutoff for the formation of the cubic phase may be due to a lack of order in the t-BN layer which prevents the formation of nanoarches. The studies of McCarty et al. (1996) and of Hofsäss et al (1997) were only preliminary and suggestive, and the effect that the temperature has on the ordering of the t-BN layer deserves more in-depth attention. One could take advantage of the BN growth capabilities available on the SPEAR system to grow thin BN films on Si substrates at varying temperatures. The plan-view geometry of the samples would be ideal for characterizing the resulting structures of the t-BN films through HREM and TED.

Another alternative explanation for the low temperature threshold for c-BN formation may have to do with the stability of c-BN under ion bombardment. Ullmann, Baglin, and Kellock (1998) studied the effects of 1.1 MeV Xe ion bombardment on cubic boron nitride films at room temperature. They found that for a fluence of Xe ions resulting in about 2 dpa for boron and nitrogen atoms in the film, the cubic phase was destroyed, and the film converted back into sp^2-bonded material. With typical c-BN film

growth conditions, the boron and nitrogen atoms in a growing film are subjected to roughly 5 dpa (Sene et al. 1996). Therefore it may be possible that the low temperature threshold for c-BN deposition corresponds to an activation energy threshold for an ion damage healing process in the c-BN crystal. Studies of the temperature dependence of keV ion damage in c-BN could be carried out at Argonne national labs and would clarify this point.

Finally, as pointed out to me by Dr. Mark Kirk, other factors such as the total recoil energy transfer rate per unit volume of the film may play critical roles as well. Also, Erman Bengu has noted that the formation of extended defect structures could be important in cubic boron nitride film growth and should be investigated. Energy transfer rate issues are currently being explored through TRIM ion bombardment simulations and theoretical scattering calculations. This is only an initial step as TRIM calculations involve a number of approximations and must be viewed with some caution for incident ion energies in the sub-keV energy range. A more accurate approach would involve the use of a sophisticated simulation package such as MARLOWE which takes into account the crystal structure of the target material. However, MARLOWE calculations are complicated and involved, and it is likely that a startup time of several weeks would have to be invested before any useful results were obtained. The investigation of the role of extended defect structures as suggested by Erman Bengu would also require extensive theoretical modeling work. Information could be obtained possibly through molecular dynamics simulations or through first-principles total energy calculations for

proposed defect structures. While these calculations would again require a significant setup effort, they could offer some important insight into processes which are currently only poorly understood.

REFERENCES

Abukawa, T., M. Sasaki, F. Hisamatsu, T. Goto, T. Kinoshita, A. Kakizaki, and S. Kono. 1995. Surface electronic structure of a single-domain Si(111)4x1-In surface: a synchrotron radiation photoemission study. *Surf. Sci.* 325: 33-44.

Abukawa, T., M. Sasaki, F. Hisamatsu, M. Nakamura, T. Kinoshita, A. Kakizaki, T. Goto, and S. Kono. 1996. Core-level photoemission study of the Si(111)4x1-In Surface. *J. Elec. Spect. Rel. Phenom.* 80: 233-236.

Allen, S. M. and E. L. Hall. 1982. Foil thickness measurements from convergent-beam diffraction patterns: an experimental assessment of errors. *Phil. Mag. A* 46: 243-253.

An, K. S., R. J. Park, J. S. Kim, C. Y. Park, C. Y. Kim, J. W. Chung, T. Abukawa, S. Kono, T. Kinoshita, A. Kakizaki, and T. Ishii. 1995. Mg-induced Si(111)3x1 structure studied by photoelectron spectroscopy. *Surf. Sci.* 337: L789-L794.

Ballal, A. K., L. Salamanca-Riba, C.A. Taylor II, and G.L. Doll. 1993. Structural characterization of preferentially oriented cubic BN films grown on Si (001) substrates. *Thin Solid Films* 224: 46-51.

Banhart, F., M. Zwanger, and H. J. Muhr. 1994. The formation of curled concentric-shell clusters in boron-nitride under electron-irradiation. *Chem. Phys. Lett.* 231: 98-104.

Banhart, F. and P. M. Ajayan. 1996. Carbon onions as nanoscopic pressure cells for diamond formation. *Nature* 382: 433-435.

Bertucci, M., G. Le Lay, M. Manneville, and R. Kern. 1979. Desorption kineteics of condensed phases. *Surf. Sci.* 85: 471-492.

Bevington, P. R. and D. K. Robinson. 1992. *Data reduction and error analysis for the physical sciences*. New York: McGraw-Hill, Inc.

Bouchier, D., G. Sene, M. A. Djouadi, P. Moller. 1994. Effect of noble gas ions on the synthesis of c-BN by ion beam assisted deposition. *Nucl. Instrum. Meth. B* 89: 369-372.

Boulanger, L., B. Andriot, M. Cauchetier, and F. Willaime. 1995. Concentric shelled and plate-like graphitic boron-nitride nanoparticles produced by CO_2-laser pyrolysis. *Chem. Phys. Lett.* 234: 227-232.

Bundy, F. P., and R. H. Wentorf. 1965. Direct transformation of hexagonal boron nitride to denser forms. *J. Chem. Phys.* 38: 1144-1149.

Cardillo, M. J. and G. E. Becker. 1978. Diffraction of He atoms at a Si(100) surface. *Phys. Rev. Lett.* 40: 1148-1151.

Cardinale, G. F., P. B. Mirkarimi, K. F. McCary, E. J. Klaus, D. L. Medlin, W. M. Clift, and D. G. Howitt. 1994. Effects of ambient conditions on the adhesion of cubic boron nitride films on silicon substrates. *Thin Solid Films* 253: 130-135.

Cardinale, G. F., D. G. Howitt, K. F. McCarty, D. L. Medlin, P. B. Mirkarimi, and N. R. Moody. 1996. Analysis of residual stress in cubic boron nitride thin films using micromachined cantilever beams. *Diam. and Rel. Mat.* 5: 1295-1302.

Cardinale, G. F., D. L. Medlin, P. B. Mirkarimi, K. F. McCarty, and D. G. Howitt. 1997. Orientation-dependence of elastic strain energy in hexagonal and cubic boron nitride layers in energetically deposited BN films. *J. Vac. Sci. Technol. A* 15: 196-200.

Carpinelli, J. M. and H. H. Weitering. 1995. Scanning tunneling microscopy study of the metal-induced Si(111)3x1 reconstruction: evidence for dimerized chain formation. *Surf. Sci.* 331-333: 1015-1021.

Carpinelli, J. M. and H. H. Weitering. 1996. Low-temperature reconstruction pathway to the Si(111)($\sqrt{3}$x$\sqrt{3}$)R30°-Ag interface. *Phys. Rev. B* 53: 12651-12654.

Chadi, D. J. 1979. Atomic and electronic structures of reconstructed Si(100) surfaces. *Phys. Rev. Lett.* 43: 43-47.

Cochran, W. 1955. Relations between the phases of structure factors. *Acta Cryst.* 8: 473-478.

Collazo-Davila, C., E. Landree, D. Grozea, G. Jayaram, R. Plass, P. C. Stair, and L. D. Marks. 1995. Design and initial performance of an ultrahigh vacuum sample preparation evaluation analysis and reaction (SPEAR) system. *JMSA* 1: 267-279.

Collazo-Davila, C., D. Grozea, E. Landree, and L. D. Marks. 1997. Transmission electron diffraction determination of the Ge(001)-(2x1) surface structure. *Surf. Sci.* 375: 293-301.

Collazo-Davila, C., L. D. Marks, K. Nishii, and Y. Tnaishiro. 1997. Atomic structure of the In on Si(111)(4x1) surface. *Surf. Rev. Lett.* 4: 65-70.

Collazo-Davila, C., D. Grozea, and L. D. Marks. 1998. Determination and refinement of the Ag/Si(111)-(3x1) surface structure. *Phys. Rev. Lett.* 80: 1678-1681.

Comello, V. 1998. Semiconductor industry faces measurement challenge. *R&D Mag.* 40: 20-24.

Cornelison, D. M., M. S. Worthington, and I. S. T. Tsong. 1991. Si(111)-(4x1)In surface reconstruction studied by impact-collision ion-scattering spectrometry. *Phys. Rev. B* 43: 4051-4056.

Cover, T. M. and J. A. Thomas. 1991. *Elements of information theory*. New York: John Wiley and Sons.

Culbertson, R. J., Y. Kuk, and L. C. Feldman. 1986. Subsurface strain in the Ge(001) and Ge(111) surfaces and comparison to silicon. *Surf. Sci.* 167: 127-140.

Dabrowski, J. and M. Scheffler. 1992. Self-consistent study of the electronic and structural properties of the clean Si(001)(2x1) surface. *App. Surf. Sci.* 56-58: 15-19.

Ding, Y. G., C. T. Chan, and K. M. Ho. 1991. Structure of the ($\sqrt{3}$x$\sqrt{3}$)R30°-Ag/Si(111) surface from first principles calculations. *Phys. Rev. Lett.* 67: 1454-1457.

Doll, G. L., J. A. Sell, C. A. Taylor II, and R. Clarke. 1991. Growth and characterization of epitaxial cubic boron nitride films on silicon. *Phys. Rev. B* 43: 6816-6819.

Dworschak, W., K. Jung, and H. Ehrhardt. 1995. Growth mechanism of cubic boron nitride in a r.f. glow discharge. *Thin Solid Films* 254: 65-74.

Erwin, S. C. 1995. New structural model for the alkali-induced Si(111)-(3x1) reconstruction from first principles. *Phys. Rev. Lett.* 75: 1973-1976.

Esch, S., M. Hohage, T. Michely, and G. Comsa. 1994. Origin of oxygen induced layer-by-layer growth in homoepitaxy on Pt(111). *Phys. Rev. Lett.* 72: 518-521.

Falta, J., A. Hille, D. Novikov, G. Materlik, L. Seehofer, G. Falkenberg, and R. L. Johnson. 1995. Domain wall structure of Si(111)($\sqrt{3}$x$\sqrt{3}$)R30°-Au. *Surf. Sci.* 330: L673-L677.

Fan, W. C. and A. Ignatiev. 1990. Metal-adsorbate-induced Si(111)-(1x3) reconstruction. *Phys. Rev. B* 41: 3592-3595.

Feidenhans'l, R. 1989. Surface-structure determination by x-ray-diffraction. *Surf. Sci. Rep.* 10: 105-188.

Ferrer, S., X. Torrelles, V. H. Etgens, H. A. van der Vegt, and P. Fajardo. 1995. Atomic structure of the c(4x2) surface reconstruction of Ge(001) as determined by X-ray diffraction. *Phys. Rev. Lett.* 75: 1771-1774.

Finney, M. S., C. Norris, P. B. Howes, M. A. James, J. E. Macdonald, A. D. Johnson, and E. Vlieg. 1994. The growth and atomic structure of the Si(111)-indium interface studied by surface x-ray diffraction. *Physica B* 198: 246-248.

Friedmann, T. A., P. B. Mirkarimi, D. L. Medlin, K. F. McCarty, E. J. Klaus, D. R. Boehme, H. A. Johnsen, M. J. Mills, D. K. Ottesen, and J. C. Barbour. 1994. Ion-assisted pulsed laser deposition of cubic boron nitride films. *J. Appl. Phys.* 76: 3088-3101.

Fukuda, T. 1994. Determination of silver coverage on Si(111)3x1(6x1)-Ag surfaces. *Phys. Rev. B* 50: 1969-1972.

Gerchberg, R. W., and W. O. Saxton. 1972. A practical algorithm for the determination of phase from image and diffraction plane pictures. *Optik* 35: 237-246.

Gilmore, C. J., L. D. Marks, D. Grozea, C. Collazo, E. Landree, and R. D. Twesten. 1997. Direct solutions of the Si(111) 7x7 structure. *Surf. Sci.* 381: 77-91.

Göthelid, M., M. Hammar, U. O. Karlsson, C. Wigren, and G. Le Lay. 1995. Structural and electronic evolution on the Ge(111)-Ag surface. *Phys. Rev. B* 52: 14104-14110.

Hahn, J., F. Richter, R. Pintaske, M. Roder, E. Schneider, and T. Welzel. 1997. Formation of c-BN thin films under reduced ion impact. *Surf. & Coat. Technol.* 92: 129-134.

Hammar, M., M. Göthelid, U. O. Karlsson, and S. A. Flodström. 1993. Initial growth of silver on Ge(111) studied by scanning tunneling microscopy. *Phys. Rev. B* 47: 15669-15674.

Hammers, R. J., R. M. Tromp, and J. E. Demuth. 1986. Scanning tunneling microscopy of Si(001). *Phys. Rev. B* 34: 5343-5357.

Harker, D. and Kasper, J. S. 1948. Phases of Fourier coefficients directly from crystal diffraction data. *Acta Cryst.* 1: 70-75.

Hashizume, T., M. Katayama, D. Jeon, M. Aono, and T. Sakurai. 1993. The absolute coverage of K on the Si(111)-3x1-K surface. *Jpn. J. Appl. Phys.* 32: L1263-L1265.

Higashiyama, K., S. Kono, and T. Sagawa. 1986. Structural disorder of Si(111)$\sqrt{3}$x$\sqrt{3}$-Au surface studied by LEED. *Jpn. J. Appl. Phys.* 25: L117-L120.

Hill, I. G. and A. B. McLean. 1997. Metallicity of In Chains on Si(111). *Phys. Rev. B* 56: 15725-15728.

Hofsäss, H., H. Feldermann, M. Sebastian, and C. Ronning. 1997. Thresholds for the phase formation of cubic boron nitride thin films. *Phys. Rev. B* 55: 13230-13233.

Hofsäss, H., H. Feldermann, R. Merk, M. Sebastian, and C. Ronning. 1998. Cylindrical spike model for the formation of diamondlike thin films by ion depostion. *Appl. Phys. A* 66: 153-181.

Horiuchi, S., L. L. He, and M. Akaishi. 1995. Semispiral structure of turbostratic boron nitride formed under high pressure and high temperature. *Jpn. J. Appl. Phys.* 34: L1612-L1615.

Huang, H., H. Over, S. Y. Tong, J. Quinn, and F. Jona. 1994. Atomic geometry of Ge(111) $\sqrt{3}$x$\sqrt{3}$ R30°-Ag determined by low-energy electron diffraction. *Phys. Rev. B* 49: 13483-13487.

Ichiki, T., T. Momose, and T. Yoshida. 1994. Effects of the substrate bias on the formation of cubic boron nitride by inductively coupled plasma enhanced chemical vapor deposition. *J. Appl. Phys.* 75: 1330-1334.

Ihm, J., D. H. Lee, J. D. Joannopoulos, and J .J. Xiong. 1983. Structural phase diagrams for the surface of a solid: a total-energy, renormalization-group approach.. *Phys. Rev. Lett.* 51: 1872-1875.

Ikeda, T., Y. Kawate, and Y. Hirai. 1990. Formation of cubic boron nitride films by arc-like plasma-enhanced ion plating method. *J. Vac. Sci. Tech. A* 8: 3168-3174.

Ikeda, T. 1992. Cubic boron nitride films synthesized by low-energy ion-beam-enhanced vapor deposition. *Appl. Phys. Lett.* 61: 786-788.

Jayaram, G., R. Plass, and L. D. Marks. 1995. UHV-HREM and diffraction of surfaces. *Interface Sci.* 2: 379-395.

Jeong, S. and M. Kang. 1996. Buckled reconstruction of the alkali-metal (Na, K)-adsorbed Si(111)-(3x1) surfaces. *Phys. Rev. B* 54: 8196-8201.

Johansson, M. P., L. Hultman, S. Daaud, K. Bewilogua, H. Luthje, A. Schutze, S. Kouptsidis, and G. S. A. M. Theunissen. 1996. Microstructure of BN:C films deposited on Si substrates by reactive sputtering from a B_4C target. *Thin Solid Films* 287: 193-201.

Kester, D. J. and R. Messier. 1992. Phase control of cubic boron nitride thin films. *J. Appl. Phys.* 72: 504-513.

Kester, D. J., K. S. Ailey, R. F. Davis, and K. L. More. 1993. Phase evolution in boron nitride thin films. *J. Mat. Res.* 8: 1213-1216.

Kester, D. J., K. S. Ailey, D. J. Lichtenwalner, and R. F. Davis. 1994. Growth and characterization of cubic boron nitride thin films. *J. Vac. Sci. Technol. A* 12: 3074-3081.

Kevan, S. D. and N. G. Stoffel. 1984. Metal-insulator transition on the Ge(001) surface. *Phys. Rev. Lett.* 53: 702-705.

Kevan, S. D. 1985. Surface states and reconstruction on Ge(001). *Phys. Rev. B* 32: 2344-2350.

Kidner, S., C. A. Taylor II, and R. Clarke. 1994. Low energy kinetic threshold in the growth of cubic boron nitride films. *Appl. Phys. Lett.* 64: 1859-1861.

Kinchin, G. H., R. S. Pease. 1955. The displacement of atoms in solids by radiation. *Rep. Prog. Phys.* 18: 1-51.

Koike, J., D. M. Parkin, and T. E. Mitchell. 1992. Displacement threshold energy for type IIa diamond. *Appl. Phys. Lett.* 60: 1450-1452.

Kraft, J., M. G. Ramsey, and F. P. Netzer. 1997. Surface Reconstructions of In on Si(111). *Phys. Rev. B* 55: 5384-5393.

Krüger, P. and J. Pollmann. 1995. Dimer reconstruction of diamond, Si, and Ge (001) surfaces. *Phys. Rev. Lett.* 74: 1155-1158.

Kubby, J. A., J. E. Griffith, R. S. Becker, and J. S Vickers. 1987. Tunneling microscopy of Ge(001). *Phys. Rev. B* 36: 6079-6093.

Kulisch, W. and S. Reinke. 1997. Modeling of c-BN Thin Film Deposition. *Diam. Films and Tech.* 7: 105-138.

Lambert, W. R., P. L. Trevor, M. J. Cardillo, A. Sakai, and D. R. Hamann. 1987. Surface structure of Ge(100) studied by He diffraction. *Phys. Rev. B* 35: 8055-8064.

Landemark, E., C. J. Karlsson, L. S. O. Johansson, and R. I. G. Uhrberg. 1994. Electronic structure of clean and hydrogen-chemisorbed Ge(001) surfaces studied by photoelectron spectroscopy. *Phys. Rev. B* 49: 16523-16533.

Lander, J. J., and J. Morrison. 1962. Low-energy electron diffraction study of silicon surface structures. *J. Chem. Phys.* 37: 729-746.

Landree, E., C. Collazo-Davila, and L. D. Marks. 1997. Multi-solution genetic algorithm approach to surface structure determination using direct methods. *Acta Cryst. B* 53: 916-922.

Le Lay,G. 1983. Physics and electronics of the noble-metal/elemental-semiconductor interface formation: a status report. *Surf. Sci.* 132: 169-204.

Le Lay, G., V. Y. Aristov, L.Seehofer, T. Buslaps, R. L. Johnson, M. Göthelid, M. Hammar, U. O. Karlsson, S. A. Flodström, R. Feidenhans'l, M. Nielsen, E. Findeisen, and R. I. G. Uhrberg. 1994. STM and synchrotron radiation studies of "prototypical" metal/semiconductor systems. *Surf. Sci.* 307-309: 280-294.

Levi, A. and H. Stark. 1984. Image restoration by the method of generalized projections with application to restoration form magnitude. *J. Opt. Soc. Am. A* 1: 932-943.

Lifshitz, Y., S. R. Kasi, J. W. Rabalais, and W. Eckstein. 1990. Subplantation model for film growth from hyperthermal species. *Phys. Rev. B* 41: 10468-10480.

Lottermoser, L., E. Landemark, D. M. Smilgies, M. Nielsen, R. Feidenhans'l, G. Falkenberg, R. L. Johnson, M. Gierer, A. P. Seitsonen, H. Kleine, H. Bludau, H. Over, S. K. Kim, and F. Jona. 1998. New bonding configuration on Si(111) and Ge(111) surfaces induced by the adsorption of alkali metals. *Phys. Rev. Lett.* 80: 3980-3983.

Lucas, C. A., C. S. Dower, D. F. McMorrow, G. C. L. Wong, F. J. Lamelas, and P. H. Fuoss. 1993. Order-disorder c(4x2)-(2x1) transition on Ge(001): an in situ x-ray scattering study. *Phys. Rev. B* 47: 10375-10382.

Madan, A., X. Chu, and S. A. Barnett. 1996. Growth and characterization of epitaxial Mo/NbN superlattices. *Appl. Phys. Lett.* 68: 2198-2200.

Malis, T., S. C. Cheng, and R. F. Egerton. 1988. EELS log-ratio technique for specimen-thickness measurement in the TEM. *J. Electron Microscopy Technique* 8: 193-200.

Marks, L. D. and R. Plass. 1995. Atomic structure of Si(111)-(5x2)-Au from high reslution electron microscopy and heavy-atom holography. *Phys. Rev. Lett.* 75: 2172-2175.

Marks, L. D., R. Plass, and D. Dorset. 1997. Imaging surface structures by direct phasing. *Surf. Rev. and Lett.* 4: 1-8.

Marks, L. D., and E. Landree. 1998. A minimum entropy algorithm for surface phasing problems. *Acta Cryst. A*, in press.

Marks, L. D., E. Bengu, C. Collazo-Davila, D. Grozea, E. Landree, C. Leslie, and W. Sinkler. 1998. Direct methods for surfaces. *Surf. Rev. and Lett.*, in press.

Marshall, S. 1997. MEMS technologies -- on the brink of maturity?. *R&D Mag.* 39: 20-22.

McCarty, K. F. and D. L. Medlin. 1997. How plastic deformation can produce texture in graphitic films of boron nitride, carbon nitride, and carbon. *Diam. and Rel. Mat.* 6: 1219-1225.

Mc Carty, K. F., P. B. Mirkarimi, D. L. Medlin, T. A. Friedmann, and J. C. Barbour. 1996. On the low-temperature threshold for cubic boron nitride formation in energetic film depostion. *Diam. and Rel. Mat.* 5: 1519-1526.

McKenzie, D.R. 1993. Generation and applications of compressive stress induced by low energy ion beam bombardment. *J. Vac. Sci. Tech. B* 11: 1928-1935.

McKenzie, D. R., W. D. McFall, W. G. Sainty, C. A. Davis, and R. E. Collins. 1993. Compressive stress induced formation of cubic boron nitride. *Diam. and Rel. Mat.* 2: 970-976.

McKenzie, D. R., W. D. McFall, H. Smith, B. Higgins, R. W. Boswell, A. Durandet, B. W. James, and I. S. Falconer. 1995. High pressure phases produced by low energy ion implantation with reference to cubic boron nitride. *Nucl. Instrum. Meth. B* 106: 90-95.

McKinley, W. A., H. Feshbach. 1948. The coulomb scattering of relativistic electrons by nuclei. *Phys. Rev.* 74: 1759-1763.

Medlin, D. L., T. A. Friedmann, P. B. Mirkarimi, M. J. Mills, and K. F. McCarty. 1994. Evidence for rhombohedral boron nitride in cubic boron nitride films grown by ion-assisted deposition. *Phys. Rev. B* 50: 7884-7887.

Medlin, D. L., T. A. Friedmann, R. B. Mirkarimi, G. F. Cardinale, and K. F. McCarty. 1996. Crystallographic texture in cubic boron nitride thin films. *J. Appl. Phys.* 79: 3567-3571.

Meilunas, R. J., R. P. H. Chang, S. Liu, and M. M. Kappes. 1991. Nucleation of diamond films on surfaces using carbon clusters. *Appl. Phys. Lett.* 59: 3461-3463.

Mieno, M. and T. Yoshida. 1990. Preparation of cubic boron nitride films by RF sputtering. *Jap. J. Appl. Phys.* 29: L1175-L1177.

Mirkarimi, P. B., K. F. McCarty, D. L. Medlin, W. G. Wolfer, T. A. Friedmann, E. J. Klaus, G. F. Cardinale, and D. G. Howitt. 1994. On the role of ions in the formation of cubic boron nitride films by ion-assisted deposition. *J. Mater. Res.* 9: 2925-2938.

Mirkarimi, P. B., D. L. Medlin, K. F. McCarty, and J. C. Barbour. 1995. Growth of cubic BN films on β-SiC by ion-assisted pulsed laser deposition. *Appl. Phys. Lett.* 66: 2813-2815.

Mirkarimi, P. B., D. L. Medlin, K. F. McCarty, D. C. Dibble, W. M. Clift, J. A. Knapp, and J. C. Barbour. 1997. The synthesis, characterization, and mechanical properties of thick, ultrahard cubic boron nitride films deposited by ion-assisted sputtering. *J. Appl. Phys.* 82: 1617-1625.

Mirkarimi, P. B., K. F. McCarty, and D. L. Medlin. 1997. Review of advances in cubic boron nitride film synthesis. *Mat. Sci. and Eng.* R21: 47-100.

Monch, W. 1995. *Semiconductor Surfaces and Interfaces*. Berlin: Springer-Verlag.
Mott, N. F. 1929. The scattering of fast electrons by atomic nuclei. *R. Soc. London A* 124: 425-442.

Muscat, A. J., A. Rjeb, and D. Roy. 1994. Oxidation of Si(111)7x7 using alkali metal atoms: evidence for local promotion mechanisms. *Surf. Sci. Lett.* 302: L256-L262.

Nakamura, N., K. Anno, and S. Kono. 1991. Structure analysis of the single-domain Si(111)4x1-In surface by μ-probe Auger electron diffraction and μ-probe reflection high energy electron diffraction. *Surf. Sci.* 256: 129-134.

Nakano, S. and O. Fukunaga. 1993. New scope of high pressure-high temperature synthesis of cubic boron nitride. *Diam. and Rel. Mat.* 2: 1409-1413.

Needels, M., M. C. Payne, and J. D. Joannopoulos. 1987. Ab initio molecular dynamics on the Ge(100) surface. *Phys. Rev. Lett.* 58: 1765-1768.

Needels, M., M. C. Payne, and J. D. Joannopoulos. 1988. High-order reconstructions of the Ge(100) surface. *Phys. Rev. B* 38: 5543-5546.

Nicholls, J. M., P. Martensson, and G. V. Hansson. 1985. Surface states on Si(111)$\sqrt{3}$x$\sqrt{3}$-In: experiment and theory. *Phys. Rev. B* 32: 1333-1335.

Nogami, J., S. Park, and C. F. Quate. 1987. Indium-induced reconstructions of the Si(111) surface studied by scanning tunneling microscopy. *Phys. Rev. B* 36: 6221-6224.

Nogami, J., A. A. Baski, and C. F. Quate. 1990. $\sqrt{3}$x$\sqrt{3} \rightarrow$ 6x6 phase transition on the Au/Si(111) surface. *Phys. Rev. Lett.* 65: 1611-1614.

Northrup, J. E. 1993. Electronic structure of Si(100)c(4x2) calculated within the GW approximation. *Phys. Rev. B* 47: 10032-10035.

Ohnishi, H., Y. Yamamoto, I. Katayama, Y. Ohba, and K. Oura. 1994. Scanning tunneling microscope observations of Si(111)3x1-Ag and 6x1-Ag structures. *Appl. Surf. Sci.* 82/83: 444-448.

Okamoto, M., H. Yokoyama, and Y. Osada. 1990. Formation of cubic boron nitride film on Si with boron buffer layers. *Jap. J. Appl. Phys.* 29: 930-933.

Okuda, T., H. Shigeoka, H. Daimon, S. Suga, T. Kinoshita, and A. Kakizaki. 1994. Surface and bulk core level shifts of the Si(111)3x1-Na and Si(111) δ7x7-Na surfaces. *Surf. Sci* 321: 105-110.

Okuda, T., K. Sakamoto, H. Nishimoto, H. Daimon, S. Suga, T. Kinoshita, and A. Kakizaki. 1997. Angle-resolved photoelectron spectroscopy of the Si(111)3x1-Na surface. *Phys. Rev. B* 55: 6762-6765.

Oppo, S., V. Fiorentini, and M. Scheffler. 1993. Theory of adsorption and surfactant effect of Sb on Ag(111). *Phys. Rev. Lett.* 71: 2437-2440.

Ozawa, S., A. Yamanaka, K. Kobayashi, Y. Tanishiro, and K. Yagi. 1990. A new technique to produce clean and thin silicon films in situ in a UHV electron-microscope for TEM-TED studies of surfaces. *Jpn. J. Appl. Phys.* 29: L655-L658.

Paggel, J. J., G. Neuhold, H. Haak, and K. Horn. 1995. Scanning-tunneling-microscopy and photoemission study of an alkali-metal-induced structural phase transition: Si(111)-(7x7) into Si(111)-Na(3x1). *Phys. Rev. B* 52: 5813-5823.

Pandey, K. C. 1981. New π-bonded chain model for Si(111)-(2x1) surface. *Phys. Rev. Lett.* 47: 1913-1917.

Park, C. Y., K. S. An, J. S. Kim, R. J. Park, J. W. Chung, T. Kinoshita, A. Kakizaki, and T. Ishii. 1995. Photoemission study of the Si(111)6x1-Cs surface. *Phys. Rev. B* 52: 8198-8204.

Park, K. S., D. Y. Lee, K. J. Kim, and D. W. Moon. 1997. Observation of a hexagonal BN surface layer on the cubic BN film grown by dual ion beam sputter deposition. *Appl. Phys. Lett.* 70: 315-317.

Park, S., J. Nogami, and C. F. Quate. 1988. Metal-induced reconstructions of the silicon(111) surface. *J. Microscopy* 152: 727-734.

Peng, L. M., G. Ren, S. L. Dudarev, and M J. Whelan. 1996. Debye-Waller factors and absorptive scattering factors of elemental crystals. *Acta Cryst. A* 52: 456-470.

Phani, A. R., S. Roy, and V. J. Rao. 1995. Growth of boron nitride thin films by metal-organic chemical vapour deposition. *Thin Solid Films* 258: 21-25.

Plass, R. and L. D. Marks. 1997. Submonolayer Au on Si(111) phase diagram. *Surf. Sci.* 380: 497-506.

Pollmann, J., P. Krüger, and A. Mazur. 1987. Self-consistent electronic structure of semi-infinite Si(001) (2x1) and Ge(001) (2x1) with model calculations for scanning tunneling microscopy. *J. Vac. Sci. Technol. B* 5: 945-952.

Pryor, R. W., X. L. Wu, K. R. Padmanabhan, S. Villanueva, and R. L. Thomas. 1994. Characterization of laser-ablated boron nitride thin films on silicon. *Thin Solid Films* 253: 243-246.

Qin, L. C. and S. Iijima. 1996. Onion-like graphitic particles produced from diamond. *Chem. Phys. Lett.* 262: 252-258.

Quinn, J. and F. Jona. 1991. New results on the reaction of Si{111} with Mg. *Surf. Sci. Lett.* 249: L307-L311.

Reinke, S., M. Kuhr, W. Kulisch, and R. Kassing. 1995. Recent results in cubic boron nitride deposition in light of the sputter model. *Diam. and Rel. Mat.* 4: 272-283.

Rossmann, R., H. L. Meyerheim, V. Jahns, J. Wever, W. Moritz, D. Wolf, D. Dornisch, and H. Schulz. 1992. The Ge(001) (2x1) reconstruction: asymmetric dimers and multilayer relaxation observed by grazing incidence X-ray diffraction. *Surf. Sci.* 279: 199-209.

Sachdev, H., R. Haubner, H. Hoth, and B. Lux. 1997. Investigation of the c-BN/h-BN phase transformation at normal pressure. *Diam. and Rel. Mat.* 6: 286-292.

Saitoh, H. and W. A. Yarbrough. 1991. Growth of cubic boron nitride on diamond particles by microwave plasma enhanced chemical vapor deposition. *Appl. Phys. Lett.* 58: 2482-2484.

Sakamoto, K., T. Okuda, H. Nishimoto, H. Daimon, S. Suga, T. Kinoshita, and A. Kakizaki. 1994. Photoemission study of the Si(111)3x1-K surface. *Phys. Rev. B* 50: 1725-1732.

Saranin, A. A., A. V. Zotov, K. V. Ignatovich, V. G. Lifshits, T. Numata, O. Kubo, H. Tani, M. Katayama, and K Oura. 1997. Structural Model for the Si(111)-4x1-In Reconstruction. *Phys. Rev. B* 56: 1017-1020.

Sayre, D. 1952. The squaring method: a new method for phase determination. *Acta Cryst.* 5: 60-65.

Schlier, R. E. and H. E. Farnsworth. 1959. Structure and adsorption characteristics of clean surfaces of germanium and silicon. *J. Chem. Phys.* 30: 917-926.

Seitz, F. and J. S. Koehler. 1956. Displacement of atoms during irradiation. *Solid State Phys.* 2: 305-448.

Seiwatz, R. 1964. Possible structures for clean, annealed surfaces of germanium and silicon. *Surf. Sci.* 2: 473-483.

Sene, G., D. Bouchier, S. Ilias, M. A. Djouadi, J. Pascallon, V. Stambouli, P. Moller, and G. Hug. 1996. Correlation between microstructure and collisional effects in cubic boron nitride synthesized using IBAD. *Diam. and Rel. Mat.* 5: 530-534.

Shinn, M. and S. A. Barnett. 1994. Effect of superlattice layer elastic moduli on hardness. *Appl. Phys. Lett.* 64: 61-63.

Sokolowski, M.1979. Deposition of wurtzite type bron nitride layers by reactive pulse plasma crystallization. *J. Cryst. Grwth.* 46: 136-138.

Solozhenko, V. L. 1993. Thermodynamics of dense boron nitride modifications and a new phase P,T diagram for BN. *Termochimica Acta* 218: 221-227.

Song, Z., F. Zhang, Y. Guo, and G. Chen. 1994. Textured growth of cubic boron nitride film on nickel substrates. *Appl. Phys. Lett.* 65: 2669-2671.

Spence, D. J. and S. P. Tear. 1998. STM studies of submonolayer coverages of Ag on Ge(111). *Surf. Sci.* 398: 91-104.

Spiess, L., A. J. Freeman, and P. Soukiassian. 1994. Ge(100) 2x1 and c(4x2) surface reconstructions studied by ab initio total-energy molecular-force calculations. *Phys. Rev. B* 50: 2249-2258.

Steffen, H. J., D. Marton, and J. W. Rabalais. 1992. Displacement energy threshold for Ne^+ irradiation of graphite. *Phys. Rev. Lett.* 68: 1726-1729.

Stevens, J. L., M. S. Worthington, and I. S. T. Tsong. 1993. 4x1 reconstruction of indium deposited on vicinal Si(111) surfaces. *Phys. Rev. B* 47: 1453-1459.

Takahashi, S., Y. Tanishiro, and K. Takayanagi. 1991. Short range orders of an adsorbed layer: gold on the Si(111)7x7 surface. *Surf. Sci.* 242: 73-80.

Takahashi, T. and S. Nakatani. 1993. Refinement of the Si(111)√3x√3-Ag structure by surface x-ray-diffraction. *Surf. Sci.* 282: 17-32.

Takami, T., D. Fukushi, T. Nakayama, M. Uda, and M. Aono. 1994. Structural correlation among differnet phases in the initial stage of epitaxial growth of Au on Si(111). *Jpn. J. Appl. Phys.* 33: 3688-3685.

Takayanagi, K., K. Kobayashi, K. Yagi, and G. Honjo. 1978. *J. Phys. E* 11: 441.

Takayanagi, K., Y. Tanishiro, S. Takahashi, and M. Takahashi. 1985. Structure analysis of Si(111)-7x7 reconstructed surface by transmission electron diffraction. *Surf. Sci.* 164: 367-392.

Tanishiro, Y., K. Kaneko, H. Minoda, K. Yagi, T. Sueyoshi, T. Sato, and M. Iwatsuki. 1996. Dynamic observation of In adsorption on Si(111) surfaces by UHV high-temperature scanning tunneling microscopy. *Surf. Sci.* 357-358: 407-413.

Tikhov, M., L. Surnev, and M. Kiskinova. 1991. Na-induced (7x7)-to-(3x1) structural transformation on a Si(111)7x7 surface and the resulting passivation of the surface towards interaction with oxygen. *Phys. Rev. B* 44: 3222-3225.

Torrelles, X., H. A. van der Vegt, V. H. Etgens, P. Fajardo, J. Alvarez, and S. Ferrer. 1996. The structure of the Ge(001)-(2x1) reconstruction investigated with x-ray diffraction. *Surf. Sci.* 364: 242-252.

Ugarte, D. 1992. Curling and closure of graphitic networks under electron-beam irradiation. *Nature* 359: 707-709.

Ullmann, J., J. E. E. Baglin, and A. J. Kellock. 1998. Effects of MeV ion irradiation of thin cubic boron nitride films. *J. Appl. Phys.* 83: 2980-2987.

Vel, L., G. Demazeau, and J. Etourneau. 1991. Cubic boron nitride: synthesis, physicochemical properties and applications. *Mat. Sci. and Eng. B* 10: 149-164.

Wan, K. J., X. F. Lin, and J. Nogami. 1992. Comparison of the 3x1 reconstructions of the Si(111) surface induced by Li and Ag. *Phys. Rev. B* 46: 13635-13638.

Wang, J., T. A. Arias, and J. D. Joannopoulos. 1993. Dimer vacancies and dimer vacancy complexes on the Si(100) surface. *Phys.Rev. B* 47: 10497-10508.

Weitering, H. H., N. J. DiNardo, R. Pérez-Sandoz, J. Chen, and E. J. Mele. 1994. Structural model for the metal-induced Si(111)3x1 reconstruction. *Phys. Rev. B* 49: 16837-16840.

Weitering, H. H., X. Shi, and S. C. Erwin. 1996. Band dispersions of the π-bonded-chain reconstruction of Si(111)3x1-Li: a critical evaluation of theory and experiment. *Phys. Rev. B* 54: 10585-10592.

Weitering, H. H. 1996. New barium-induced surface reconstructions on Si(111). *Surf. Sci.* 355: L271-L277.

Weitering, H. H. and J. M. Carpinelli. 1997. Eelectronic properties of the Ag/Ge(111) interface. *Surf. Sci.* 384: 240-253.

Weng-Sieh, Z., K. Cherrey, M. G. Chopra, X. Blase, Y. Miyamoto, A. Rubio, M. L. Cohen, S. G. Louie, A. Zettl, and R. Gronsky. 1995. Synthesis of $B_xC_yN_z$ Nanotubes. *Phys. Rev. B* 51: 11229-11232.

Wentorf, R. H. 1957. Cubic form of boron nitride. *J. Chem. Phys.* 26: 956.

Wentorf, R. H. 1961. Synthesis of the cubic form of boron nitride. *J. Chem. Phys.* 34: 809-812.

Widany, J., T. Frauenheim, and W. R. L. Lambrecht. 1996. Investigation of the stability of the hexagonal-cubic boron nitride prism interface. *J. Mater. Chem.* 6: 899-901.

Woicik, J. C., T. Kendelewicz, A. Herrera-Gomez, A. B. Andrews, Boong Soo Kim, P. L. Cowan, K. E. Miyano, C. E. Bouldin, B .A. Karlin, G. S. Herman, J. L. Erskine, P. Pianetta, and W. E. Spicer. 1993. Adatom location on the Si(111)7x7 and Si(111)$\sqrt{3}$x$\sqrt{3}$-In surfaces by the x-ray standing wave and photoemission techniques. *J. Vac. Sci. Technol. A* 11: 2359-2363.

Wong, G. C. L., C. A. Lucas, D. Loretto, A. P. Payne, and P. H. Fuoss. 1994. Parallel adatom chains on Si(111) - a chemisorption-induced surface reconstruction. *Phys. Rev. Lett.* 73: 991-994.

Wood, E. A. 1963. Vocabulary of surface crystallography. *J. Appl. Phys.* 35: 1306-1311.
Woolfson, M. M. 1961. *Direct methods in crystallography*. Oxford: Clarendon Press.

Xu, P., G. Jayaram, and L.D. Marks. 1994. Cross-correlation method for intensity measurement of transmission electron diffraction patterns. *Ultramicroscopy* 53: 15-18.

Yang, W. S., X. D. Wang, K.Cho, J. Kishimoto, S. Fukatsu, T. Hashizume, and T. Sakurai. 1994. Missing-dimer complexes and dimers on the Ge(001) surface. *Phys. Rev. B* 50: 2406-2408.

Yokoyama, H., M. Okamoto, and Y. Osaka. 1991. Effects of a negative self-bias on the growth of cubic boron nitride prepared by plasma chemical vapor deposition. *Jap. J. Appl. Phys*. 30: 344-348.

Youla, D. C. 1987. Mathematical theory of image restoration by the method of convex projections. In *Image recovery: theory and applications*, edited by H. Stark.. Orlando: Academic press, Inc. 29-76.

Yuhara, J., M. Inoue, and K. Morita. 1992. Commensurate-incommensurate phase transition between 6x6 and $\sqrt{3}x\sqrt{3}$ + satellite structures of the Au/Si(111) surface. *J. Vac. Sci. Techonol. A* 10: 3486-3492.

Zhou, W. L., Y. Ikuhara, and T. Suzuki. 1995. Orientational relationship between cubic boron nitride and hexagonal boron nitride in a thin film synthesized by ion plating. *Appl. Phys. Lett.* 67: 3551-3553.

Zitzlsperger, M., R. Honke, P. Pavone, and U. Schröder. 1997. Ab initio calculation of the structure, the electronic states and the phonon dispersion of the Si(111)-(2x1) surface. *Surf. Sci.* 377-379: 108-111.

APPENDIX A. DIFFRACTION INTENSITY MEASUREMENT ERRORS

In the TED intensity measurement process described in chapter 2, a single reflection, **h**, is likely to be measured several times on different negatives belonging to the through-exposure-time series. Given that the relative intensity scaling factors between the repeat measurements can be calculated as described in section 2.2, the next question becomes one of averaging the different measurements to arrive at one final value with an associated error estimate for the intensity of a given beam.

If the measured values actually corresponded to the number of electrons arriving during the exposure time, N^e, then random counting statistics would be directly applicable and the error for a single measurement would be $(N^e)^{1/2}$. I will denote this error for a single measurement by $\sigma_j(\mathbf{h})$, where j is used to index the picture from which the measurement was made, and **h** is the particular reflection being measured. With error estimates for individual measurements, averaging several different measurements for the same reflection would be a straight-forward application of the standard formula (Bevington and Robinson 1992, 59),

$$\bar{I}(\bar{h}) = \frac{\sum_j \left(I_j(\bar{h}) / \sigma_j^2(\bar{h}) \right)}{\sum_j \left(1 / \sigma_j^2(\bar{h}) \right)} \qquad (A.1)$$

where $I_j(\mathbf{h})$ is the measured intesity of the reflection, **h**, for picture number j, and the sums are taken over all pictures in which $I(\mathbf{h})$ was measured. The corresponding error for the averaged value would be (Bevington and Robinson 1992, 59),

$$\sigma[\bar{I}(\bar{h})] = \frac{1}{\sum_j \left(1 / \sigma_j^2(\bar{h}) \right)} \qquad (A.2)$$

However, the intensity values that are measured from the exposed negatives are proportional to N^e, not equal to it, and therefore it is not correct to directly equate $\sigma_j(\mathbf{h}) = [I_j(\mathbf{h})]^{1/2}$. Instead, $I_j(\mathbf{h})$ should be viewed as a function of $N^e(\mathbf{h})$ given by,

$$I_j(\bar{h}) = CN_j^e(\bar{h}) \qquad (A.3)$$

where C is the proportionality constant. Then by following the propagation of errors (Bevington and Robinson 1992, 38) one finds,

$$\sigma_j^2(\bar{h})_I = C^2 \sigma_j^2(\bar{h})_N \qquad (A.4)$$

Here the subscript "I" placed after $\sigma_j^2(\mathbf{h})$ is used to indicate that the units of the error estimate are the same as the intensity measurement units, $I_j(\mathbf{h})$. The term, $\sigma_j^2(\mathbf{h})_N$, represents an uncertainty directly as a number of electrons and so is not numerically equal to $\sigma_j^2(\mathbf{h})_I$. Substituting $\sigma_j^2(\mathbf{h})_N = N^e$ in equation A.4 and then using equation A.3 gives,

$$\sigma_j^2(\bar{h})_I = CI_j(\bar{h}) \qquad \text{(A.5)}$$

Equation A.5 shows the correct relationship between $I_j(\mathbf{h})$ and $\sigma_j^2(\mathbf{h})_I$. If one is to obtain an error estimate for an individual measurement by calculating $[I_j(\mathbf{h})]^{1/2}$, then the value of the constant, C, must be known first.

As mentioned in section 2.2, the uncertainty in individual measurements increases with increasing exposure times because of a stronger background relative to the optical density measurement window. This causes C to become a function of the picture number, with larger values of C for longer exposure times. Rearranging equation A.5 shows that C_j can be regarded as a variance for a measurement scaled by the value of that measurement,

$$C_j = \frac{\sigma_j^2(\bar{h})_I}{I_j(\bar{h})} \qquad \text{(A.6)}$$

It should be constant for a given exposure time, and can be estimated from the data itself by,

$$C_j = \frac{\sigma_j^2(\bar{h})_I}{I_j(\bar{h})} = \frac{1}{M-1}\sum_{\bar{h}} \frac{[I_j(\bar{h}) - \bar{I}(\bar{h})]^2}{\bar{I}(\bar{h})} \qquad \text{(A.7)}$$

where the sum is taken over all reflections measured in picture number j. Equation A.7 is actually a recursive relationship since the average value for a measurement, $\bar{I}(\mathbf{h})$, should be calculated using equation A.1 taking into account the relative uncertainties of measurements from different pictures. So $\bar{I}(\mathbf{h})$ depends on the estimates of the Cj.

To find self-consistent estimates for the C_j, we run iterative calculations using equation A.7. For the initial iteration, we take all of the C_j=1 and calculate the $\overline{I}(\mathbf{h})$ with an equal weighting of all pictures. In the next pass, the $\overline{I}(\mathbf{h})$ are recalculated using the estimates for the C_j found during the initial iteration. The procedure continues (usually for about 10 cycles) until the C_j converge to a self-consistent set. Once the C_j are known, then we have estimates for the uncertainties of individual measurements, and final average values with associated errors can be calculated for all of the reflections using equations A.1 and A.2.